

2

AD-A271 988



NASA  
Technical  
Paper  
3357

ATCOM  
Technical  
Report  
92-A-013

March 1993

# Suppression of Dynamic Stall with a Leading-Edge Slat on a VR-7 Airfoil

K. W. McAlister  
and C. Tung

NOV 03 1993  
S E D



US ARMY  
AVIATION and  
TROOP COMMAND



National Aeronautics and  
Space Administration

Approved for public release  
Distribution unlimited

93-26696



93 11 8 045

**NASA  
Technical  
Paper  
3357**

**ATCOM  
Technical  
Report  
92-A-013**

1993

# Suppression of Dynamic Stall with a Leading-Edge Slat on a VR-7 Airfoil

**K. W. McAlister  
and C. Tung**  
*Aeroflightdynamics Directorate  
U.S. Army Aviation and Troop Command  
Ames Research Center, Moffett Field, California*

Accession For	
NTIS	CRA&I <input checked="" type="checkbox"/>
DTIC	TAB <input type="checkbox"/>
Unannounced <input type="checkbox"/>	
Justification	
By	
Distribution/	
Availability Codes	
Dist	Availability of Special
<b>A-1</b>	

**NASA**  
National Aeronautics and  
Space Administration

**Ames Research Center**  
Moffett Field, California 94035-1000

DTIC QUALITY INSPECTED 5

# CONTENTS

<b>SUMMARY</b>	1
<b>NOMENCLATURE</b>	1
<b>INTRODUCTION</b>	1
<b>TEST DESCRIPTION</b>	2
The Facility and the Model . . . . .	2
Load Measurements . . . . .	3
Flow Visualization . . . . .	3
<b>RESULTS AND DISCUSSION</b>	4
Basic VR-7 Airfoil . . . . .	5
VR-7 Airfoil with Slat . . . . .	6
Contrast in Performance . . . . .	7
<b>CONCLUDING REMARKS</b>	9
<b>REFERENCES</b>	9
<b>TABLES</b>	10
<b>FIGURES</b>	11

## SUMMARY

The VR-7 airfoil was experimentally studied with and without a leading-edge slat at fixed angles of attack from  $0^\circ$  to  $30^\circ$  at  $Re = 200,000$  and for unsteady pitching motions described by  $\alpha = \alpha_m + 10^\circ \sin(\omega t)$ . The models were two dimensional, and the test was performed in a water tunnel at Ames Research Center. The unsteady conditions ranged over  $Re = 100,000 \rightarrow 250,000$ ,  $k = 0.001 \rightarrow 0.2$ , and  $\alpha_m = 10^\circ \rightarrow 20^\circ$ . Unsteady lift, drag, and pitching-moment measurements were obtained along with fluorescent-dye flow visualizations. The addition of the slat was found to delay the static-drag and static-moment stall by about  $5^\circ$  and to eliminate completely the development of a dynamic-stall vortex during unsteady motions that reached angles as high as  $25^\circ$ . In all of the unsteady cases studied, the slat caused a significant reduction in the force and moment hysteresis amplitudes. The reduced frequency was found to have the greatest effect on the results, whereas the Reynolds number had little effect on the behavior of either the basic or the slatted airfoil. The slat caused a slight drag penalty at low angles of attack, but generally increased the lift/drag ratio when averaged over the full cycle of oscillation.

## NOMENCLATURE

$A_p$	planform area of airfoil (span $\times$ chord)
$c$	chord of basic VR-7 airfoil
$C_d$	drag coefficient, drag/ $A_p q_\infty$
$C_l$	lift coefficient, lift/ $A_p q_\infty$
$C_m$	moment coefficient, moment/ $c A_p q_\infty$
$k$	reduced frequency, $\omega c / 2V_\infty$
$q_\infty$	dynamic pressure, $\frac{1}{2} \rho V_\infty^2$
$Re$	Reynolds number, $c V_\infty / \nu$
$t$	time
$V_\infty$	free-stream velocity
$\alpha$	airfoil angle of attack
$\alpha_m$	mean angle of oscillation
$\nu$	fluid kinematic viscosity
$\rho$	fluid density
$\omega$	frequency of oscillation in pitch, rad/sec

## INTRODUCTION

The blades of a helicopter rotor in forward flight must undergo a cyclic change in angle of attack in

order to produce a balanced lift between the advancing and retreating sides of the rotor disk. An observer positioned on the rotor hub and looking toward the tip of the rotor blade would see the blade sinusoidally oscillating in pitch from a low angle on the advancing side to a high angle on the retreating side. The demand for either a higher flight speed or a higher level of thrust requires that the angle of attack of the blade on the retreating side must be increased to an even higher value to provide the needed lift. Because the motion is unsteady, an increase beyond the static-stall angle can normally be tolerated before incurring any adverse effects, thereby enabling an unusually high value of lift to be exploited. However, at a sufficiently high angle of attack, a portion of the blade on the retreating side will experience stall. The stall that occurs in this unsteady environment is called dynamic stall, and it is characterized by a sudden increase in the peak loads as well as by an increase in the hysteresis amplitudes.

Serious attention to the peculiar events characteristic of unsteady pitching motions beyond the static-stall angle began with a concern over aerodynamic damping and stall flutter on rotor blades (ref. 1). It was found that the associated transient and often severe loadings on the blade could be charged to the shedding of intense vorticity (later to be called a dynamic-stall vortex) from the forward part of the upper surface, and that the process could be investigated in relatively simple two-dimensional oscillating airfoil experiments (ref. 2). These tests have shown that as the vortex moves over the surface, the center of pressure moves aft and induces a nose-down pitching moment. As the vortex moves off the trailing edge, the high lift, drag, and pitching moment loads reach a peak, and then suddenly collapse. These impulsive loads produce vibrations that not only impact the design and fatigue life of mechanical linkages (ref. 3), but also contribute to structural problems, and excite resonances that degrade human performance (ref. 4). Considering the damaging effects that dynamic stall has on both the machine and its crew, the operational envelope of the helicopter is limited.

In an effort to quantify the importance of profile shape on the initiation and extent of unsteady separation on oscillating airfoils, it was found that although the shape of the airfoil has some influence on the loads during light stall, those differences are obscured by the large (and somewhat similar) hysteresis loops that occur during deep stall (refs. 5 and 6). This finding suggested that something more radical than a change

in profile would be required in order to avoid or even modify the stall vortex. Numerous informal experiments were performed at the Army Aeroflightdynamics Directorate, and several candidate approaches proved to be successful. One of these approaches involved the addition of a slat to the leading edge of an airfoil that already had a good rotor performance record (ref. 7). The new design was based on a VR-7 for the main element and a NACA 15320 for the slat. An optimization code (ref. 8) was used to determine the best relative orientation of the two elements for achieving the maximum stall-free lift in a steady two-dimensional flow.

It was already known from the literature (refs. 9 and 10) that the lift of an airfoil at high angles of attack can be improved by segmenting an airfoil into multiple elements. The forward segment, or slat, was originally referred to simply as the additional airfoil forming the leading edge of the multi-element airfoil. The explanation (ref. 9) given for the overall improvement in performance obtained with this configuration was that the slat and the main element reacted to the others presence in a mutually beneficial way. The slat relieved the adverse pressure gradient on the nose of the main element (thereby delaying separation), and the main element provided a lower pressure region around the trailing edge of the slat (thereby allowing the slat to reach higher angles of attack before stalling). A more recent explanation (ref. 11) credits the slat with producing most of the vorticity and then shedding it at a large enough distance above the main element so that not only are higher convective velocities available to usher the vorticity downstream, but the retarding influence of the image system that exists along the upper surface of the airfoil is greatly reduced.

In an earlier oscillating airfoil experiment involving the slat (ref. 7), only the main element was instrumented. Although the data was sufficient to indicate the success of the slat in preventing the formation of the dynamic-stall vortex, the total performance could only be qualitatively inferred. The purpose of the present experiment was to determine the dynamic loads (lift, drag, and pitching moment) on the entire configuration and to explore a wider range of conditions. Another objective was to ascertain the applicability of relatively low-Reynolds-number tests in a water tunnel for evaluating the merits of various high-lift concepts that are intended for use at high Reynolds numbers. Results will be presented for the VR-7 airfoil with and without a leading-edge slat for  $Re = 100,000 \rightarrow 250,000$  and

$\alpha = \alpha_m + 10^\circ \sin(\omega t)$ , with  $\alpha_m = 10^\circ \rightarrow 20^\circ$  and  $k = 0.001 \rightarrow 0.2$ .

## TEST DESCRIPTION

### The Facility and the Model

This experimental study was conducted in the closed-circuit water tunnel at the Aeroflightdynamics Laboratory at Ames Research Center (fig. 1). Advantages at this facility are that unsteady loads on the entire airfoil can be measured, and visualizations of the flow can be easily obtained.

The test section is 8.3 in. wide, 12 in. high, and extends 34 in. horizontally. There are removable windows on all four sides. The free-stream velocity of the water ( $V_\infty$ ) is determined from the difference in static pressure between the settling chamber and the test section. A honeycomb and several screens are positioned in the settling chamber to straighten the flow and reduce the turbulence intensity to about 0.05% when a model is not present in the test section. The turbulence intensity can increase by a factor of five when a stalled airfoil is present in the test section. The tunnel was operated at an ambient temperature of about 70°F.

The model selected for this study was a Boeing-Vertol VR-7 airfoil (fig. 2). The basic airfoil (that is, the model without the slat) was two dimensional, having a chord length of 4 in. and a span of 8.3 in. To minimize the moment of inertia of the airfoil, the main body of the airfoil was made from a lightweight urethane material and the bulk of the stainless steel spar was concentrated around the quarter-chord pitch axis. The mean camber line over the aft 5% of the VR-7 airfoil is inclined  $+3^\circ$  relative to the chord line (officially designated as  $-3^\circ$  tab). To insure rigidity, the thickness of this section was maintained at  $0.005c$  by incorporating a stainless steel plate (0.020 in. thick) along the trailing edge of the airfoil.

In the case of the VR-7 airfoil with a leading-edge slat (fig. 2), a separate VR-7 model was used for the main element and a NACA 15320 profile was used for the secondary element. The chord length of the slat was 10% of that of the main element. The slat was positioned  $0.074c$  forward,  $0.056c$  downward, and at a negative angle of attack of  $51.5^\circ$  with respect to the chord line of the main element. The slat and the attachment ribs were machined from stainless steel as a single unit and joined to the spar with pins. The slat

and spar assembly are shown in figure 3 alongside the mold used for constructing the VR-7 airfoil.

## Load Measurements

When installed in the water tunnel, the spar of the airfoil extended through the test-section windows and was supported by lift and drag transducers on both sides (fig. 4). One end of the spar was connected to an instrumented drive shaft through a torsionally stiff coupling so that airfoil incidence and pitching moment could be measured. Frictional moments imparted by the support bearings and seals were also measured and later treated as dynamic-load tares. Inertial loads were assumed to be small because the oscillation frequency was always less than 1.2 Hz and the urethane/water density ratio was around 1 (compared to a urethane/air density ratio of around 980).

The electrical instrumentation consisted of transducers for the measurement of airfoil incidence, lift (both sides), drag (both sides), total pitching moment, and the bearing and seal moments (both sides). After amplification, these signals were either summed appropriately (i.e., both frictional moments subtracted from the total pitching moment) and displayed on local monitors, or they were transmitted to a remote data acquisition system where they were digitized and ensemble averaged. Digitizing and averaging operations were based on two additional signals: a 360/rev pulse train that was synchronous with  $\omega t$ , and a 1/rev pulse that was synchronous with the beginning of each cycle of oscillation.

In cases involving an airfoil undergoing oscillations in pitch, the ensemble average of a given unsteady load was monitored in real time so that the data acquisition sequence could be terminated at any time. Although the average was routinely based on 100 cycles of data, this online capability of monitoring the progress of the averaging process was especially useful when the period of oscillation was long. Oscillation periods in this experiment ranged from about 0.8 sec to 166 sec. When the oscillation period was considered too long (in view of potential errors due to "zero" drifts), the acquisition was terminated once a given load was observed to have obtained a desired smoothness. This was a subjective decision and it depended greatly on the nonperiodic content of the signal.

In cases involving the VR-7 at fixed angles of attack, the "steady" data were digitized at a rate of 360 samples/sec and averaged over a period of 30 sec.

A limited amount of data was obtained for the basic VR-7 to ascertain the time-dependent nature of the flow (especially when the airfoil is stalled). For these cases the data were digitized at a rate of 1000 samples/sec over a period of 10 sec.

In addition to the averaged data being stored for future processing, the data was automatically reduced to engineering coefficients and graphically presented in a familiar format that showed the lift, drag, and moment loads versus angle of attack. This practice of immediately displaying the results permitted a timely evaluation of the data so that any irregularity in the measurement system could be quickly exposed and corrected. It is estimated that the angle of attack of the airfoil could be measured with an accuracy of  $0.2^\circ$ . Lift and drag measurements are considered accurate to 0.002 lb and the pitching moments to 0.02 in-lb.

## Flow Visualization

The technique for visualizing the flow was based on the release of a fluorescing dye from an orifice (0.030-in. diameter) located midspan on the leading edge of the VR-7 airfoil. The same orifice location was used for both the basic and slatted airfoils. No provision was made for releasing dye from the slat in this experiment. The dye solution was prepared from Rhodamine 6G and deionized water at a ratio of about 1 mg powder to 800 ml water. This aqueous solution was carried to the model through a flexible tube from a reservoir located above the water tunnel and at a sufficient height to maintain flow at all angles of attack. The dye flowed out from the surface of the airfoil and mixed with the fluid coming from the stagnation region. The mixture was then transported downstream from the leading edge by the fluid in the boundary layer and wake, thereby enabling the thickness and eventual separation of the boundary layer to be observed.

The dye appears orange under ordinary room lighting, and has a fluorescence emission that is yellow when the dye is stimulated by light at a shorter wavelength. Since a dark background offers the best contrast with yellow, the rear test-section wall was painted black and a black pigment was included in the urethane mixture when the VR-7 models were cast. The dye was stimulated by two sources of light: a Xenon strobe which emitted a large quantity of radiation in the ultraviolet range, and an Argon-ion laser which emitted a majority of its radiation in the green and blue range.

The strobe cavity has the shape of a long tube so that the light from the Xenon gas needed only to be baffled to form a sheet of light with a thickness of about 1 in. The light from the laser was carried along an optical fiber and then directed onto a mirror that was oscillating at about 120 cps. The slightly diverging beam that was reflected from the mirror formed a fan of light with nearly the same thickness as the strobe. In both cases, the light passed through the upper test-section window and straight down onto the airfoil surface. The strobe was used for the single-frame recordings which were made on Kodak TMY 6053 black and white film (ASA 400), and the laser was used for the video recordings (30 frames/sec) on Betacam-formatted film.

The flow visualization portion of the experiment was performed with the lift and drag balance removed on the viewing side of the tunnel, thereby allowing the cameras to sight down the axis of rotation without being obstructed. The pitching moment gage remained active during the flow visualizations, and the time history of this signal was simultaneously recorded with a second video camera (fig. 5). A single time code was recorded on both video films so that image overlays could be synchronized during a post-test editing session. Values of either  $\omega t$  (unsteady case) or  $\alpha$  (steady case) were digitally displayed by light-emitting diodes that were positioned in the field of view of the camera looking into the test section.

## RESULTS AND DISCUSSION

Both steady and unsteady data were obtained for the basic and slatted airfoils. A majority of this data was taken at  $Re = 200K$  at ambient temperatures between  $67^\circ F$  and  $70^\circ F$ . For a 4-in.-chord airfoil this Reynolds number corresponds approximately to a free-stream velocity of 6.5 ft/sec and a dynamic pressure of  $0.28 \text{ lb/in}^2$ .

Steady data were obtained over a range of angles of attack from  $0^\circ$  to  $30^\circ$ . Unsteady data were primarily for airfoil oscillations described by  $\alpha = 15^\circ + 10^\circ \sin(\omega t)$ , with the pitching motion being about the quarter-chord axis, at reduced frequency  $k = 0.1$ . This value of reduced frequency corresponded to an oscillation frequency of about 0.66 cps. In addition to these primary conditions, a limited amount of data was also taken for Reynolds numbers ranging from 100K to 250K, mean angles ranging from  $10^\circ$  to  $20^\circ$ , and reduced frequencies ranging from 0.001 to 0.2

(tables 1–3). When measurements are taken on a lifting airfoil in a flow that is confined by tunnel walls, certain quantities (such as the lift coefficient) are altered from their free-air values because of blockage and a distortion of the streamlines. In a closed test section, blockage has the effect of producing higher velocities in the region where the airfoil is located. A change in streamline curvature has the effect of increasing the "apparent" camber of the airfoil and inducing a higher angle of attack (ref. 12).

Since the frontal area of the present airfoil at  $\alpha = 25^\circ$  is 13.8% of the cross-sectional area of the test section and since the chord of the airfoil is 33% of the height of the test section, some amount of blockage of the flow and distortion of the streamlines around the airfoil can be expected. However, since the available methods for determining wall corrections are not exact, the data are presented as measured, without the introduction of any questionable (and irreversible) alterations. This point should be kept in mind when these data are compared with free-air calculations or other experimental data, but it is of little concern as long as the comparisons are limited to cases within this experiment.

The dynamic pressure,  $q_\infty$ , is involved in the calculation of the nondimensional coefficients  $C_l$ ,  $C_d$ , and  $C_m$ . In unsteady flows that involve pitching airfoils, the average value for  $q_\infty$  may be used as long as the blockage is small. When the blockage is not small and the tunnel drive does not have a feedback circuit for maintaining a constant speed, then the dynamic pressure will vary in concert with changes in the total pressure (which, in turn, are caused by a cyclic variation of the drag force on the oscillating airfoil). This unsteady behavior of  $q_\infty$  will be especially significant when the airfoil oscillates in and out of deep stall. For this reason, it is important that the instantaneous value of  $q_\infty$  be used to calculate the load coefficients. If the average value of  $q_\infty$  is mistakenly used to calculate these coefficients, the amount of hysteresis present in the data will be altered. This feature is particularly evident in quasi-steady data that includes an  $\alpha$  sweep through the low-angle-of-attack range in which the flow is normally attached (fig. 6).

A pitching airfoil that goes beyond the static-stall angle produces an unsteady flow in which separation and stall can be quite different from that experienced in steady flow. In both cases separation occurs when the flow (either laminar or turbulent) encounters an adverse

pressure gradient and can no longer follow the surface of the airfoil. However, the relationship between reversed flow and separation depends on whether the flow is steady or unsteady. In steady flow, the point of reversed flow is coincident with the point of separation. In unsteady flow, the entire upper surface of an airfoil may temporarily experience reversed flow without any evidence of separation. In steady flow, the spread of separation affects the force and moment loads and characterizes the stall. When stall occurs, there is massive separation and all the loads are affected simultaneously. In unsteady flow, the effects of separation are normally augmented substantially by the formation and shedding of a vortex over the upper surface. During the finite time it takes for the vortex to travel over the airfoil, the drag and pitching moment rapidly grow in magnitude (thereby initiating drag and moment stall) while the lift continues to benefit from the low pressure that accompanies the vortex. It is not until the vortex leaves the trailing edge that the lift collapses (indicating lift stall). These distinctions should be kept in mind when reading the following discussions.

### Basic VR-7 Airfoil

**Steady results**— The steady results for the basic VR-7 airfoil show that the loads are linearly dependent on the angle of attack for  $\alpha \leq 8^\circ$  (fig. 7). For angles above  $8^\circ$  the lift-curve slope gradually decreases, indicating that the flow is undergoing an increasing amount of separation from the trailing edge of the airfoil (also verified in flow visualizations in fig. 8). As the point of separation moves toward the leading edge, the center of pressure moves aft to produce an increasingly negative (nose down) pitching moment. The abrupt changes in drag and pitching moment that occur between  $\alpha = 18^\circ$  and  $\alpha = 19^\circ$  signal that the airfoil has fully stalled. The data obtained from wind tunnel tests (refs. 6 and 13) at higher Reynolds numbers exhibit the same linear behavior at low values of  $\alpha$  and an increasingly negative pitching moment up to the point of stall (fig. 9). The stall angles are different in each case and the lift collapses more rapidly with angle of attack as the Reynolds number and Mach number are increased.

Although these results are referred to as “steady,” they are actually the average of values taken over a period of time. The time histories of these loads (fig. 10) indicate an abundance of unsteadiness with amplitudes

and frequencies that depend on the angle of attack (or the scale of the separated flow). The high-frequency segment that is superimposed on the drag at 0.6-sec intervals (fig. 10(b)) is due to noise in the drive system that is telegraphed along the tunnel walls to the balance, and should be disregarded. Aside from this, a cursory examination of the curves reveals that as the angle of attack increases, the amplitude of the unsteadiness increases, but the frequency decreases.

A dominant frequency (or tone) appears in the pitching moment at  $\alpha = 0^\circ$  (fig. 10(c)) and is probably due to vortex shedding from the trailing edge (alternating between the upper and the lower surface, one clockwise and the next counterclockwise). It can be reasoned that the moment is the load most sensitive to this shedding phenomenon since the small alternating forces that are produced by these vortices are amplified by virtue of their large distance from the pitch axis (and hence large moment arm). The shedding frequency is 127 cps, which corresponds to a Strouhal number of 0.74 (based on the projected thickness of the airfoil). Since the thickness of the wake at the trailing edge of the airfoil is much less than the projected thickness of the airfoil, an effective Strouhal number based on the wake thickness would no doubt be much more comparable to the classical value of 0.21 (ref. 14) reported for flows past circular cylinders (when shedding occurs, the wake thickness is nearly equal to the diameter of the circular cylinder).

**Unsteady results**— The basic VR-7 airfoil was tested over a range of Reynolds numbers, reduced frequencies, and mean angles of oscillation. In all cases, the unsteady motion was sinusoidal in pitch about an axis passing through the quarter-chord of the airfoil. The load coefficients  $C_l$ ,  $C_d$ , and  $C_m$  are calculated using the chord of the basic airfoil as the reference length and the instantaneous value of the dynamic pressure. When the results are displayed with  $\alpha$  as the independent variable, a solid curve is used when  $\alpha$  is increasing and a dashed curve is used when  $\alpha$  is decreasing. When the results are displayed with  $\omega t$  as the independent variable, the curve begins and ends at the minimum angle of attack (which is  $\omega t = -90^\circ$  or, equally,  $\omega t = 270^\circ$ ).

The effects of Reynolds number were examined over a range from  $Re = 100K$  to  $Re = 250K$  (fig. 11). The reduced frequency of oscillation and the pitching motion were maintained at  $k = 0.10$  and  $\alpha = 15^\circ + 10^\circ \sin(\omega t)$ . In each case the airfoil stalls, as evidenced by the sudden and large changes in the drag

and pitching moment curves. The lift curve shows a broad hysteresis loop, indicating that the stall is followed by an extensive amount of separation that lingers throughout the "pitch-down" portion of the cycle. Although the results may differ somewhat in detail, there appears to be no significant difference in the curves over this range of Reynolds numbers (fig. 12).

The effects of reduced frequency were examined over a range of  $k$  from 0.001 to 0.20 (fig. 13). The Reynolds number and the pitching motion were maintained at  $Re = 200K$  and  $\alpha = 15^\circ + 10^\circ \sin(\omega t)$ . Increasing the reduced frequency caused an increase in the stall angle of attack, a decrease in the recovery angle of attack, and a broadening of the hysteresis amplitude. These extensions of the separated-flow boundaries and the broadening of the hysteresis loops are most evident in the lift curves (fig. 14). A feature that is particularly noticeable at low reduced frequencies is the gradual decrease in the lift-curve slope with angle of attack during the "pitch-up" portion of the cycle. This decrease in slope is due to the spread of separated flow over the upper surface of the airfoil from the trailing edge. Increasing the reduced frequency delays this decrease in the lift-curve slope to higher angles of attack. Increasing the reduced frequency also increases the damping in pitch (in a positive sense), and causes an increase in all of the peak loads (lift, drag, and pitching moment). The damping in pitch is positive when the  $C_m$  vs.  $\alpha$  curve is traversed in a counter-clockwise sense ( $-\oint C_m d\alpha > 0$ ), and indicates that the airfoil is imparting energy to the surrounding flow.

Another noteworthy feature of the unsteady flow at all Reynolds numbers is the peculiar distortion in the lift curve that occurs just before the peak. Visualizations of the flow reveal that this distortion (consisting of several inflections) corresponds to the initial growth and movement of the dynamic-stall vortex over the upper surface of the airfoil (fig. 15). A review of the curves in figure 13 at various reduced frequencies indicates that the drag is only mildly sensitive to this event. However, the moment shows a sudden increase in value followed by a sudden decrease. These rapid reversals in the moment are due to the changing position of the stall vortex on the airfoil. The vortex is initially forward of the pitch axis, hence it produces a positive increment in the moment. The vortex then moves aft over the upper surface, thereby producing an increasingly negative increment in the moment.

The point in the cycle of oscillation when the vortex passes over the pitch axis of the airfoil (the quarter-chord in the present case) is signaled, approximately, by two distinct characteristics in the loads: it is preceded by a positive spike in the moment curve and it is coincident with a sudden increase in the lift-curve slope. These are important events because they not only offer clear evidence that a vortex is present on the airfoil, but they herald an approaching stall. The associated distortion in each load curve is identified by the middle arrow in figure 15 and is explored more fully in figure 16 for a range of reduced frequencies. This impending moment-stall condition, marked by rapid flow separation and the initial movement of the vortex over the upper surface, is very dependent on the reduced frequency (fig. 17). The higher the frequency of oscillation (corresponding to higher values of  $k$ ), the longer this condition is delayed (corresponding to higher values of  $\omega t$ ). The delay appears to be nearly linear with  $\omega t$ , which is the same result that was obtained for a NACA 0012 airfoil in an earlier wind tunnel experiment (ref. 15).

The effects of the mean angle of oscillation were examined over a range from  $10^\circ$  to  $20^\circ$  (fig. 18). The Reynolds number was fixed at 200K, the reduced frequency at 0.10, and the amplitude of oscillation at  $10^\circ$ . Increasing the mean angle can be seen to broaden the hysteresis amplitudes in each of the loads and increase the level of positive-pitch damping (fig. 19). For all of the mean angles considered, a common succession of events occurs during the pitch-up portion of the cycle. Over a portion of this interval the flow is attached and the load curves are coincident (independent of mean angle). This attached segment is followed by the same distortions in the lift and moment curves prior to stall that were discussed earlier (recall the sudden increase in lift-curve slope and the positive spike in the moment), even though the instantaneous value of  $d\alpha/dt$  for this event is substantially different in each case.

## VR-7 Airfoil with Slat

**Steady results**— The steady results for the VR-7 airfoil with slat show that the loads are nowhere linearly dependent on the angle of attack (fig. 20). There are two inflections in the lift curve, one around  $\alpha = 8^\circ$  and the other around  $\alpha = 21^\circ$ . The reason for the first inflection can be better understood with the help of the flow visualizations shown in figure 21. There appears to be a reversal in the growth of the boundary layer

over the aft portion of the airfoil between  $\alpha = 5^\circ$  and  $\alpha = 15^\circ$ , which implies a reversal in the extent of trailing-edge separation present on the airfoil. This recovery may be due to the energizing effect of the flow coming from the region between the slat and the main element. Although the flow over the slat was not visualized, the second inflection may reflect a degradation in lift on the main element as a result of trailing-edge separation (quite apparent at  $\alpha = 20^\circ$ ) followed by a boost in lift as the slat assumes a more favorable orientation to the oncoming flow. The lift reaches a maximum at around  $\alpha = 23^\circ$ , and although the drag and moment have suddenly increased at this angle of attack, the lift is only modestly degraded as the angle of attack is increased further.

**Unsteady results**— The VR-7 airfoil with slat was tested over the same range of conditions as that used to test the basic airfoil. The load coefficients  $C_l$ ,  $C_d$ , and  $C_m$  are calculated using the chord of the basic airfoil as the reference length (not the length of the main element plus the slat) and the instantaneous value of the dynamic pressure.

The effects of Reynolds number were examined for  $Re = 100K$  to  $Re = 250K$  (fig. 22). The reduced frequency of oscillation and the pitching motion were maintained at  $k = 0.10$  and  $\alpha = 15^\circ + 10^\circ \sin(\omega t)$ . In each case the airfoil is observed to execute a complete cycle of oscillation without any evidence of dynamic stall. The hysteresis present in all of the load curves is due to both the unsteady motion of the airfoil ( $d\alpha/dt$ ) and the extent of the separated flow during the cycle of oscillation. Although the results appear to be qualitatively similar throughout the cycle over the entire Reynolds number range (fig. 23), especially when  $\alpha < 15^\circ$ , there is a noticeable improvement in the lift and pitching moment (with only positive contributions to the pitch-damping) at high angles of attack when  $Re = 250K$ .

The effects of reduced frequency were examined over a range of  $k$  from 0.001 to 0.20 (fig. 24). The Reynolds number and the pitching motion were maintained at  $Re = 200K$  and  $\alpha = 15^\circ + 10^\circ \sin(\omega t)$ . At the lowest reduced frequency ( $k = 0.001$ ) the load curves are essentially free of any hysteresis and are nearly identical to the static results shown in figure 20. There is some raggedness in the data for  $\alpha > 23^\circ$  (caused by unsteadiness in the separated portion of the flow) that is not smoothed out by averaging over only five cycles of oscillation. At  $k = 0.005$  the lift curve

begins to show some hysteresis. There is also an increase in the lift as the airfoil is pitching up (beginning at  $\alpha > 13^\circ$ ) and the inflection at  $\alpha = 21.5^\circ$  has nearly vanished. The flow is evidently sufficiently sensitive to even this modest value of  $d\alpha/dt$ , with the result being a measurable delay in the appearance of separation on the airfoil. Increasing the reduced frequency causes the hysteresis amplitudes to broaden and the lift-curve slope to become more linear. Although the maximum value of lift increases with increasing  $k$ , the maximum value of drag is slightly reduced (fig. 25). As  $k$  is increased, the pitching moment experiences a decrease in the negative peak and an increase in the positive peak, and the damping becomes more positive.

The effects of the mean angle of oscillation were examined over a range from  $10^\circ$  to  $20^\circ$  (fig. 26). The Reynolds number was fixed at 200K, the reduced frequency at 0.10, and the amplitude of oscillation at  $10^\circ$ . Increasing the mean angle of oscillation results in progressively higher loads on the airfoil (fig. 27). There is no evidence of a stall vortex; however, the broadening of the hysteresis loops and the increase in the magnitude of the pitching moment at high angles of attack indicate that a substantial amount of trailing-edge separation may be present over the airfoil.

## Contrast in Performance

For convenience, the results are graphically summarized in figures 28–30 so that any dependence on  $k$ ,  $Re$ , and  $\alpha_m$  can be readily distinguished for the basic and the slatted cases. In every case, the hysteresis amplitudes, as well as the peak values of drag and pitching moment, have been significantly reduced by the addition of the slat. The Reynolds number has little effect on either the basic or the slatted case. The reduced frequency has the greatest effect, causing large increases in the hysteresis amplitudes and the peak load values. Increasing the mean angle does not eliminate the presence of dynamic stall in the basic case (it still occurs at about  $\alpha = 20^\circ$ ), and it does not provoke the development of a classical stall vortex in the slatted case, although the amount of trailing-edge separation does increase.

The contrast between the basic and slatted airfoils is typified by the results presented in figure 31, which are for  $Re = 200K$ ,  $k = 0.1$ , and  $\alpha = 15^\circ + 10^\circ \sin(\omega t)$ . The loads are displayed as a function of  $\omega t$  and the corresponding flow visualizations are shown at 45-deg intervals, beginning at the minimum angle of

attack ( $\alpha = 5^\circ$  when  $\omega t = -90^\circ$ ). The dynamic-stall vortex is clearly evident at  $\omega t = 45^\circ$  in the basic case, and the flow still has not recovered from stall after reaching  $\omega t = 180^\circ$ . In the slatted case the boundary layer appears much thicker, there is no evidence of separated flow until reaching  $\omega t = 90^\circ$ , and reattachment is already in progress at  $\omega t = 180^\circ$ .

The forward portion of the main element (just behind the slat) always appears attached (fig. 31(b)), indicating that in all likelihood the slat never experiences stall. During the time that the flow is separated over part of the main element, the viscous layer becomes reorganized briefly into several discrete vortices ( $\omega t = 90^\circ$ ), which soon coalesce into a single dominant vortex ( $\omega t = 135^\circ$ ) as they move down the airfoil. This multiple-vortex organization of the separated flow has been observed in the past (ref. 16) and seems to be the result of an instability that is characteristic of the free-shear layer that is formed between the outer flow and the reversing flow next to the surface of the airfoil.

The onset of dynamic stall on the basic VR-7 airfoil is rather sudden, beginning with a condition of reversed flow over a majority of the upper surface (starting at  $\omega t = 25^\circ$  in fig. 32(a)). The viscous layer in this unsteady environment is much thinner than it would be had the airfoil been at a fixed angle of attack with the same amount of reversed flow (ref. 16). At roughly 5% chord, the flow moving toward the leading edge meets with the flow moving away from the leading edge and causes an enlargement of the viscous layer ( $\omega t = 26^\circ$ ). Within this viscous flow protuberance, the vorticity (which was generated along the surface, starting at the stagnation point) accumulates until reaching a stage when it "breaks away" and moves down the airfoil ( $\omega t = 40^\circ$ ).

While the stall vortex is developing near the leading edge of the basic airfoil (fig. 32(a)), the aft portion separates and appears dominated by a "shear-layer vortex" (ref. 16). This sequence of events is in clear contrast to what occurs on the VR-7 airfoil with slat (fig. 32(b)). In the case of the slatted airfoil, a dynamic-stall vortex does not appear; however, a similar separation and shear-layer vortex does occur over the aft portion of the main element. Although the region of trailing-edge separation appears to extend farther into the outer flow in the basic case (compare  $\omega t = 40^\circ$  in fig. 32(a) with  $\omega t = 90^\circ$  in fig. 32(b)), the forward progression of this region up the airfoil is slightly higher in

the slatted case (fig. 33). The success of the leading-edge slat in delaying the static stall and suppressing the dynamic-stall vortex is shown in figure 34. In the unsteady case, the hysteresis amplitudes and peak drag and moment loads are significantly reduced by the slat. This means that the impulsive loads that normally attend the basic airfoil have been virtually eliminated (note especially the comparatively modest variation along the pitching moment curve). In the static case, the drag and moment curves indicate that the slat has produced a much more gentle stall. The slat has also delayed the onset of static stall by about  $5^\circ$  (at  $\alpha = 22^\circ$ ), however the peak in the lift curve does not occur for about another  $3^\circ$  (at  $\alpha = 25^\circ$ ) where it is accompanied by another inflection change in both the drag and pitching moment curves.

Although the streamlined appearance of the airfoil has been compromised by the addition of the slat, there seems to be only a slight drag penalty at low angles of attack (fig. 34). This result was also reported in reference 17. With regard to lift/drag, the slat offers an advantage over the basic airfoil for fixed angles of attack when  $\alpha > 15^\circ$  (fig. 35). For  $\alpha < 15^\circ$  the lift/drag is lower for the slatted airfoil because of a loss of lift on the main element. In the unsteady case ( $\alpha_m = 15^\circ$  and  $k = 0.1$ ), the slatted airfoil has about a 10% advantage over the basic airfoil if the lift/drag is averaged over the complete cycle of oscillation. Provided that the airfoil oscillation ranges over the higher angles of attack, the lift/drag will be higher with the slat for all  $k$  (fig. 36).

Whereas the results of this study may not contain certain features found in compressible flows at higher Reynolds numbers (water is virtually incompressible and the slat Reynolds number is only about 20K), the present data are in good agreement with the findings of an earlier study dealing with the effects of a slat on dynamic stall (ref. 7). In this earlier study, conducted in a wind tunnel where the Mach number was 0.19 and the Reynolds number was  $2.5 \times 10^6$ , the same observations were made regarding the reduction of hysteresis amplitudes, peak lift and moment loads, and the stall vortex. Although there are differences in some details between the water tunnel and the wind tunnel results, the effect of the slat is qualitatively the same in both cases (fig. 37).

## CONCLUDING REMARKS

The basic findings of this study were as follows:

1. The addition of a leading-edge slat on a VR-7 airfoil delays the static-drag and static-moment stall by about  $5^\circ$  and eliminates completely the development of a dynamic-stall vortex during unsteady motions that reach angles as high as  $25^\circ$ .

2. The forward portion of the main element (just behind the slat) always appeared attached, indicating that the slat may not have experienced stall for any of the steady or unsteady conditions studied.

3. The slat caused a more gradual advance of trailing-edge separation to occur over the main element. The contribution of the slat to the overall static lift was sufficient to enable the angle of attack to be increased an additional  $8^\circ$  before reaching a peak value.

4. The onset of dynamic stall on the basic VR-7 airfoil is sudden, beginning with a condition of reversed flow over a majority of the upper surface. At roughly 5% chord, the flow moving toward the leading edge meets with the flow moving away from the leading edge and causes an enlargement of the viscous layer. Within this viscous flow protuberance, vorticity accumulates until it "breaks away" and moves down the airfoil.

5. In every unsteady case studied, the hysteresis amplitudes, as well as the peak values of drag and pitching moment, were significantly reduced by the addition of the slat. The Reynolds number was found to have little effect on the results for either the basic or the slatted airfoil. The reduced frequency had the greatest effect, causing a large increase in the hysteresis amplitudes and the peak load values. Increasing the mean angle did not provoke the development of a classical stall vortex in the slatted case (although the amount of trailing-edge separation did increase).

6. Although the slat altered the streamlined appearance of the airfoil, there was only a slight drag penalty at low angles of attack. At fixed angles of attack, the slat causes higher values of lift/drag when  $\alpha > 15^\circ$ . When the motion was unsteady and  $\alpha_m > 13^\circ$ , the averaged lift/drag for the slatted airfoil became increasingly higher than that for the basic airfoil as  $k$  increased.

7. The present water tunnel results are qualitatively the same as those obtained in an earlier wind tunnel test at a much higher Reynolds number, and thus

substantiate the former conclusion that the dynamic-stall vortex on the VR-7 airfoil can be suppressed by the addition of a leading-edge slat.

## REFERENCES

1. Ham, N. D.; and Young, M. I.: Torsional Oscillation of Helicopter Blades Due to Stall. *J. Aircraft*, vol. 3, no. 3, 1966, pp. 218-224.
2. Ham, N. D.: Aerodynamic Loading on a Two-Dimensional Airfoil during Dynamic Stall. *AIAA J.*, vol. 6, no. 10, 1968, pp. 1927-1934.
3. Prouty, R. W.: The Whys and Whats of Pitch-Link Loads. *Rotor & Wing International*, vol. 22, no. 10, 1988, pp. 17-19.
4. Prouty, R. W.: Vibration Criteria: Finding Discomfort Levels. *Rotor & Wing International*, vol. 26, no. 3, 1992, pp. 94-96.
5. McCroskey, W. J.: Unsteady Airfoils. *Ann. Rev. Fluid Mechanics*, vol. 14, 1982, pp. 285-311.
6. McAlister, K. W.; Pucci, S. L.; McCroskey, W. J.; and Carr, L. W.: An Experimental Study of Dynamic Stall on Advanced Airfoil Sections, Volume 2. Pressure and Force Data. NASA TM-84245, 1982.
7. Carr, L. W.; and McAlister, K. W.: The Effect of a Leading-Edge Slat on the Dynamic Stall of an Oscillating Airfoil. AIAA Paper 83-2533, AIAA/AHS Aircraft Design, System & Operations Meeting, 1983.
8. Olson, L. E.: Optimization of Multi-Element Airfoils for Maximum Lift. NASA CP-2045, Part 2, 1978.
9. Lachmann, G. V.: Sir Frederick Handley-Page, The Man and His Work. *J. Royal Aeronautical Society*, vol. 68, no. 643, 1964, pp. 433-452.
10. Smith, A. M. G.: High-Lift Aerodynamics. *J. Aircraft*, vol. 12, no. 6, 1975, pp. 501-530.

11. Reynolds, W. C.; and Carr, L. W.: Review of Unsteady, Driven, Separated Flows. AIAA Paper 85-0527, AIAA Shear Flow Control Conference, Boulder, CO, 1985.
12. Rae, W. H.; and Pope, A.: Low-Speed Wind Tunnel Testing. John Wiley & Sons, Inc., 1984.
13. Dadone, L. U.: U.S. Army Helicopter Design Datcom, Volume 1 – Airfoils. USAAMRDL CR 76-2, 1976.
14. Schlichting, H.: Boundary-Layer Theory. McGraw-Hill Book Co., 1968.
15. McAlister, K. W.; Carr, L. W.; and McCroskey, W. J.: Dynamic Stall Experiments on the NACA 0012 Airfoil. NASA TP-1100, 1978.
16. McAlister, K. W.; and Carr, L. W.: Water Tunnel Visualizations of Dynamic Stall. Transactions of the ASME, J. Fluids Engineering, vol. 101, 1979, pp. 376–380.
17. Hoerner, S. F.: Fluid-Dynamic Drag. Hoerner Fluid Dynamics, Brick Town, N.J., 1975.

Table 1. VR-7 steady data at  $Re = 200K$

Frame		$a$ , deg
Without slat	With slat	
14970	14640	0
14971	14656	2
14972	14644	4
14973	14659	6
14974	14647	8
14975	14662	10
14982	14650	12
14983	14665	14
14984	14653	16
14985		17
14986	14668	18
14987		19
14994	14671	20
	14674	21
14995	14677	22
	14680	23
14996	14684	24
14997	14687	26
14998	14690	28
14999	14693	30

Table 2. Basic VR-7 time-history data at  $Re = 200K$

Frame	$a$ , deg
12059	0
12064	5
12068	10
12077	15
12084	20
12088	25

Table 3. VR-7 unsteady data

Frame		Cycles averaged	Mean angle	Amplitude	Re	k
Without slat	With slat					
24883	24542	100	15	10	100K	0.10
24885	24560	100	15	10	150K	0.10
24887	24633	100	15	10	200K	0.10
24890	24522	100	15	10	250K	0.10
24900	24616	5	15	10	200K	0.001
24901	24620	15	15	10	200K	0.005
24906	24624	50	15	10	200K	0.025
24908	24626	100	15	10	200K	0.05
24913	24635	100	15	10	200K	0.15
24915	24638	100	15	10	200K	0.20
24923	24731	100	10	10	200K	0.10
24930	24612	100	20	10	200K	0.10
14963	24698	5	15	15	200K	0.003

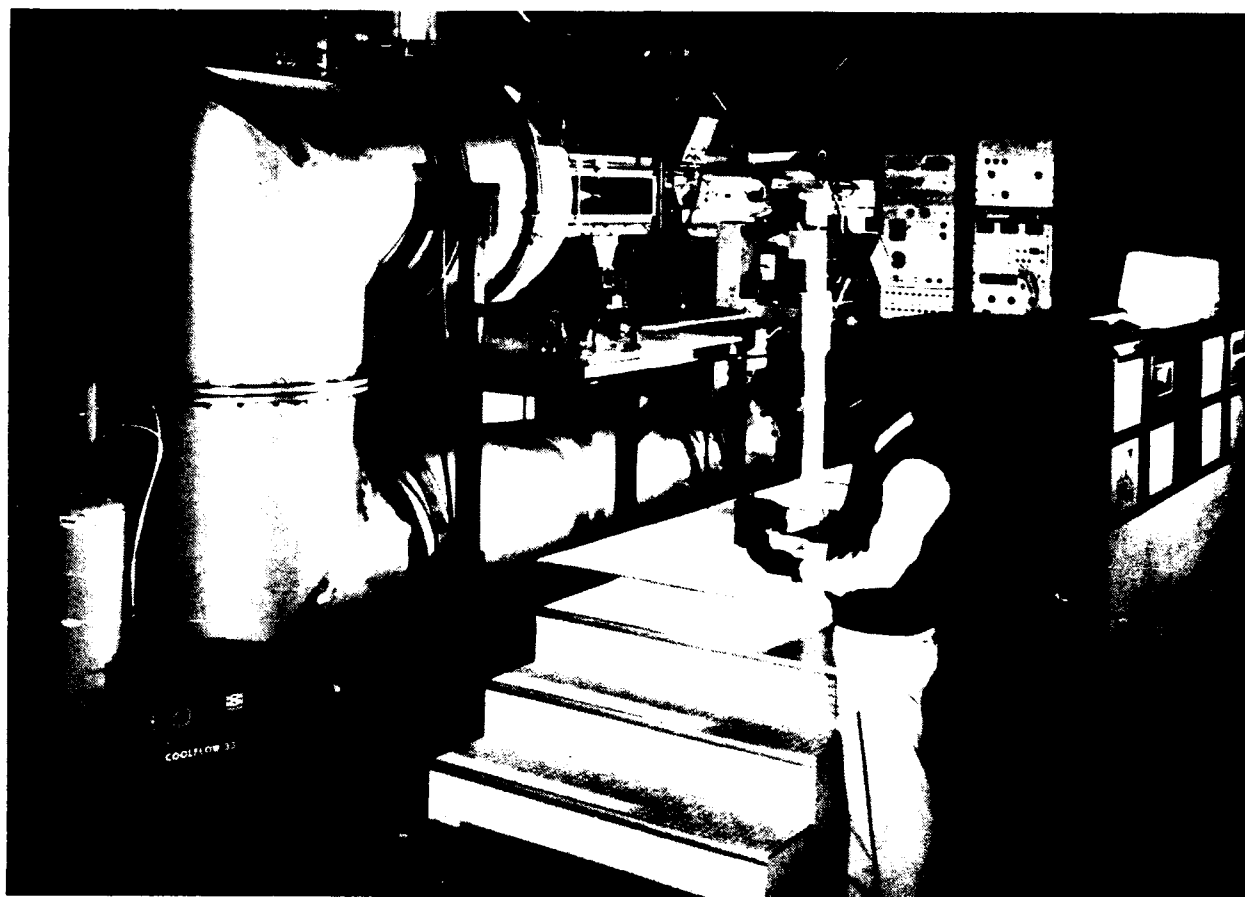


Figure 1. Aeroflightdynamics 8- by 12-in. Water Tunnel.

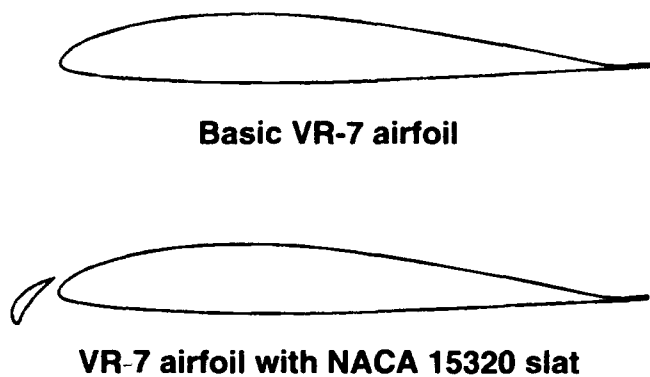


Figure 2. VR-7 airfoil with and without leading-edge slat.

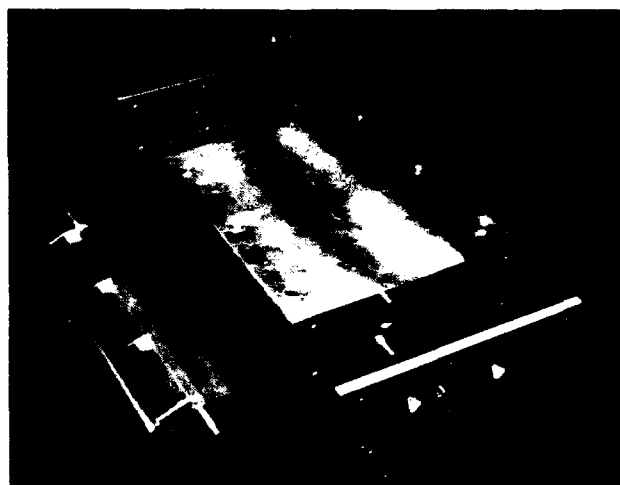


Figure 3. Slat and spar assembly alongside mold for VR-7 airfoil.

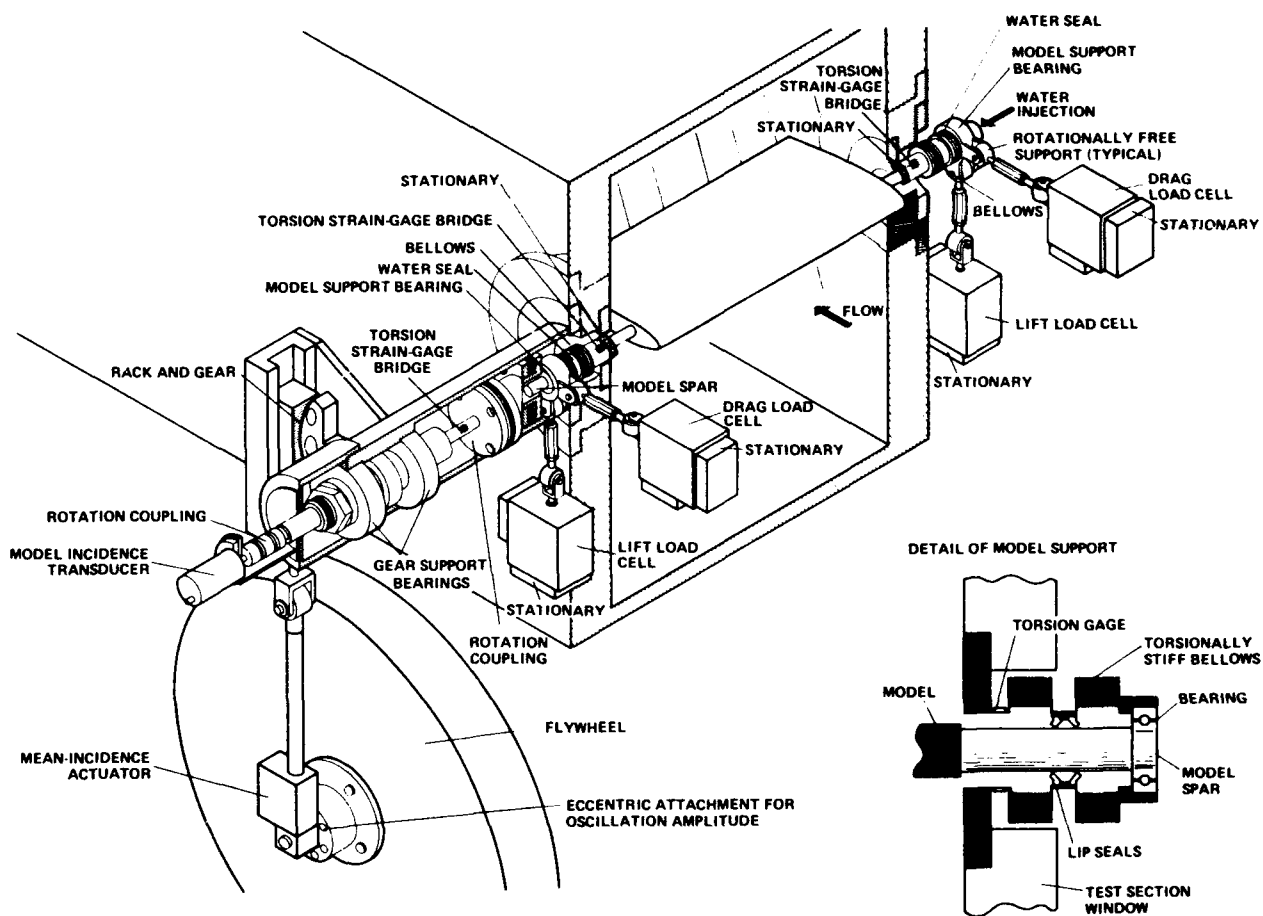


Figure 4. Model installation and balance system for force and moment measurements.

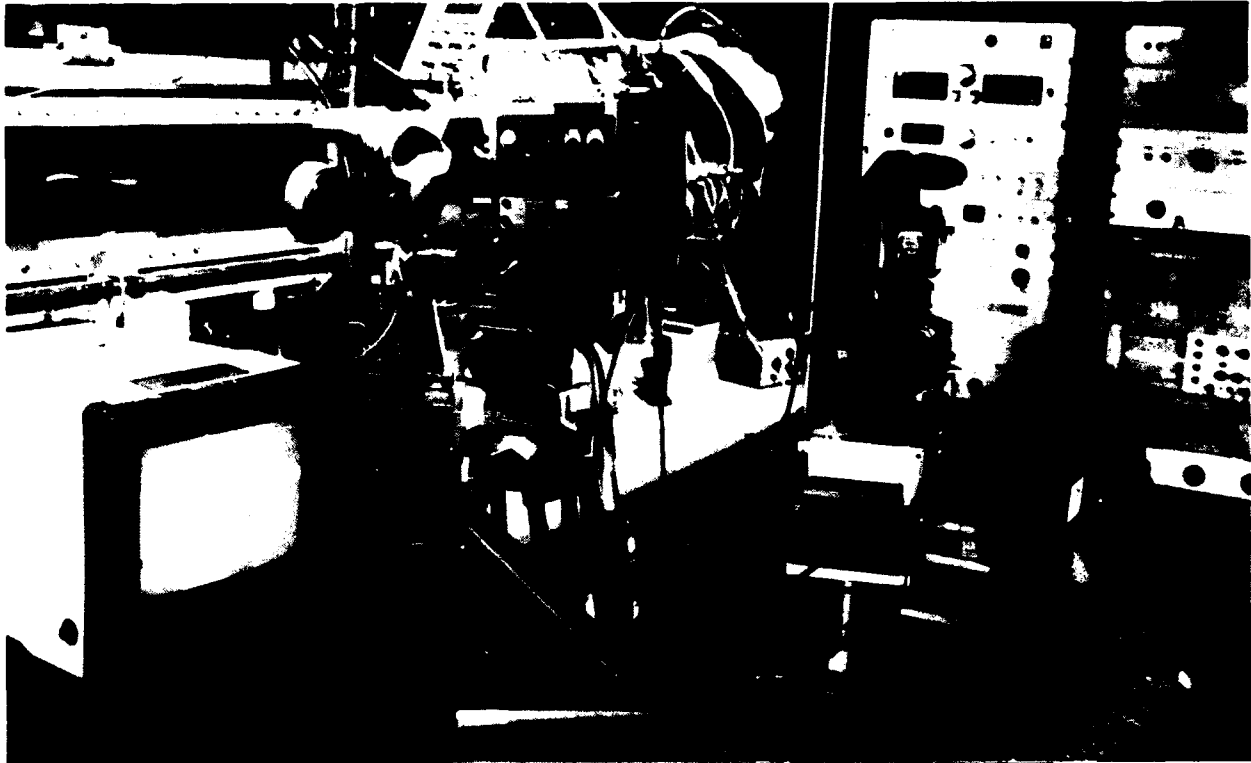


Figure 5. Placement of cameras during flow visualization studies.

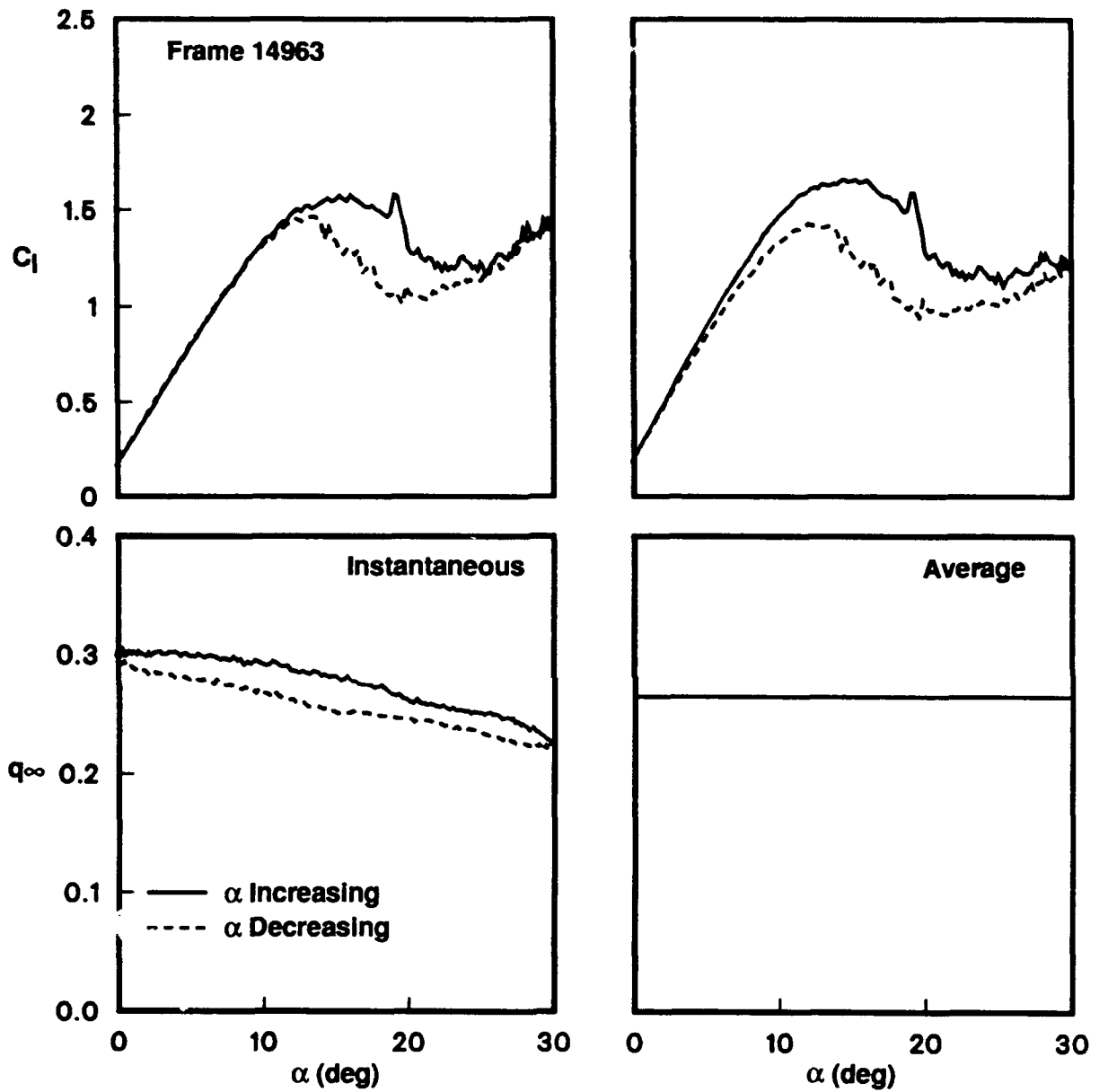


Figure 6. Consequence of using average  $q_\infty$  instead of the instantaneous value for the basic VR-7 airfoil at  $Re = 200K$  and  $k = 0.003$  with  $\alpha = 15^\circ + 15^\circ \sin(\omega t)$ .

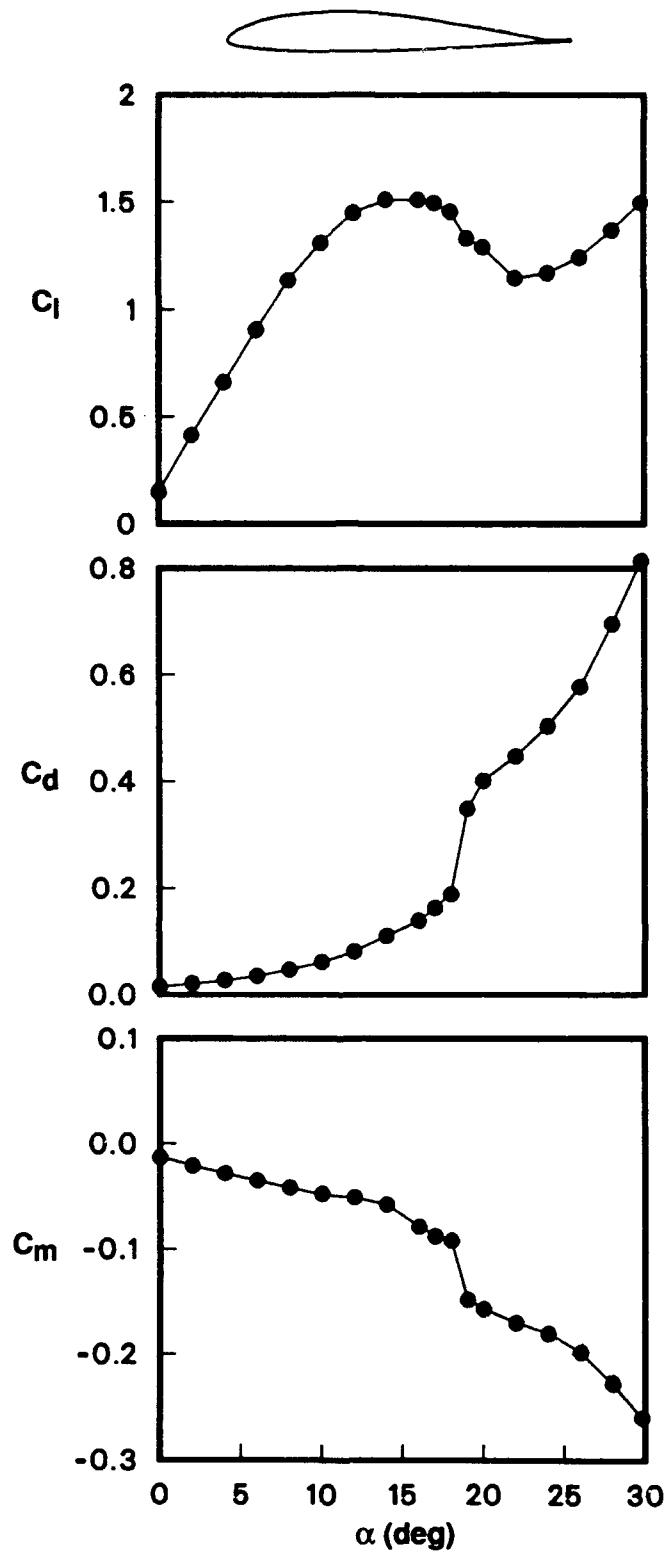


Figure 7. Steady data for the basic NACA 23012 airfoil at  $Re = 0.2 \times 10^6$ .

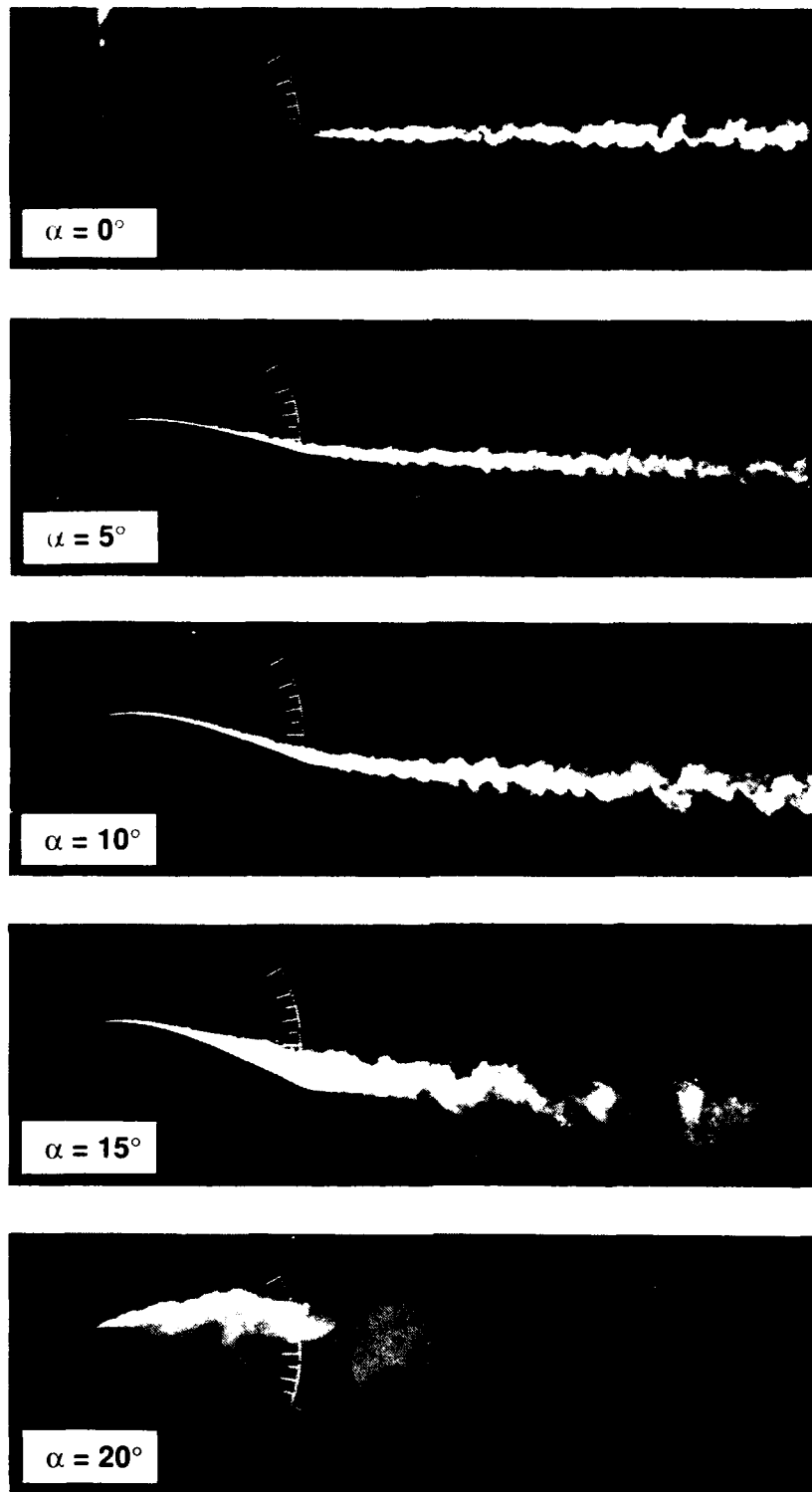
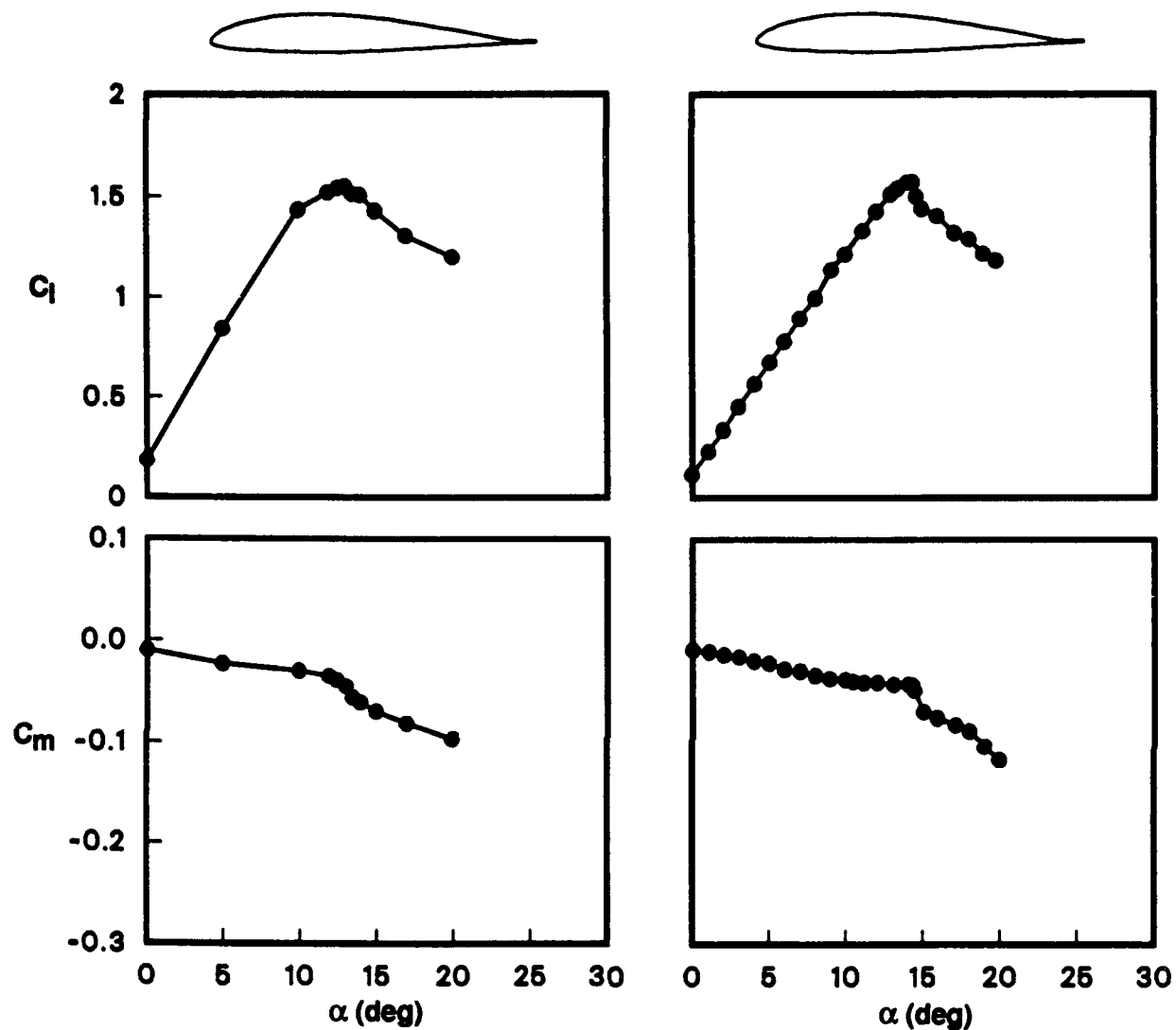


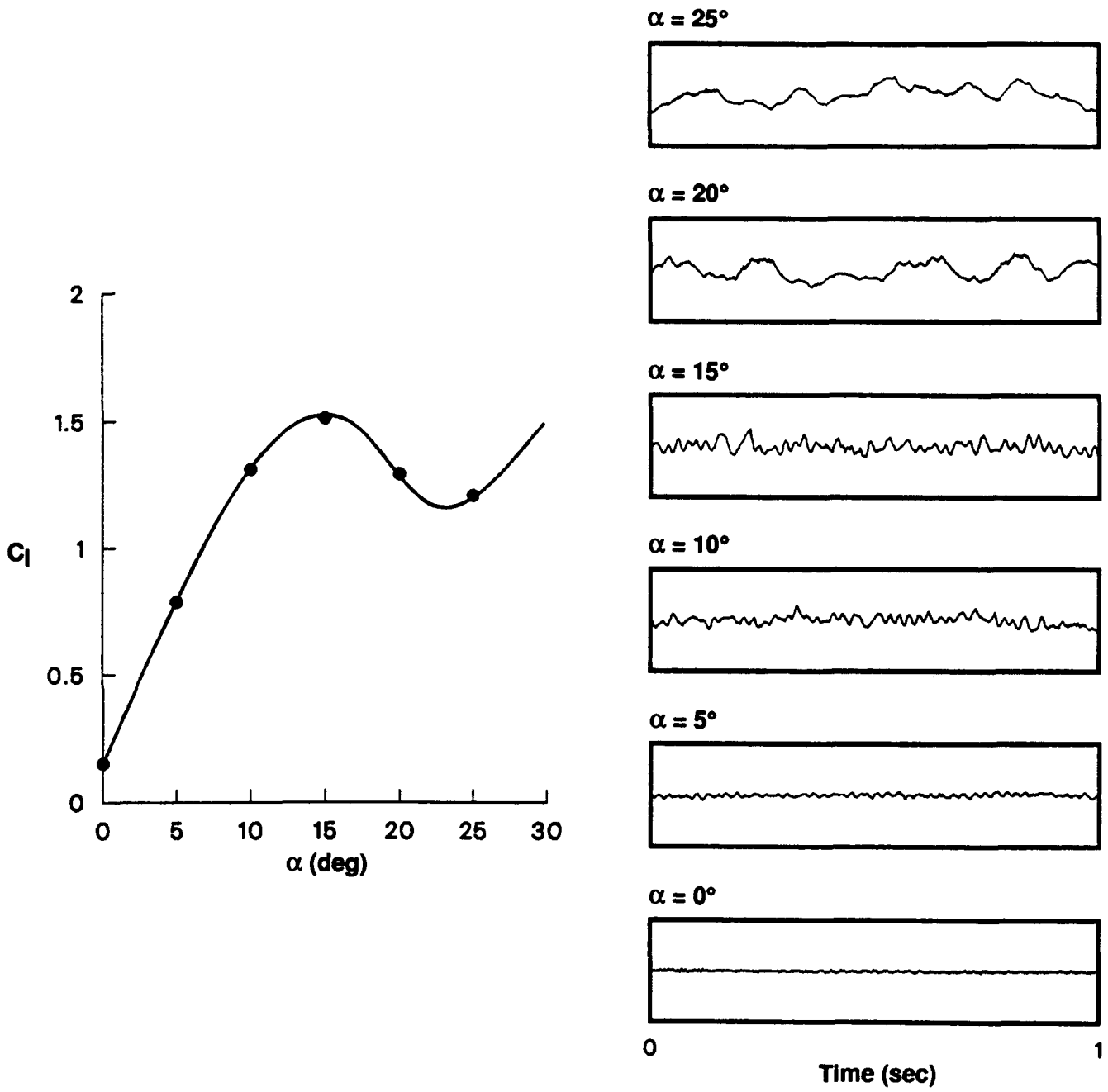
Figure 8. Boundary layer and wake visualization for the basic VR-7 airfoil at  $Re = 0.2 \times 10^6$  with fixed angles of attack.



(a) Wind tunnel data (ref. 6) at  $Re = 1.5 \times 10^6$  and  $M_\infty = 0.11$ .

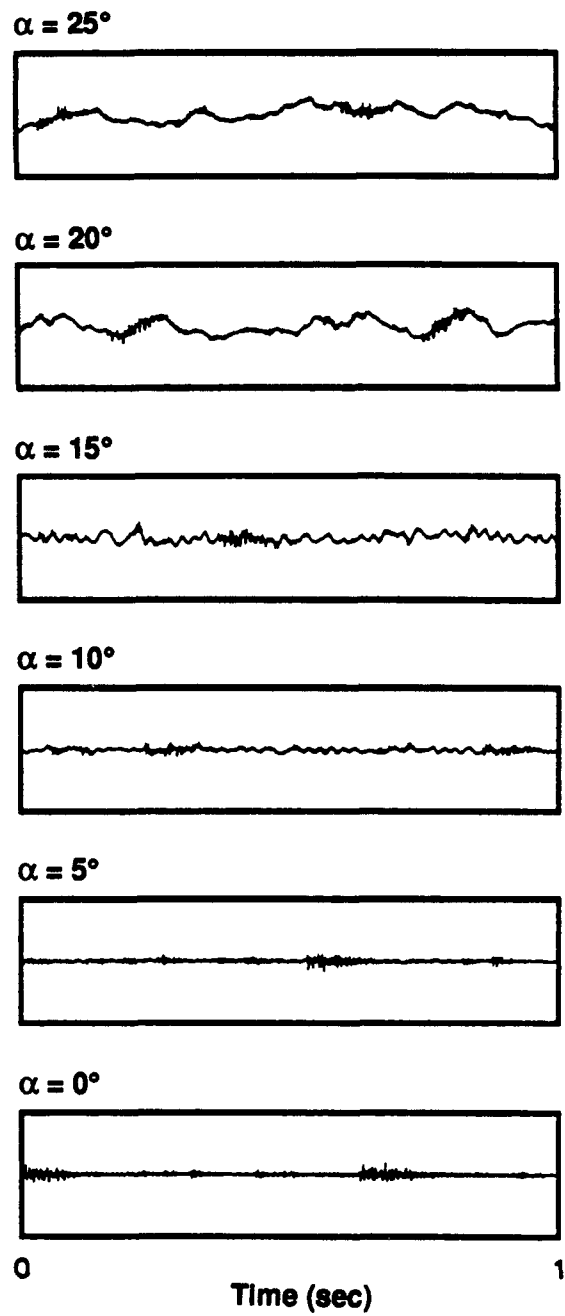
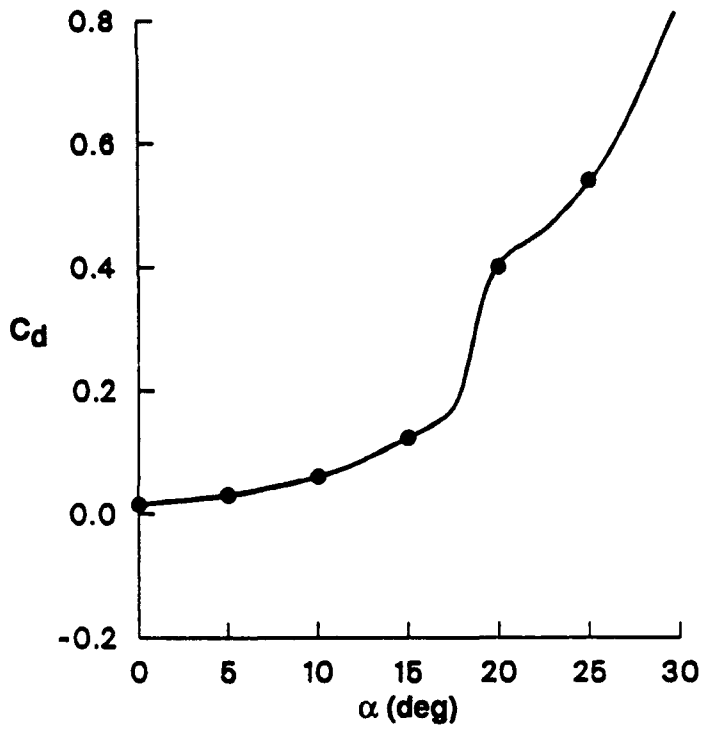
(b) Wind tunnel data (ref. 13) at  $Re = 5.7 \times 10^6$  and  $M_\infty = 0.30$ .

Figure 9. Steady data for the basic VR-7 airfoil from wind tunnel tests.



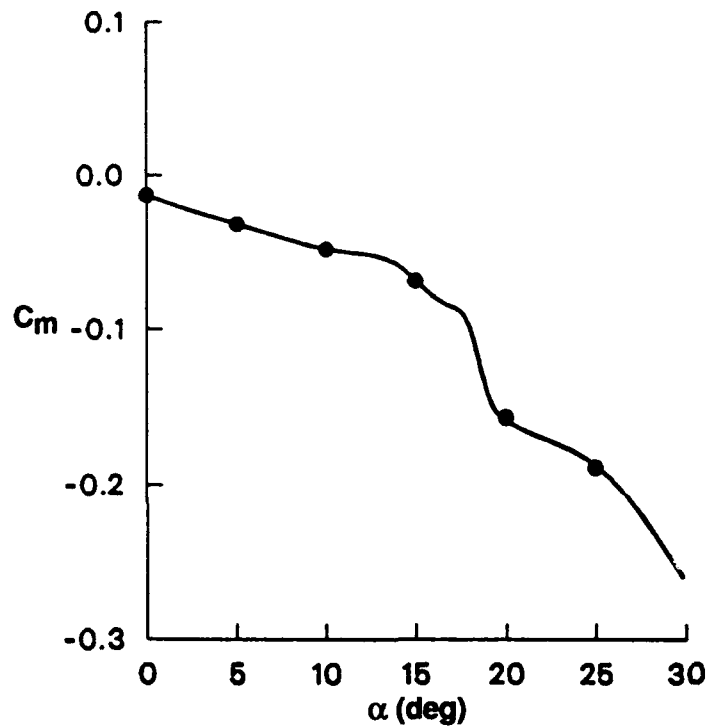
(a) Lift.

Figure 10. Time history of loads over 1-sec interval for basic VR-7 airfoil at  $Re = 0.2 \times 10^6$  at fixed angles of attack.



(b) Drag.

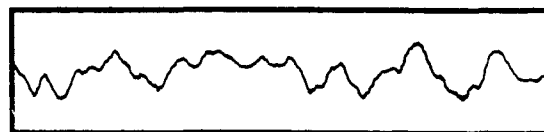
Figure 10. Continued.



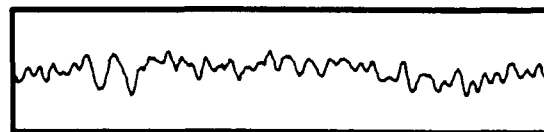
$\alpha = 25^\circ$



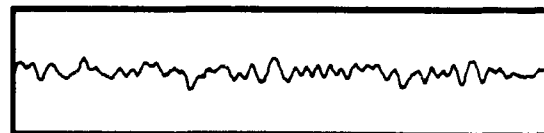
$\alpha = 20^\circ$



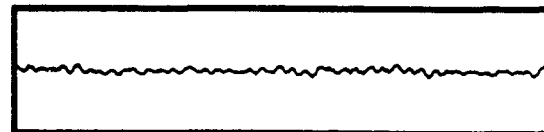
$\alpha = 15^\circ$



$\alpha = 10^\circ$



$\alpha = 5^\circ$



$\alpha = 0^\circ$



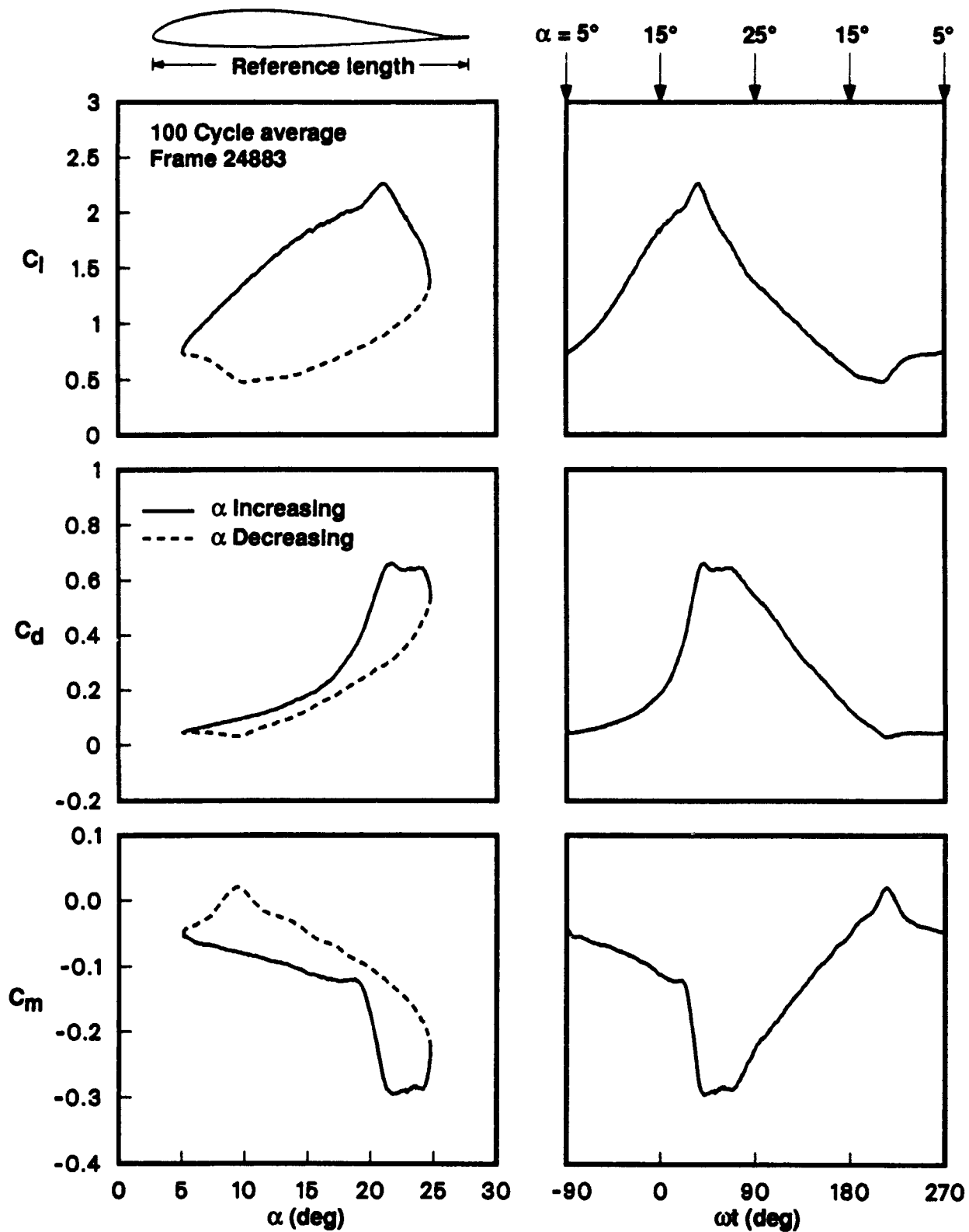
0

Time (sec)

1

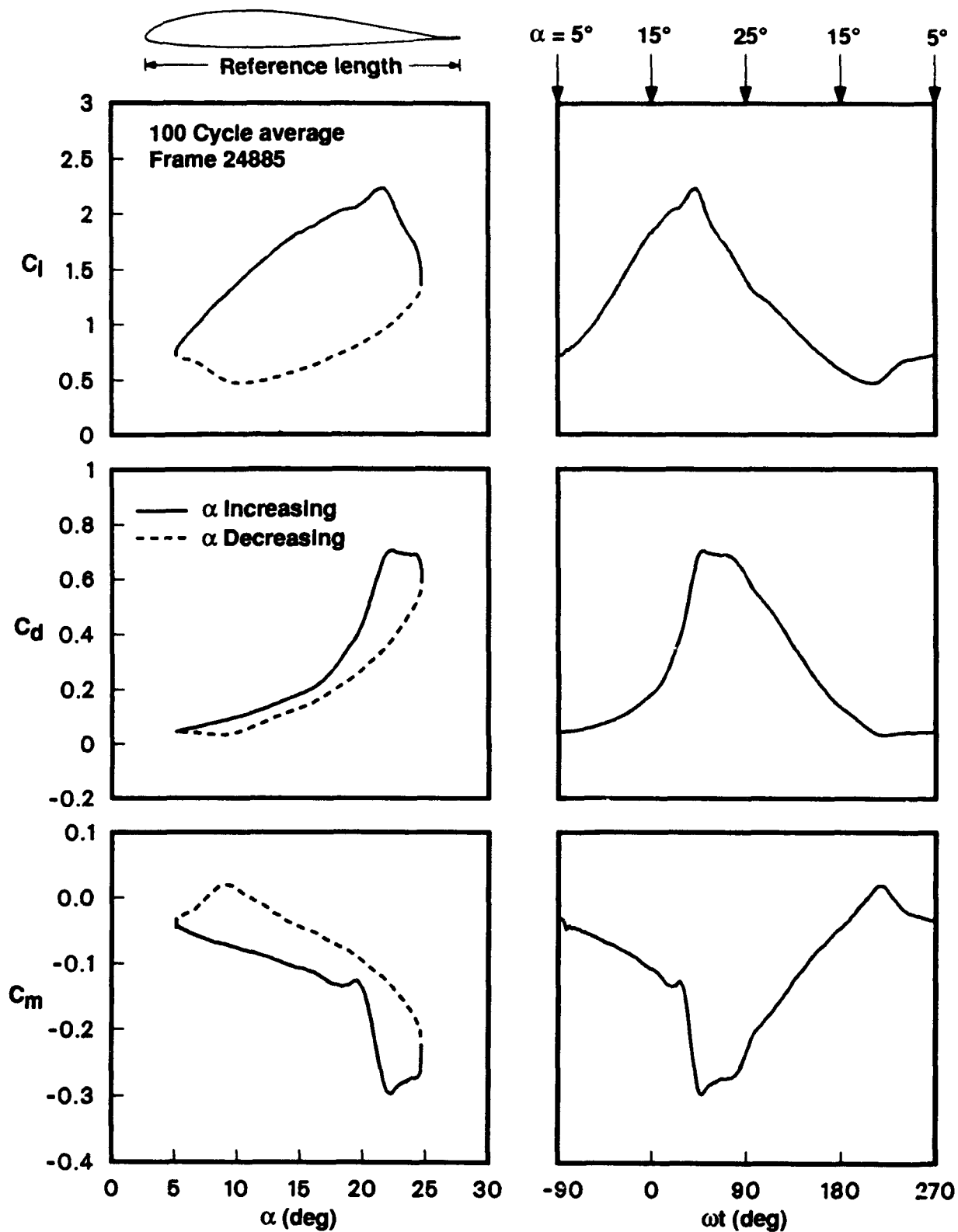
(c) Moment.

Figure 10. Concluded.



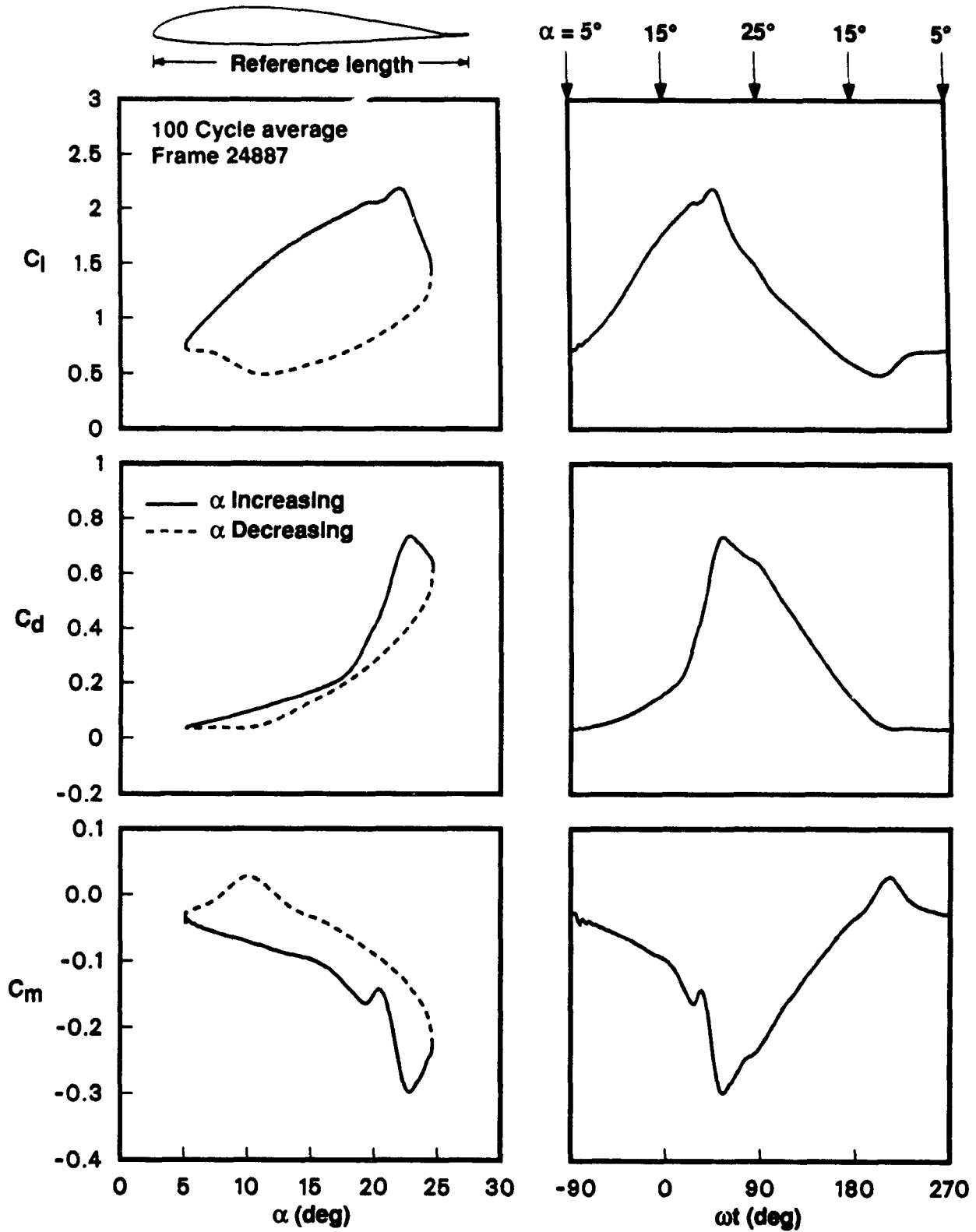
(a)  $Re = 100K$ .

Figure 11. Reynolds number effects on the basic VR-7 airfoil at  $k = 0.10$  with  $\alpha = 15^\circ + 10^\circ \sin(\omega t)$ .



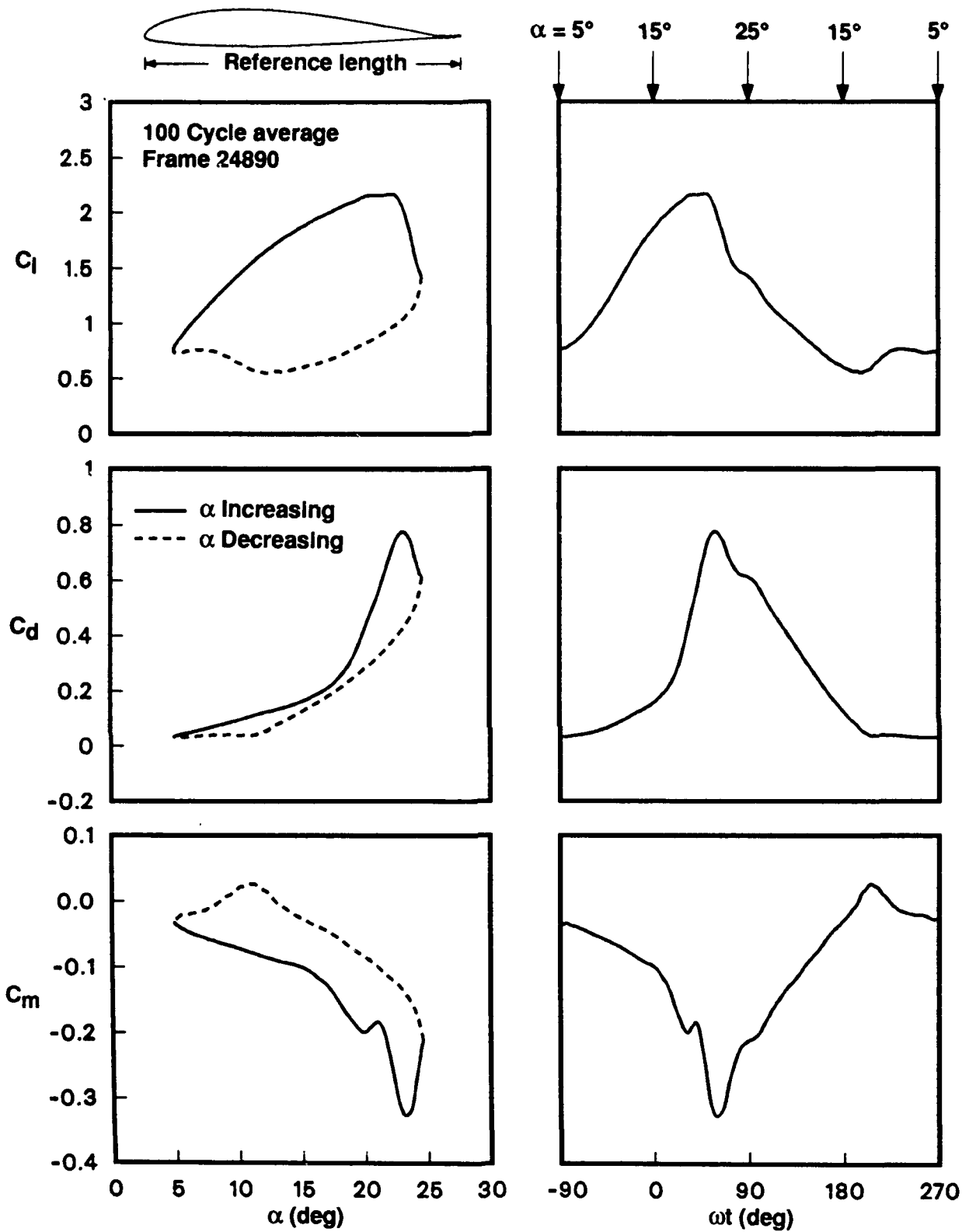
(b)  $Re = 150K$ .

Figure 11. Continued.



(c)  $Re = 200K$ .

Figure 11. Continued.



(d)  $Re = 250K$ .

Figure 11. Concluded.

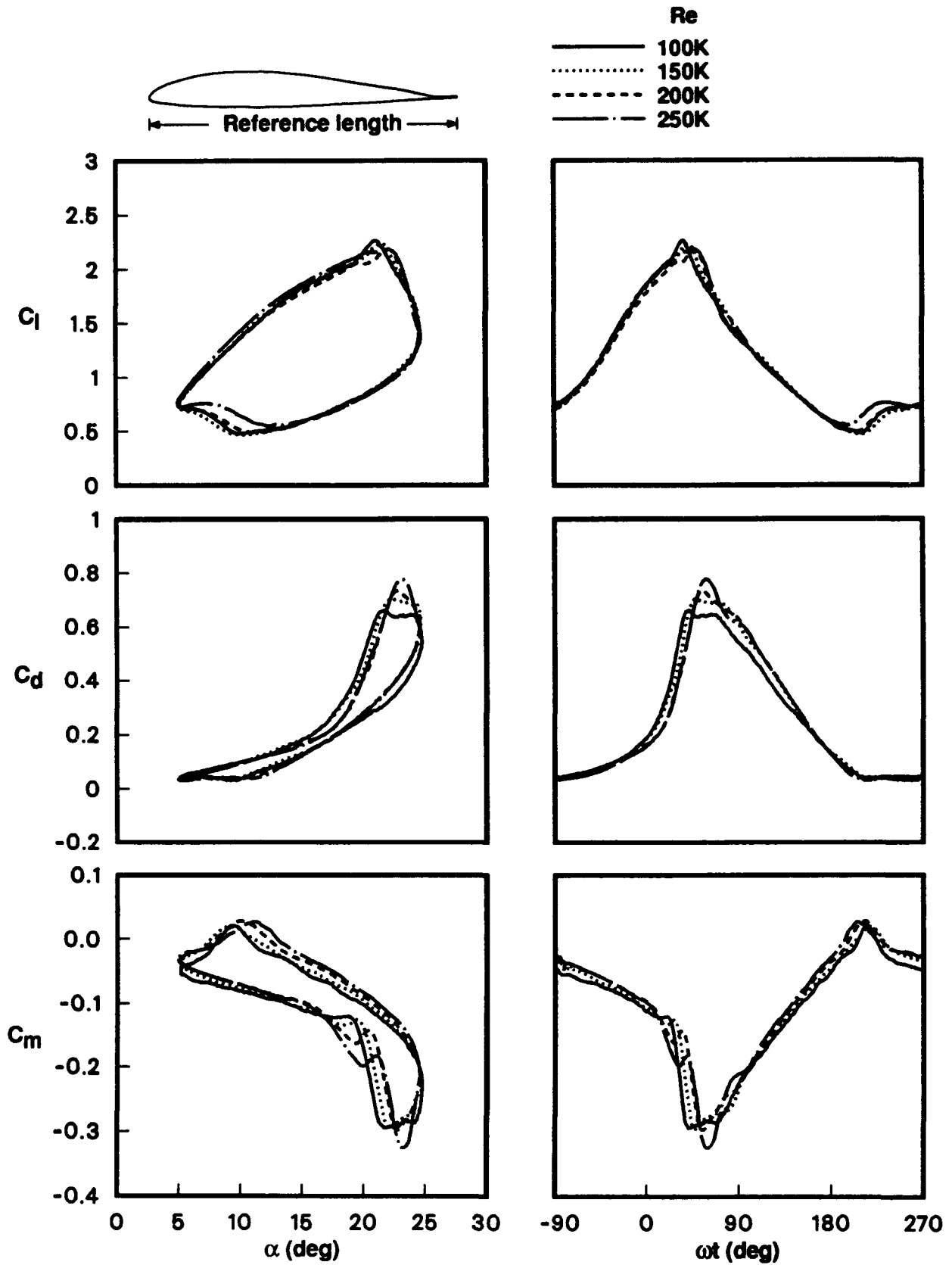
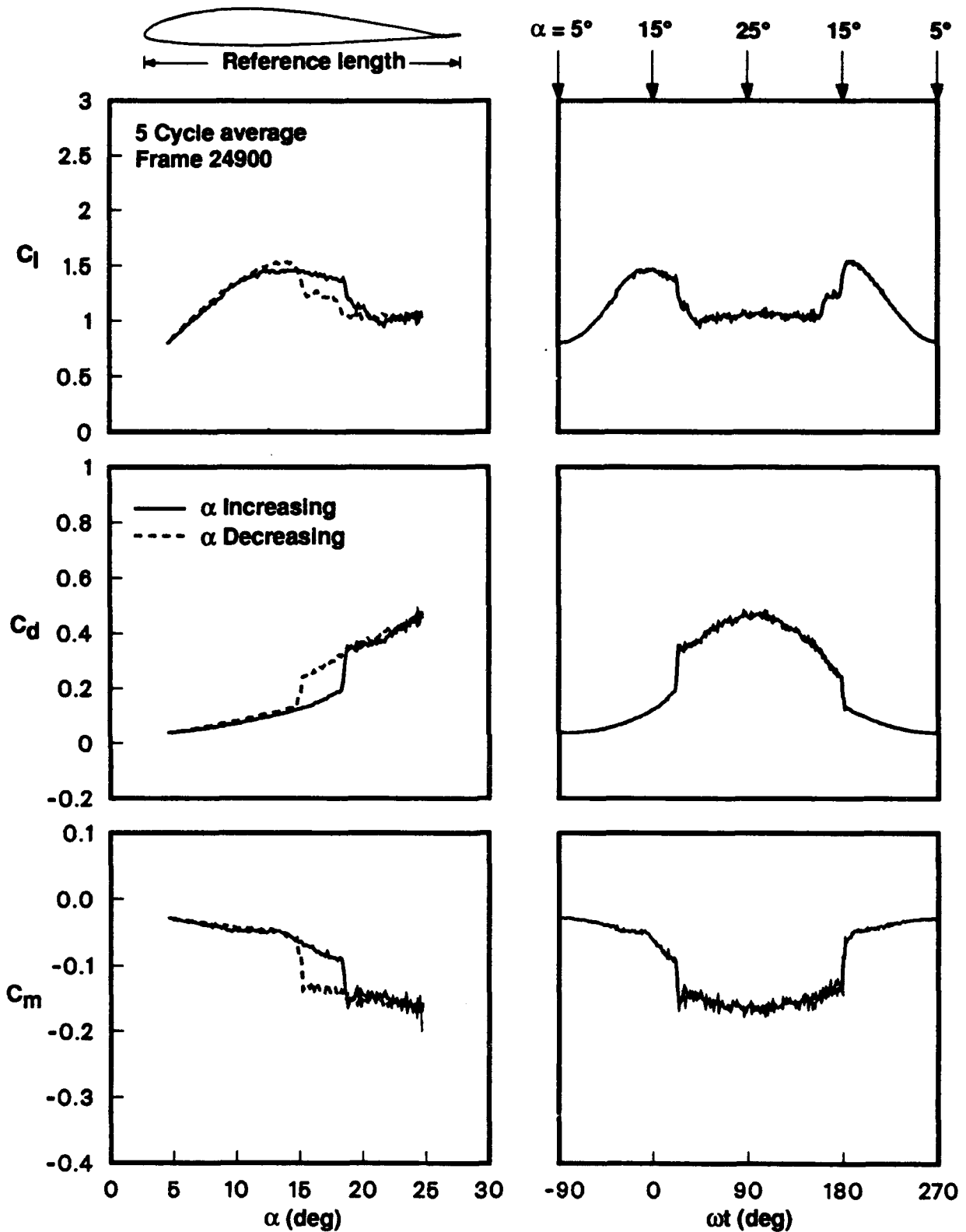
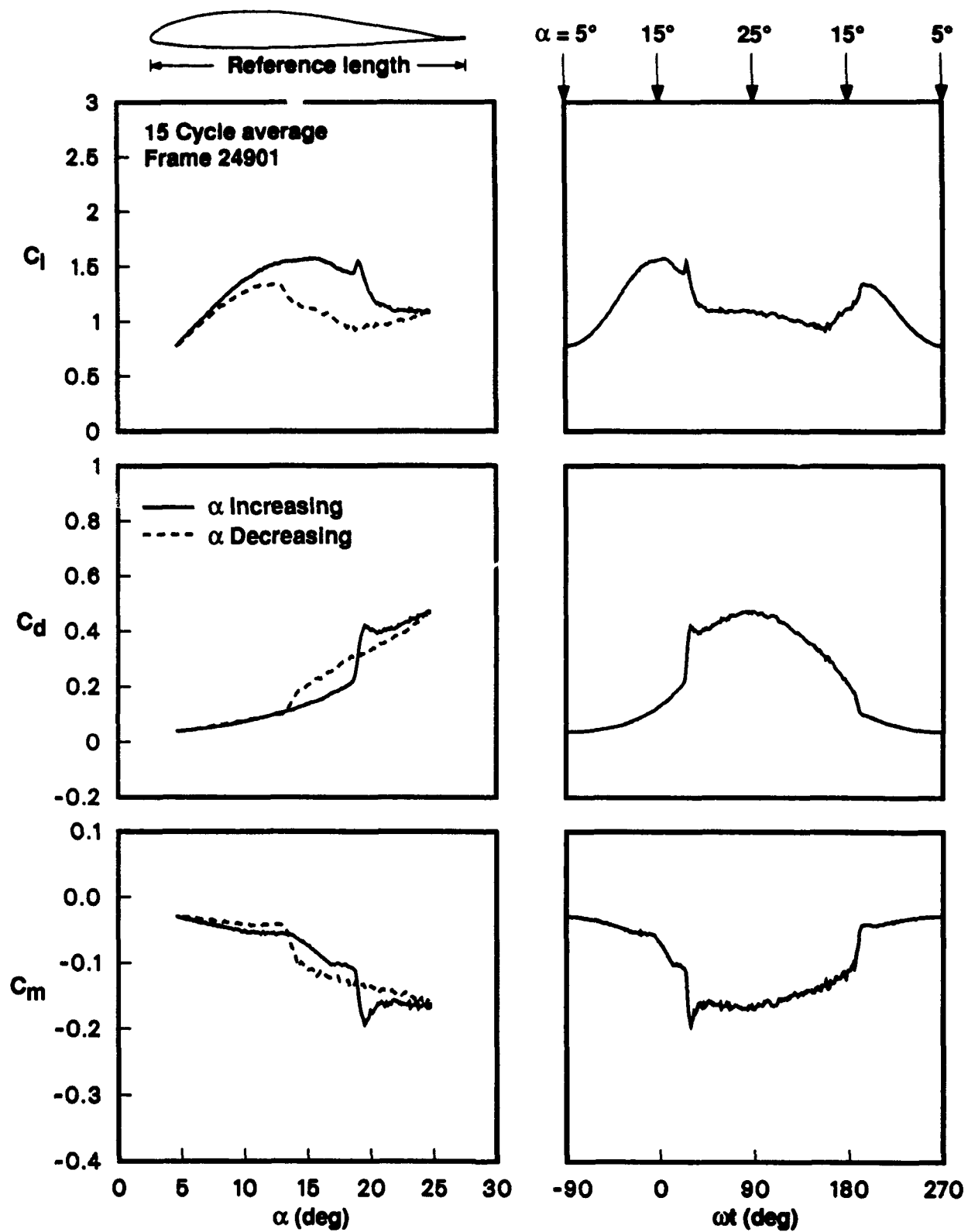


Figure 12. Superposition of results for  $Re = 100K \rightarrow 250K$  for the basic VR-7 airfoil at  $k = 0.10$  with  $\alpha = 15^\circ + 10^\circ \sin(\omega t)$ .



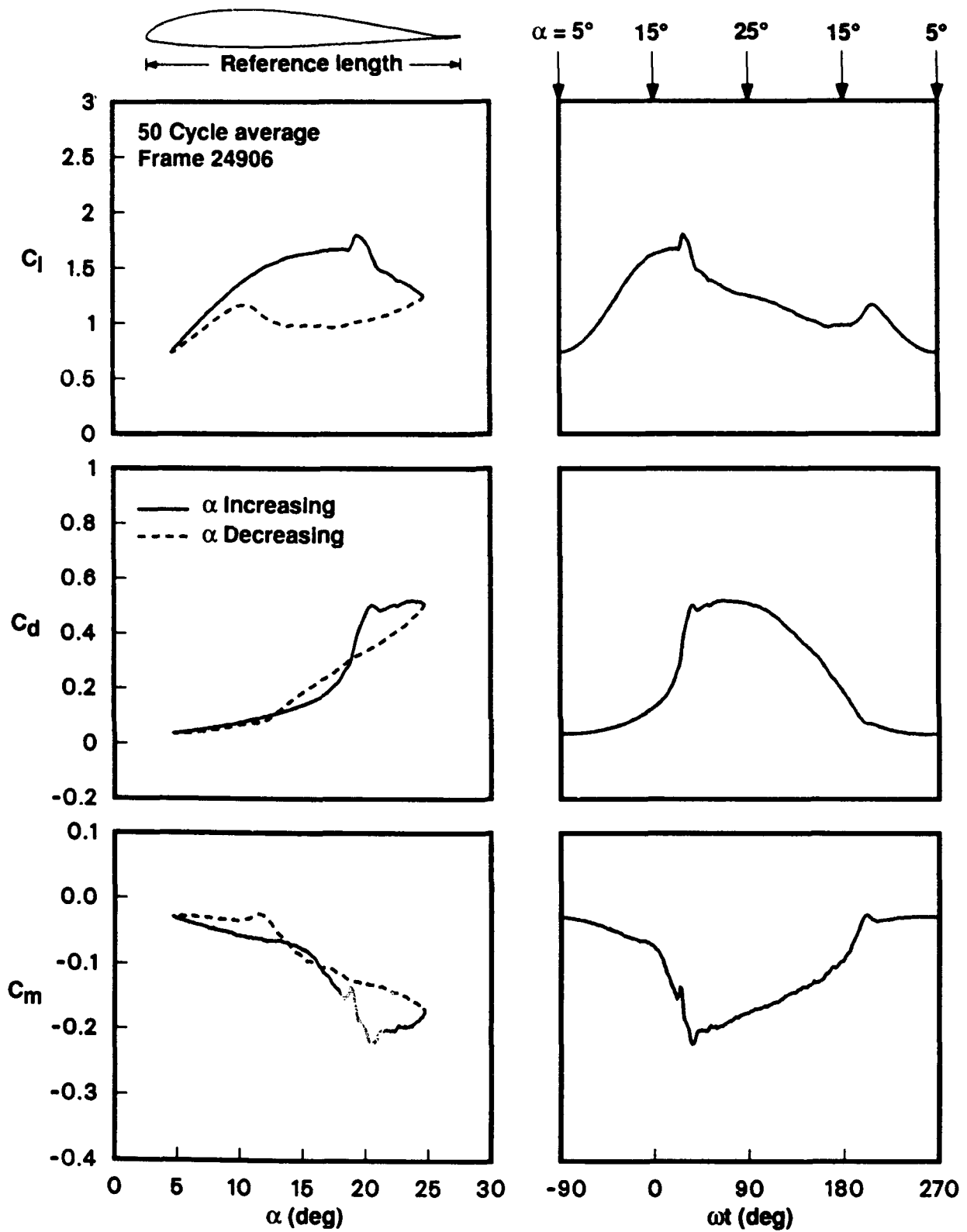
(a)  $k = 0.001$ .

Figure 13. Reduced frequency effects on the basic VR-7 airfoil at  $Re = 200K$  with  $\alpha = 15^\circ + 10^\circ \sin(\omega t)$ .



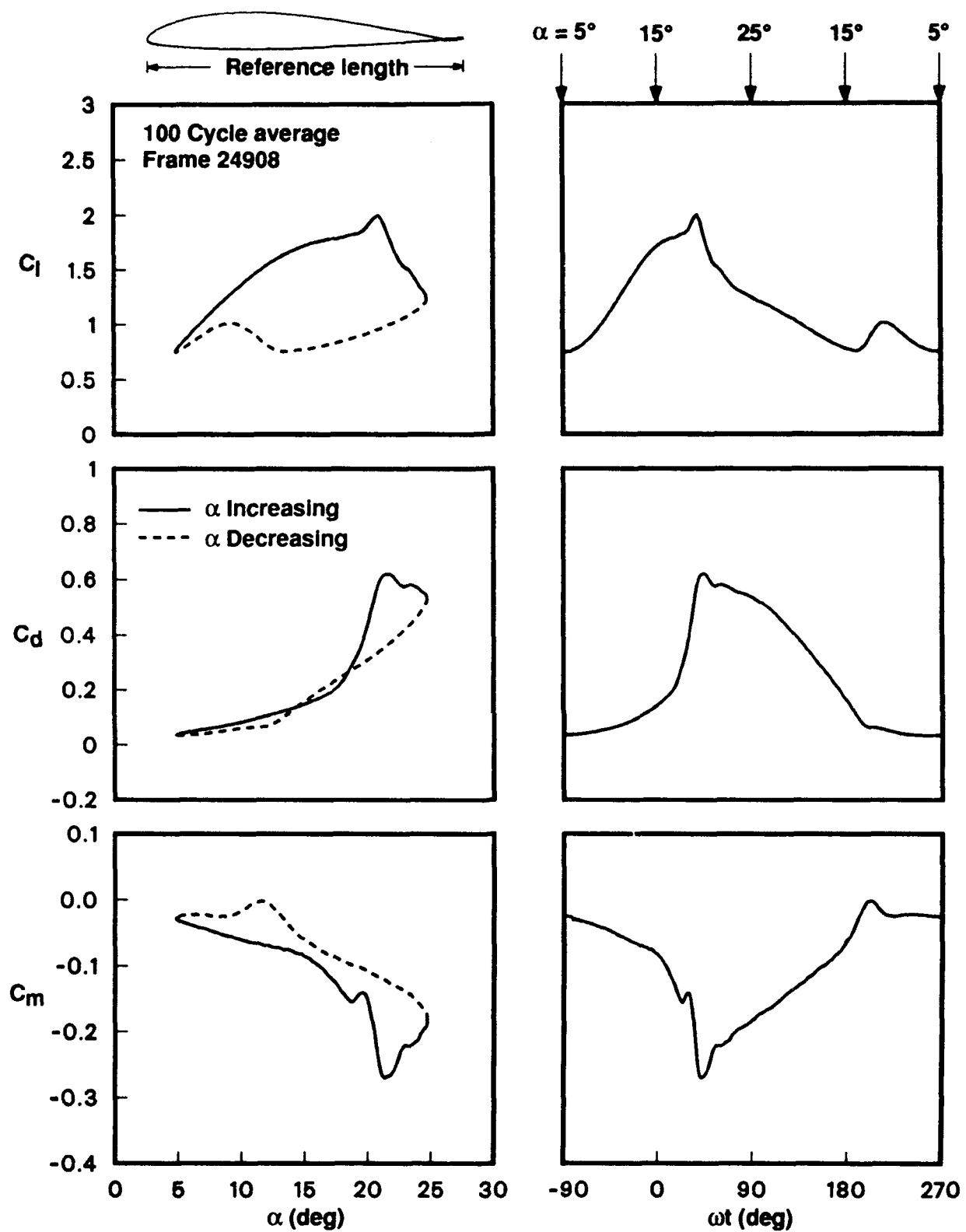
(b)  $k = 0.005$ .

Figure 13. Continued.



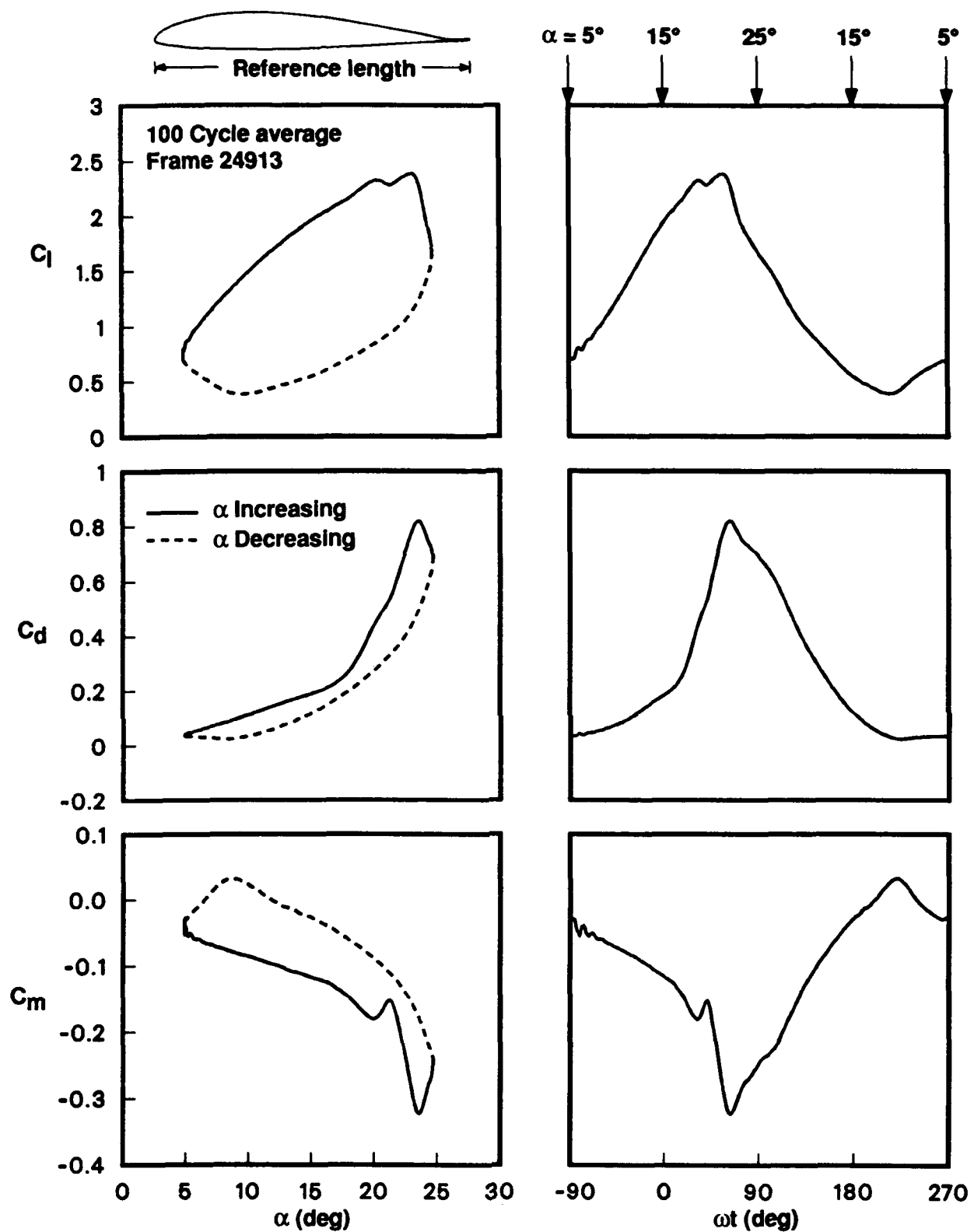
(c)  $k = 0.025$ .

Figure 13. Continued.



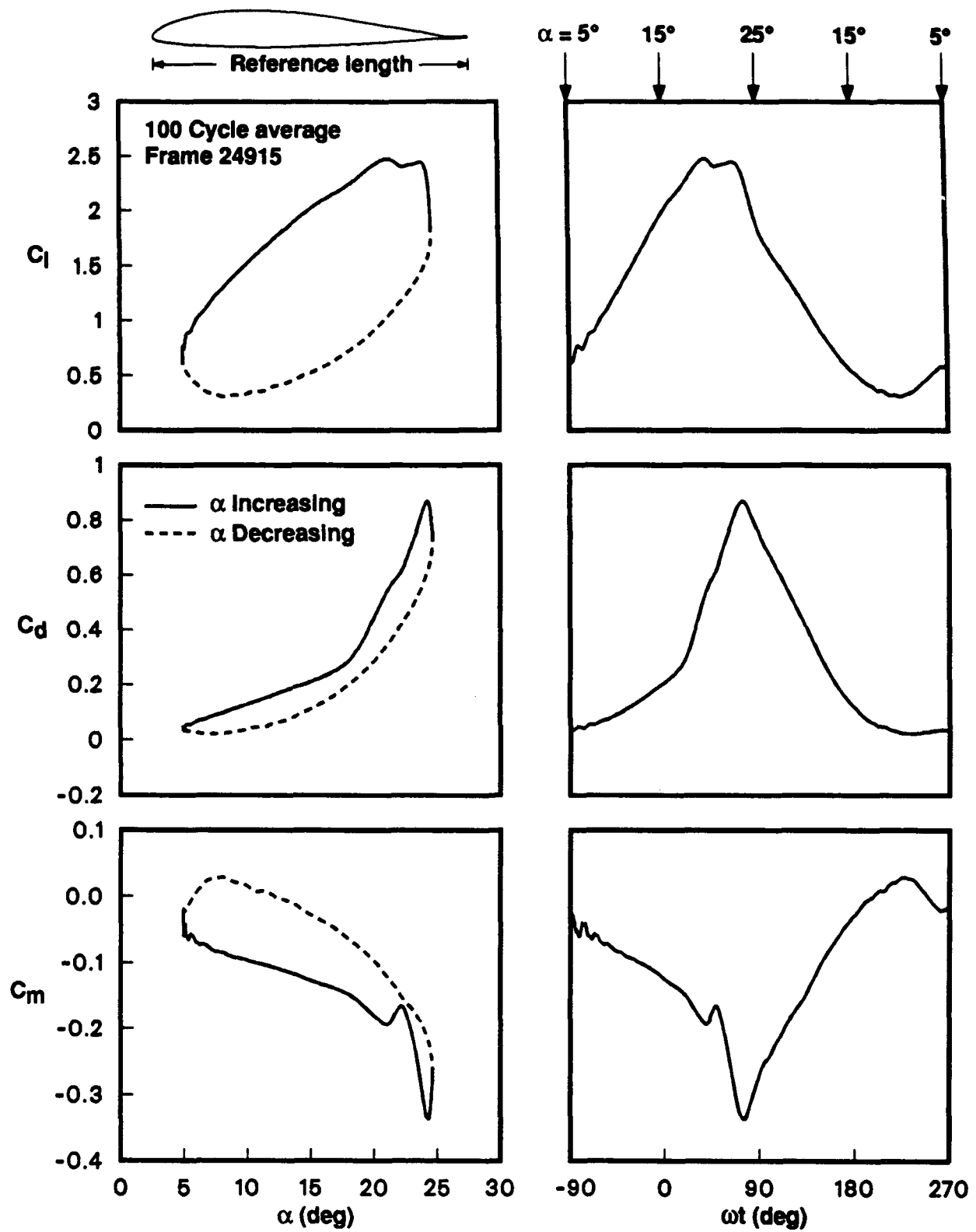
(d)  $k = 0.05$ .

Figure 13. Continued.



(e)  $k = 0.15$ .

Figure 13. Continued.



(f)  $k = 0.20$ .

Figure 13. Concluded.

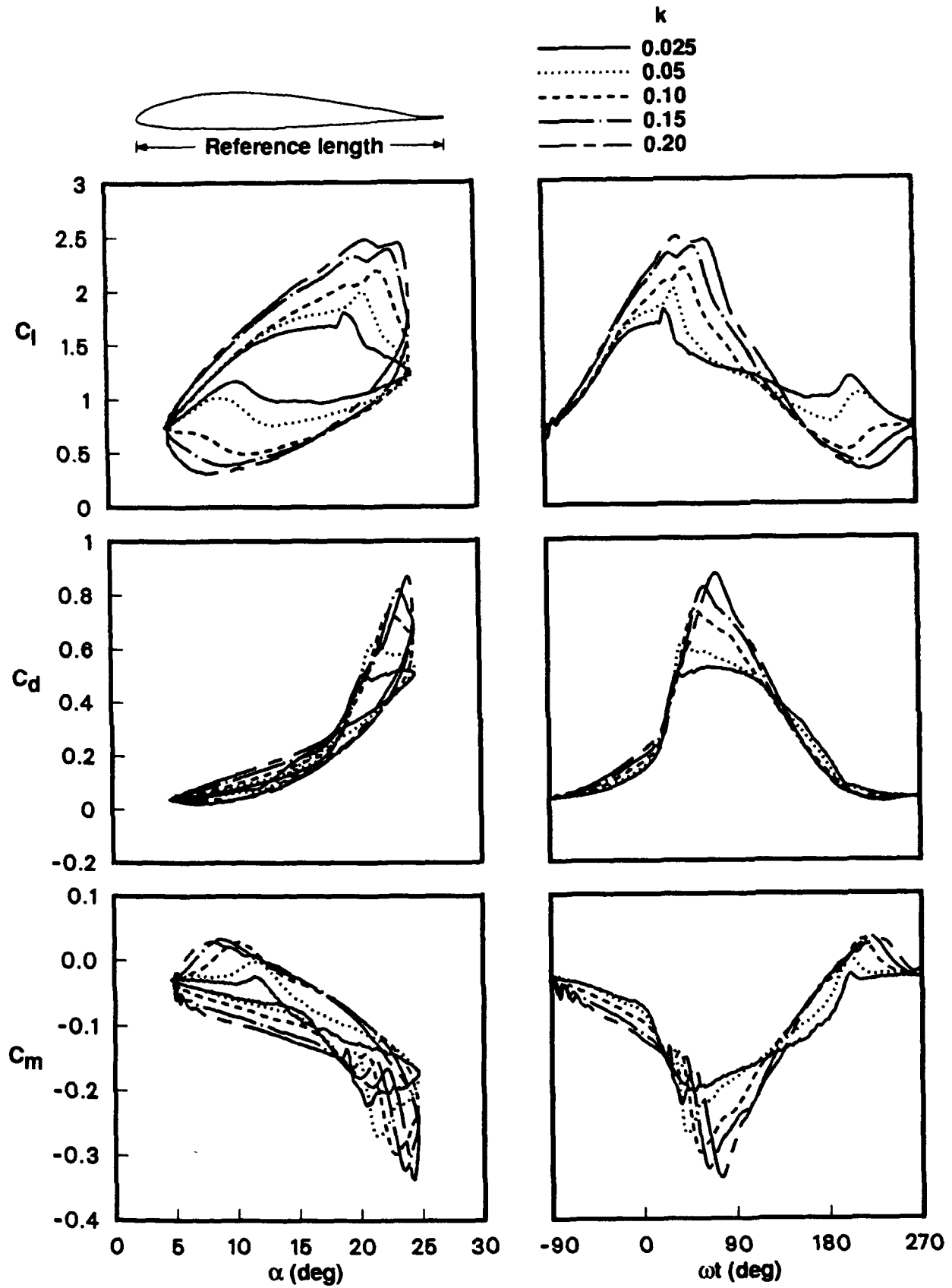


Figure 14. Superposition of results for  $k = 0.025 \rightarrow 0.20$  for the basic VR-7 airfoil at  $Re = 200K$  with  $\alpha = 15^\circ + 10^\circ \sin(\omega t)$ .

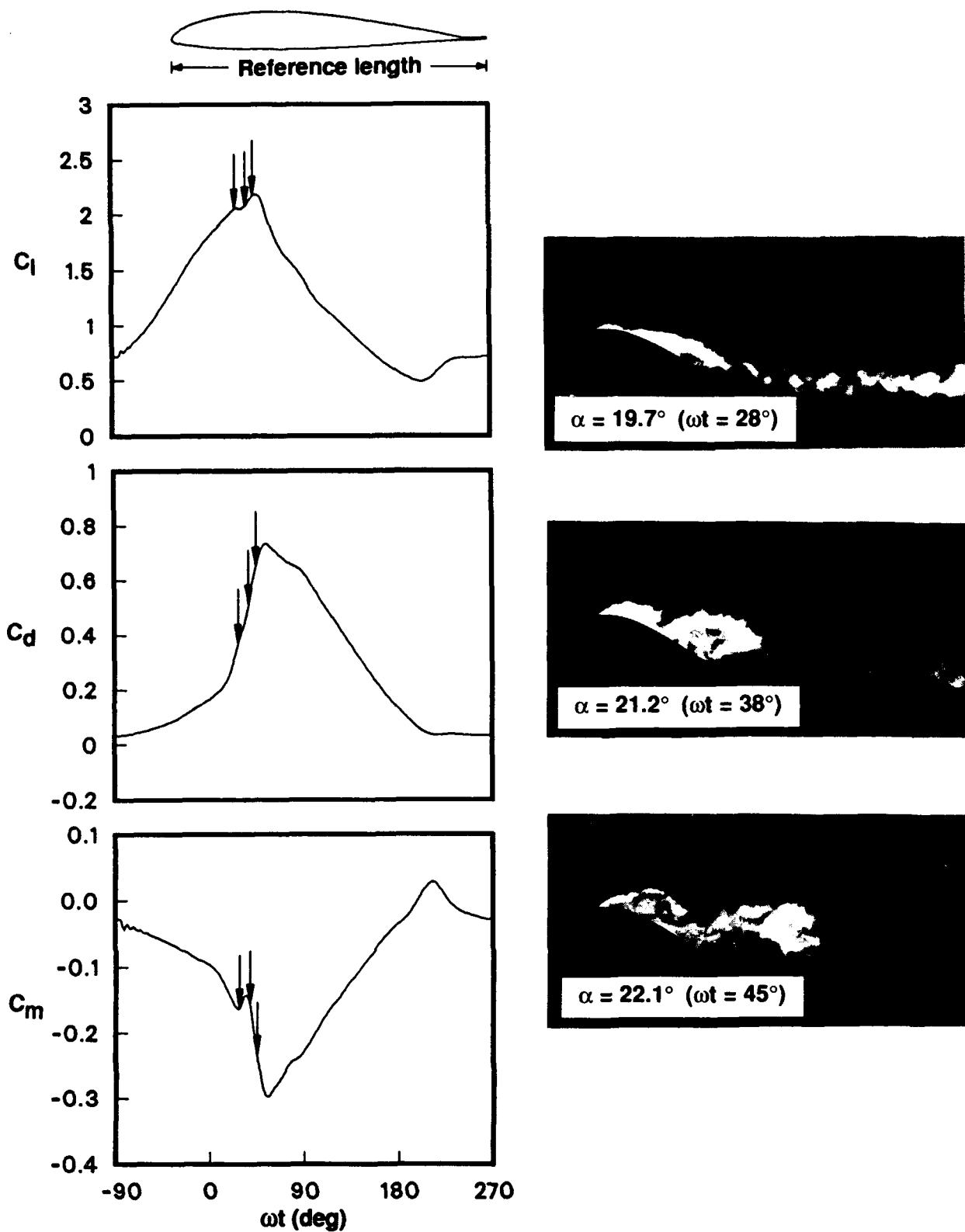


Figure 15. Development of stall vortex on the basic VR-7 airfoil at  $Re = 200K$  and  $k = 0.1$  with  $\alpha = 15^\circ + 10^\circ \sin(\omega t)$ .

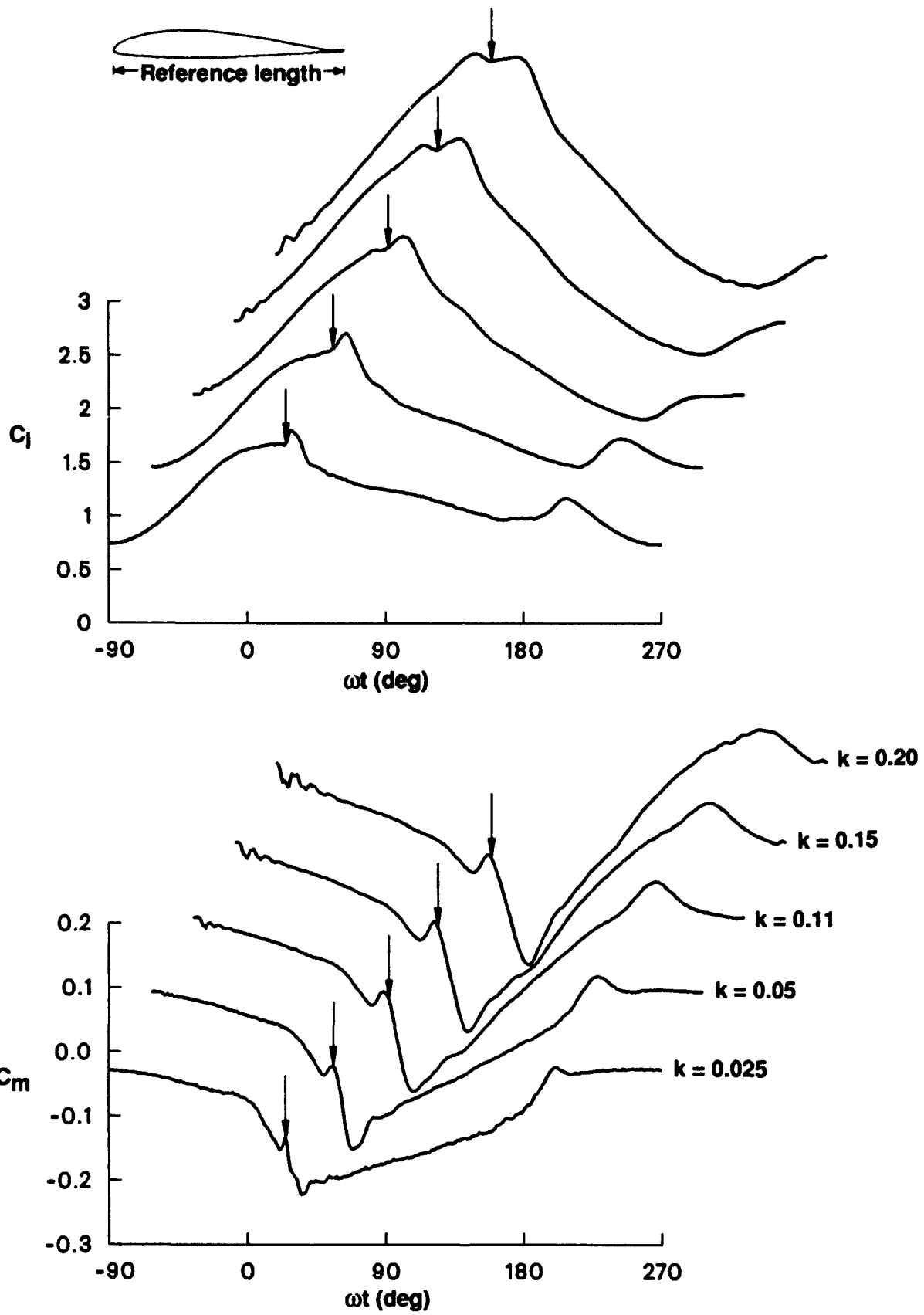


Figure 16. Movement of stall vortex past the quarter-chord of the basic VR-7 airfoil at  $Re = 200K$  with  $\alpha = 15^\circ + 10^\circ \sin(\omega t)$  over a range of  $k$ .

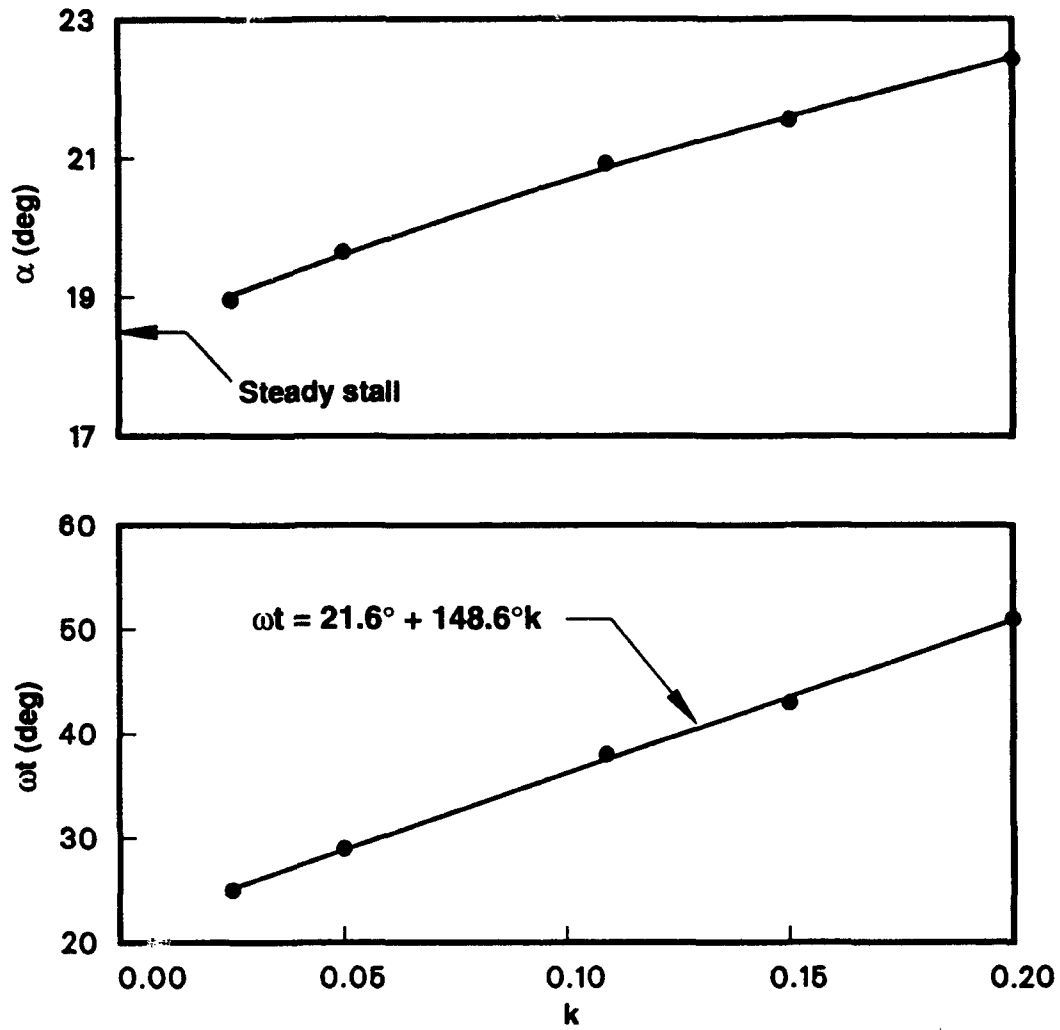
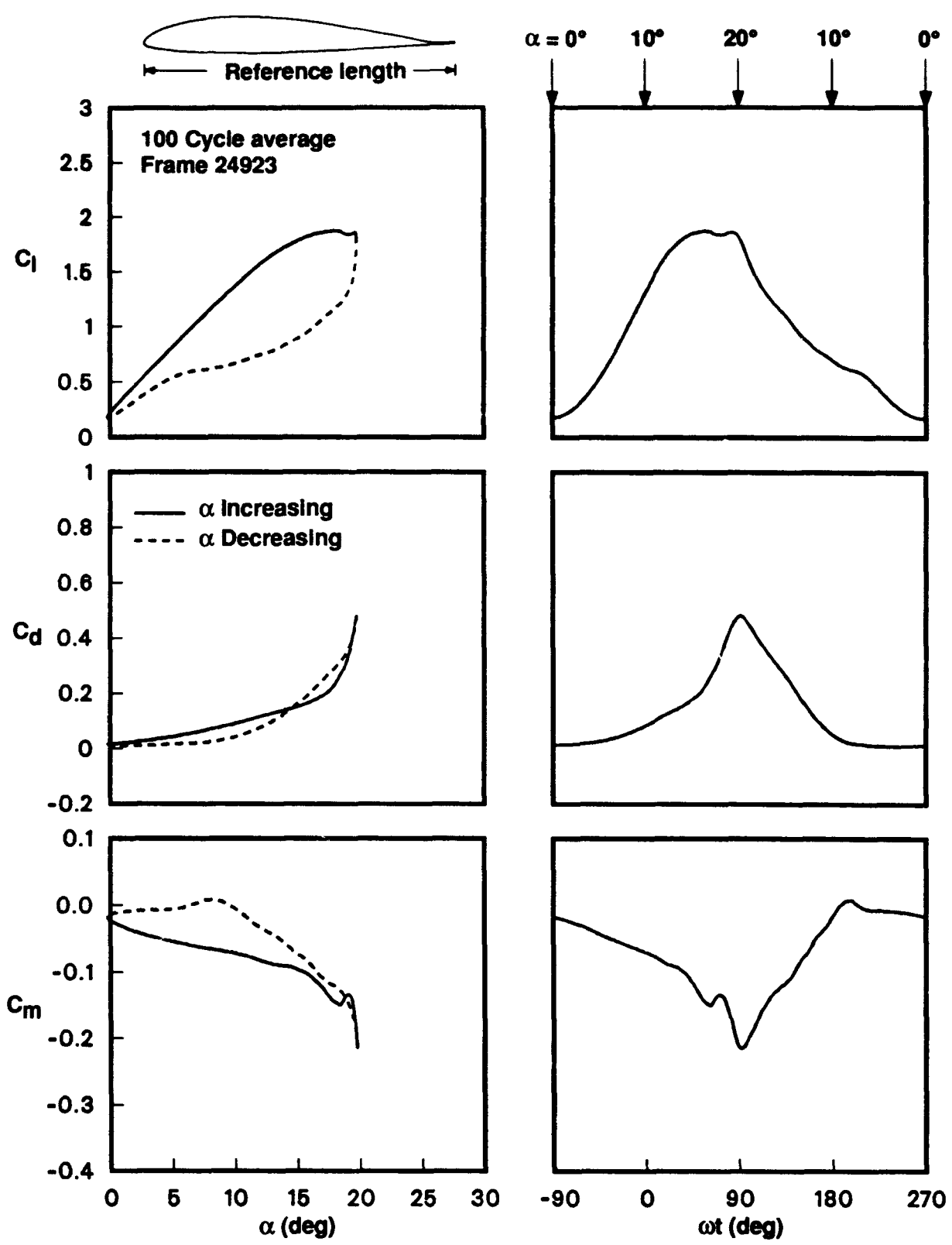
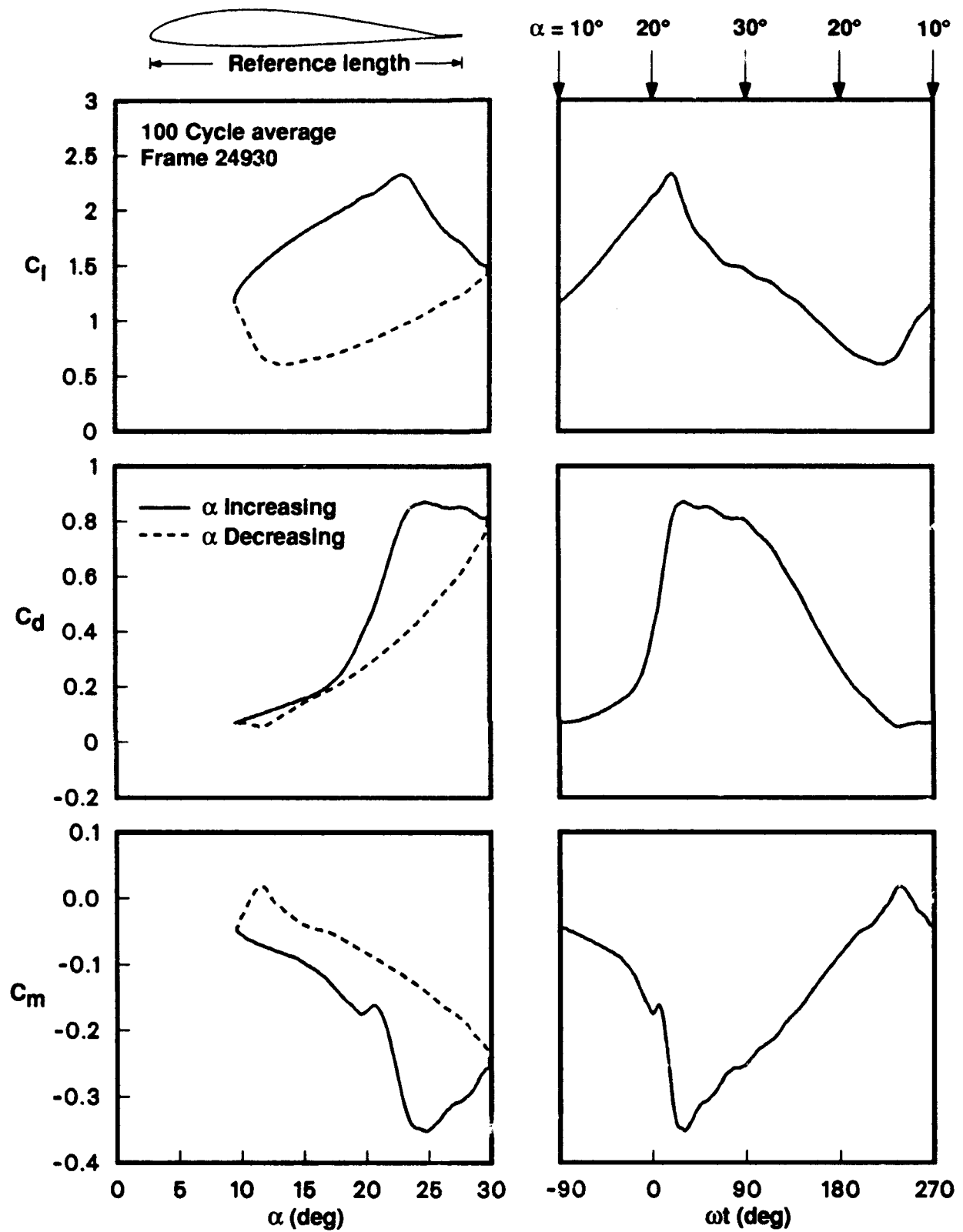


Figure 17. Effect of reduced frequency on the beginning of moment stall for the basic VR-7 airfoil at  $Re = 200K$  with  $\alpha = 15^\circ + 10^\circ \sin(\omega t)$ .



(a)  $\alpha = 10^\circ + 10^\circ \sin(\omega t)$ .

Figure 18. Effects of the mean angle of oscillation on the basic VR-7 airfoil at  $Re = 200K$  and  $k = 0.1$ .



(b)  $\alpha = 20^\circ + 10^\circ \sin(\omega t)$ .

Figure 18. Concluded.

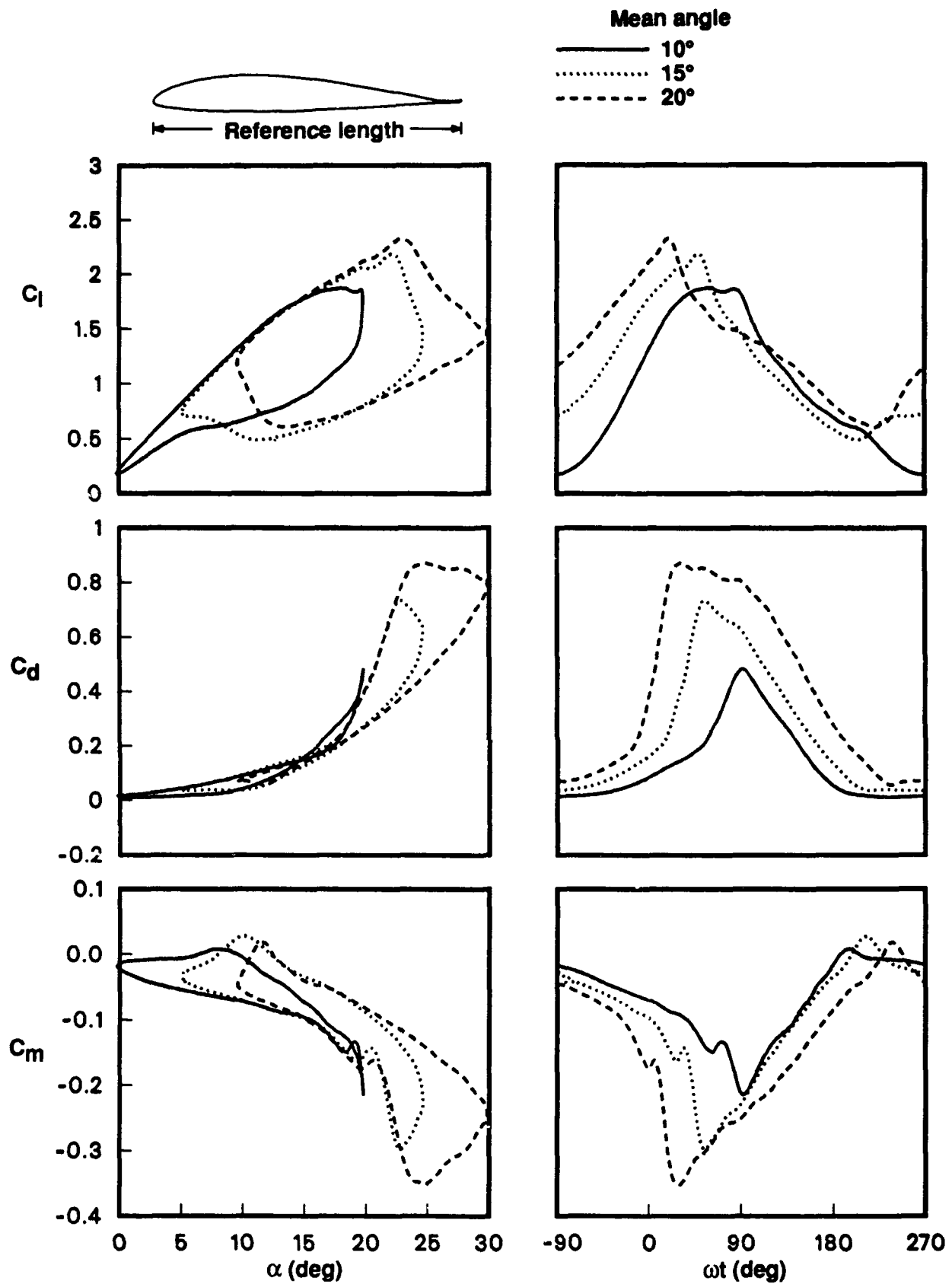


Figure 19. Superposition of results for mean angles of oscillation of  $10^\circ \rightarrow 20^\circ$  for the basic VR-7 airfoil at  $Re = 200K$  and  $k = 0.1$ .

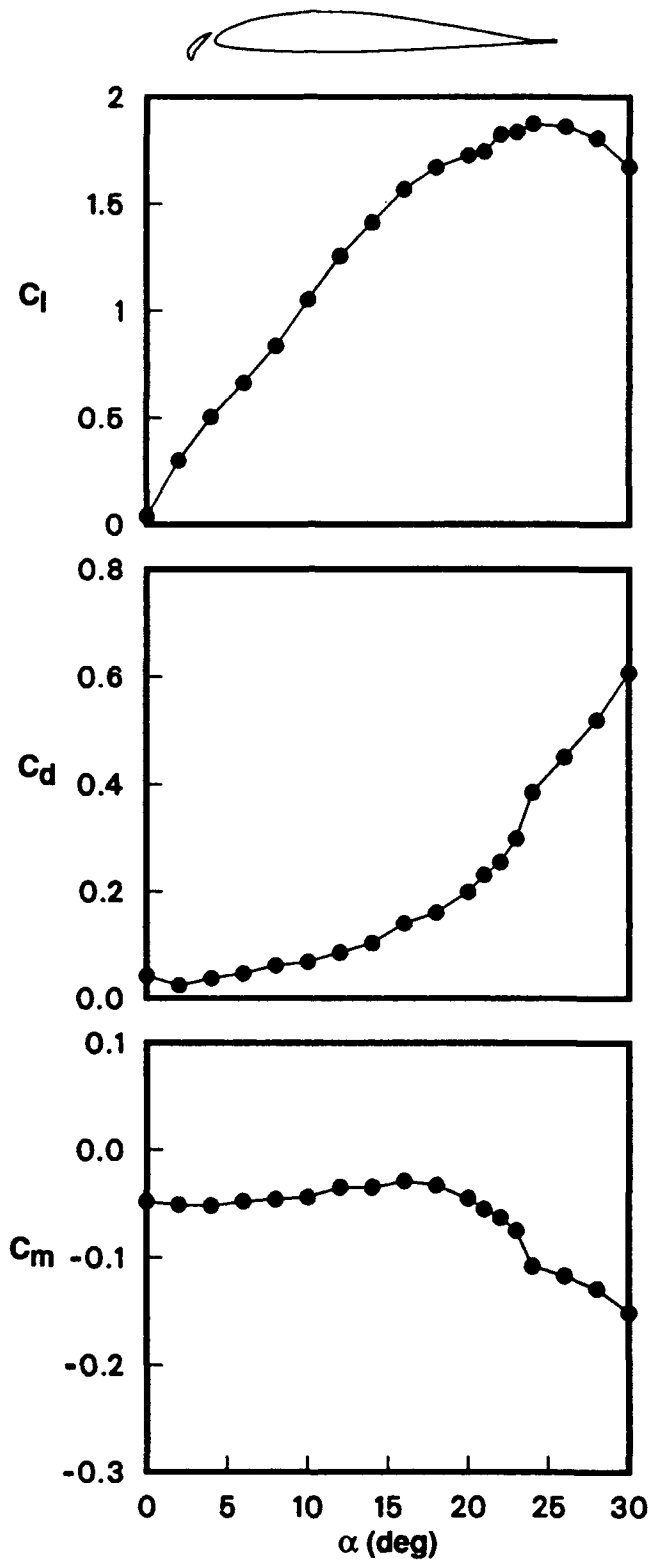


Figure 20. Steady data for the VR-7 airfoil with slat at  $Re = 0.2 \times 10^6$ .

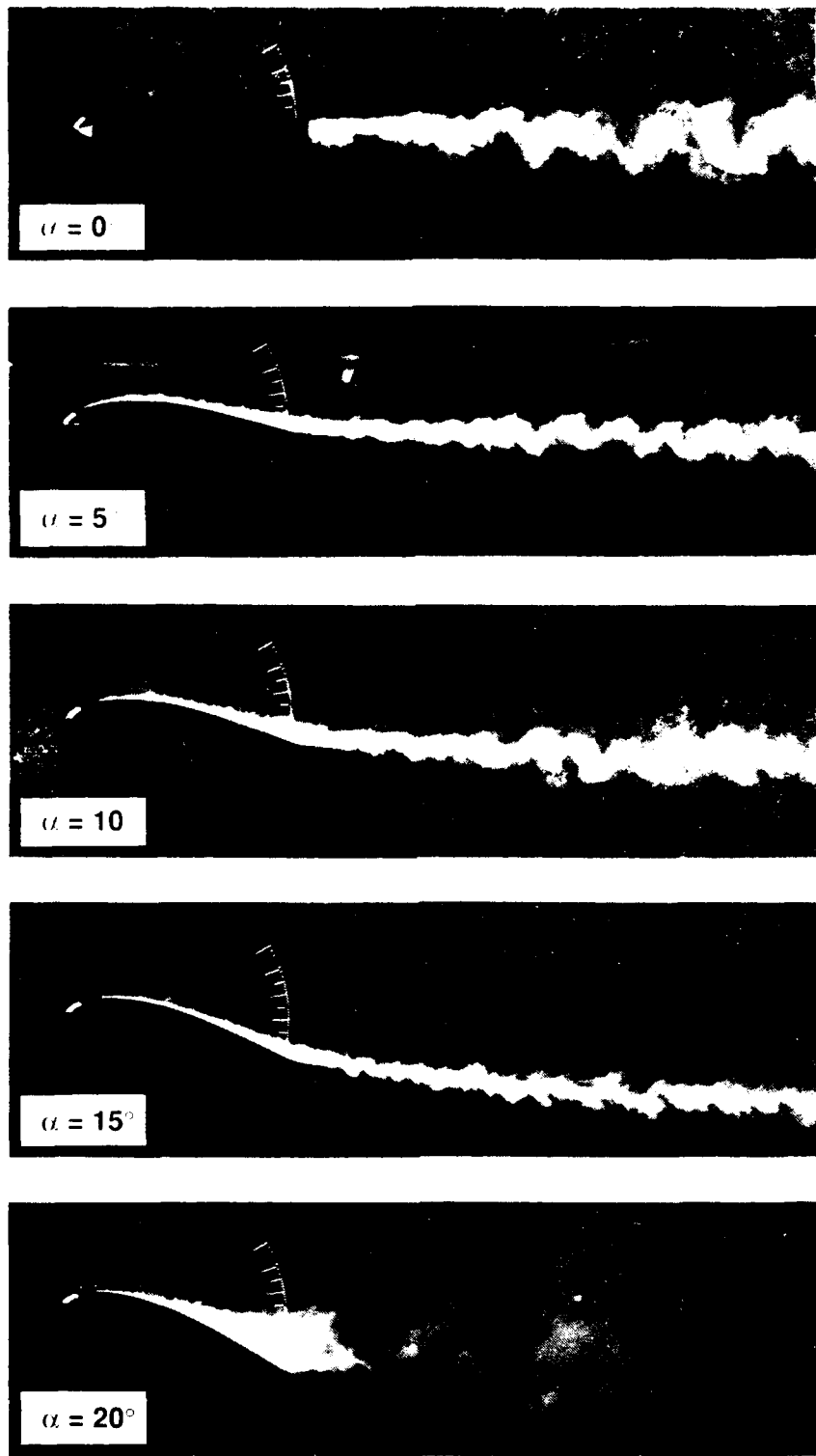
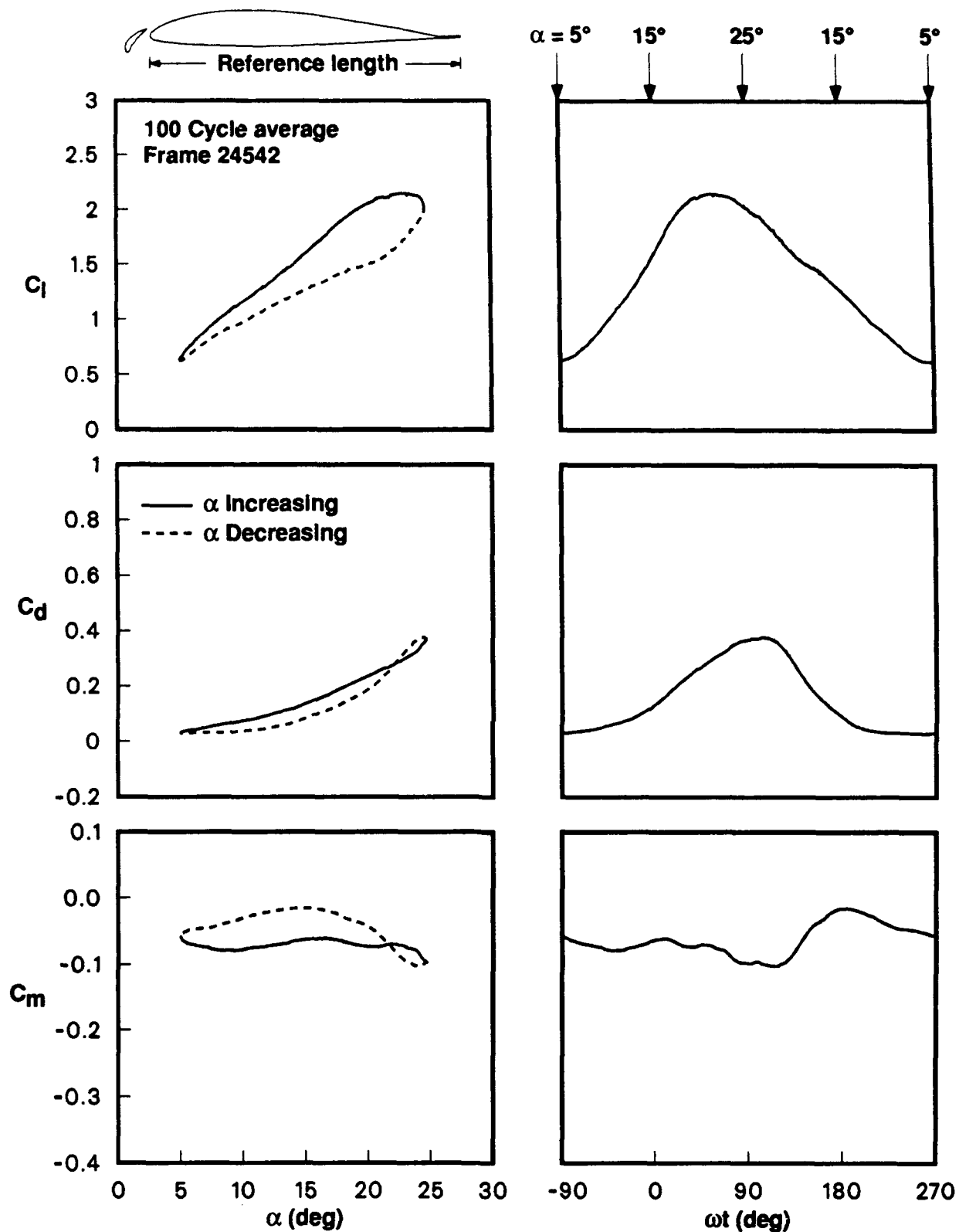
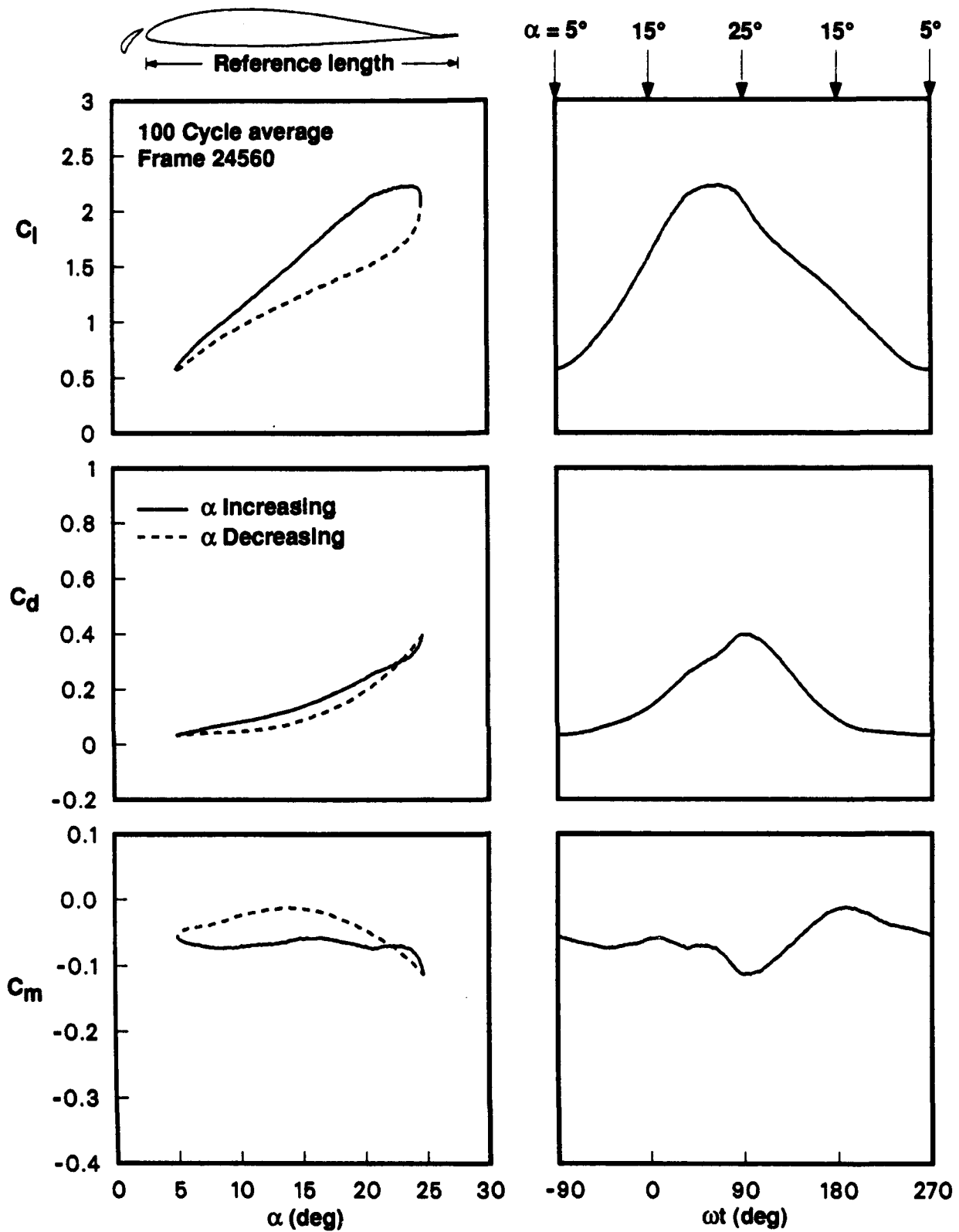


Figure 21. Boundary layer and wake visualization for the VR-7 airfoil with slat at  $Re = 0.2 \times 10^6$  with fixed angles of attack.



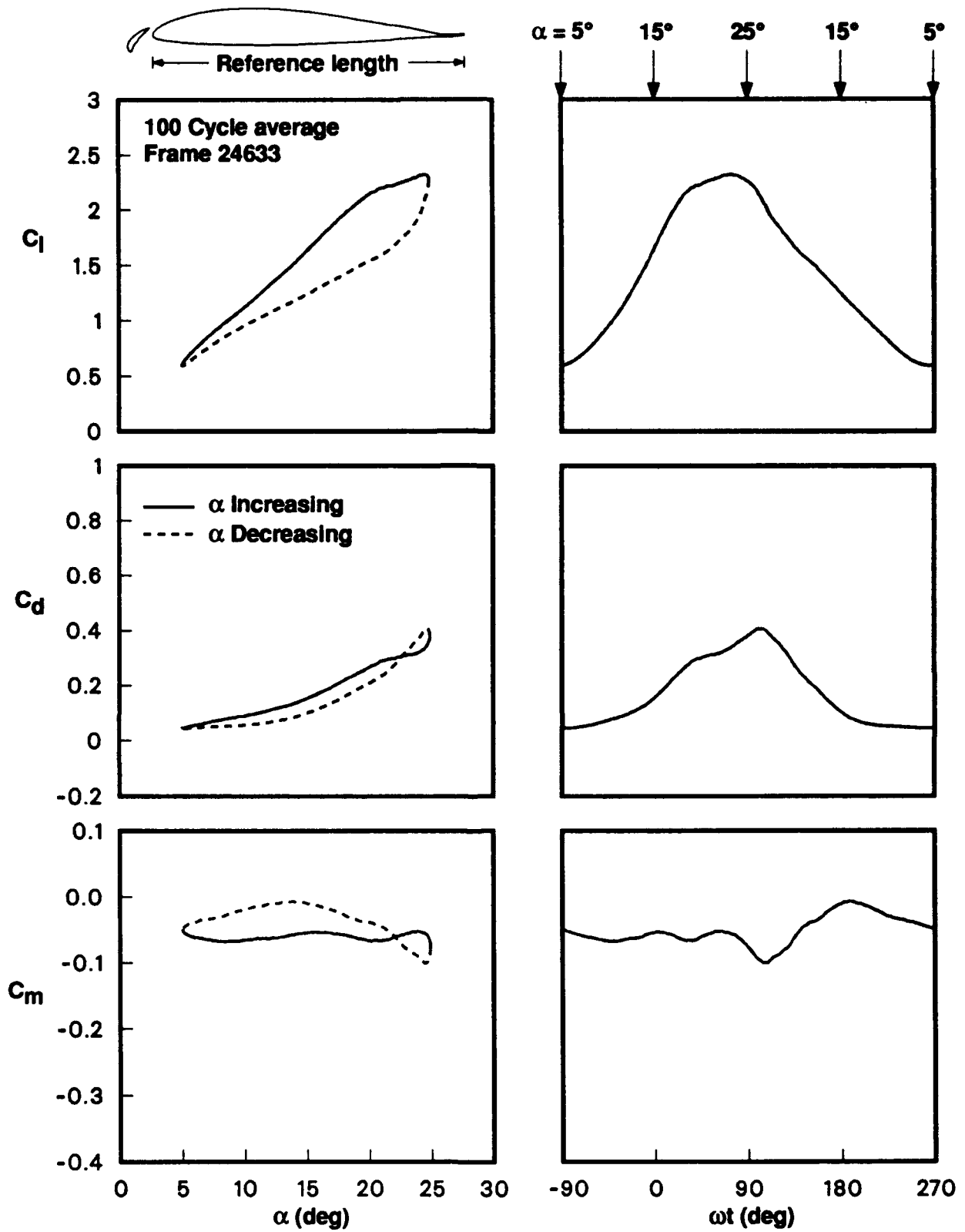
(a)  $Re = 100K$ .

Figure 22. Reynolds number effects on the VR-7 airfoil with slat at  $k = 0.10$  with  $\alpha = 15^\circ + 10^\circ \sin(\omega t)$ .



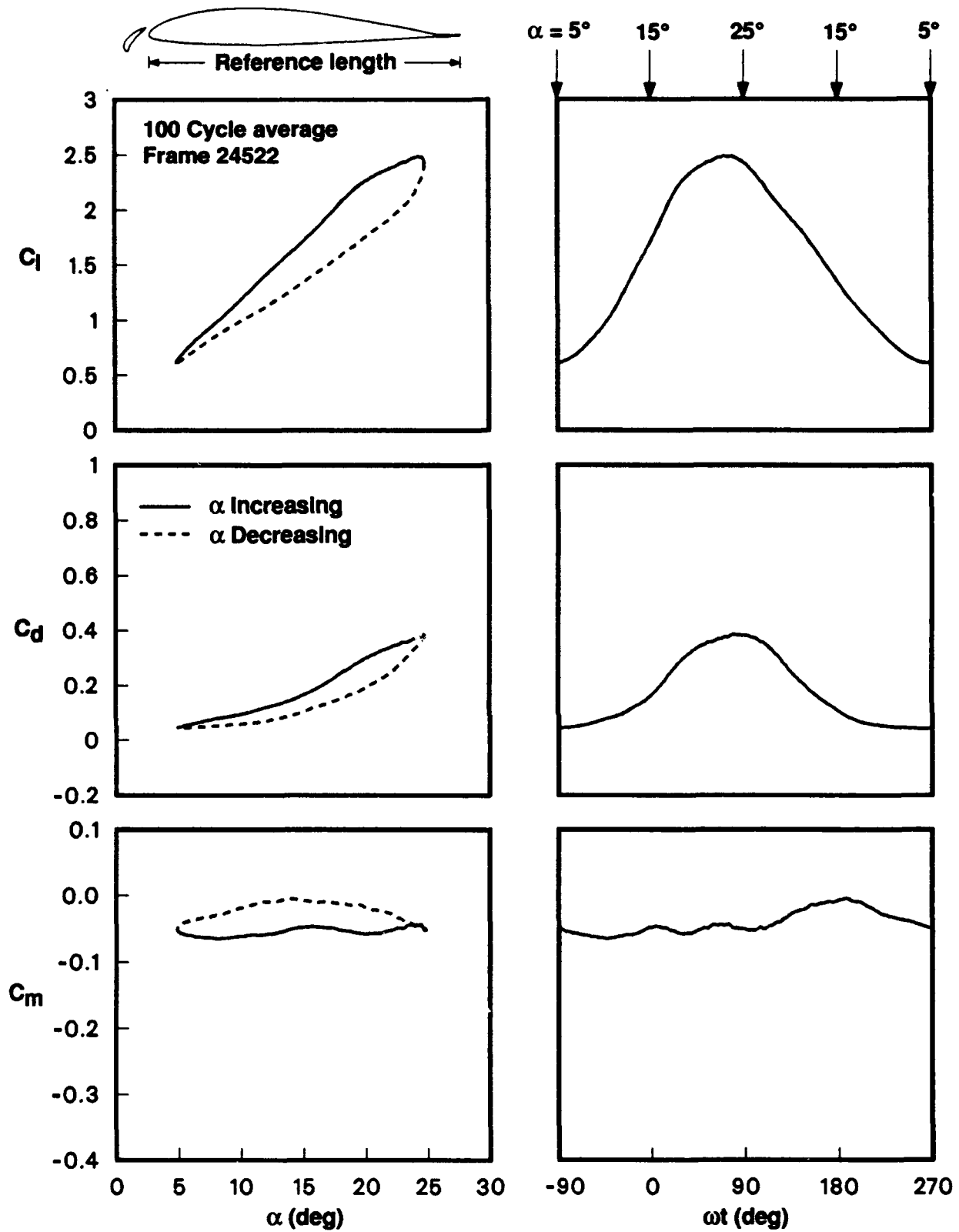
(b)  $Re = 150K$ .

Figure 22. Continued.



(c)  $Re = 200K$ .

Figure 22. Continued.



(d)  $Re = 250K$ .

Figure 22. Concluded.

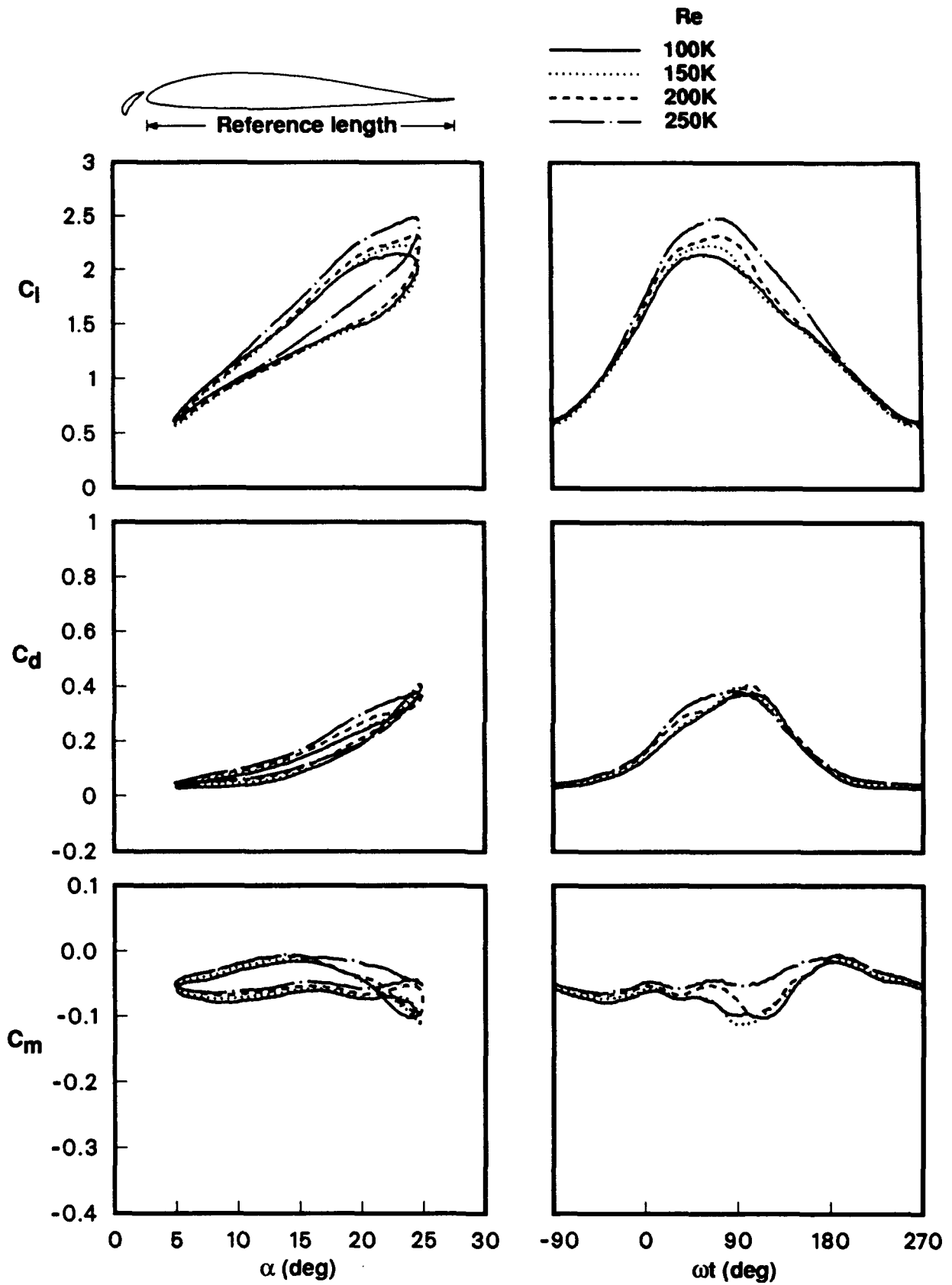
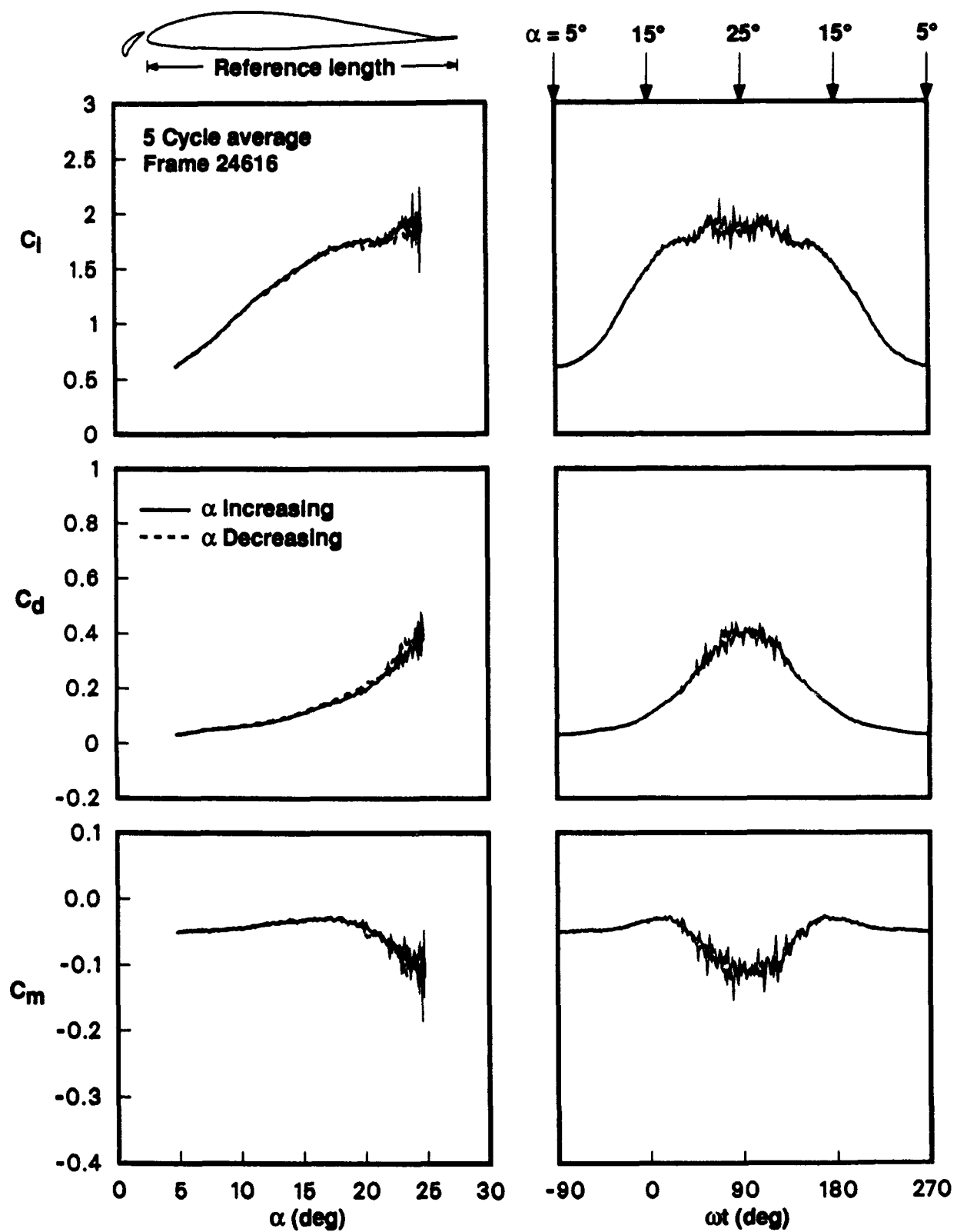
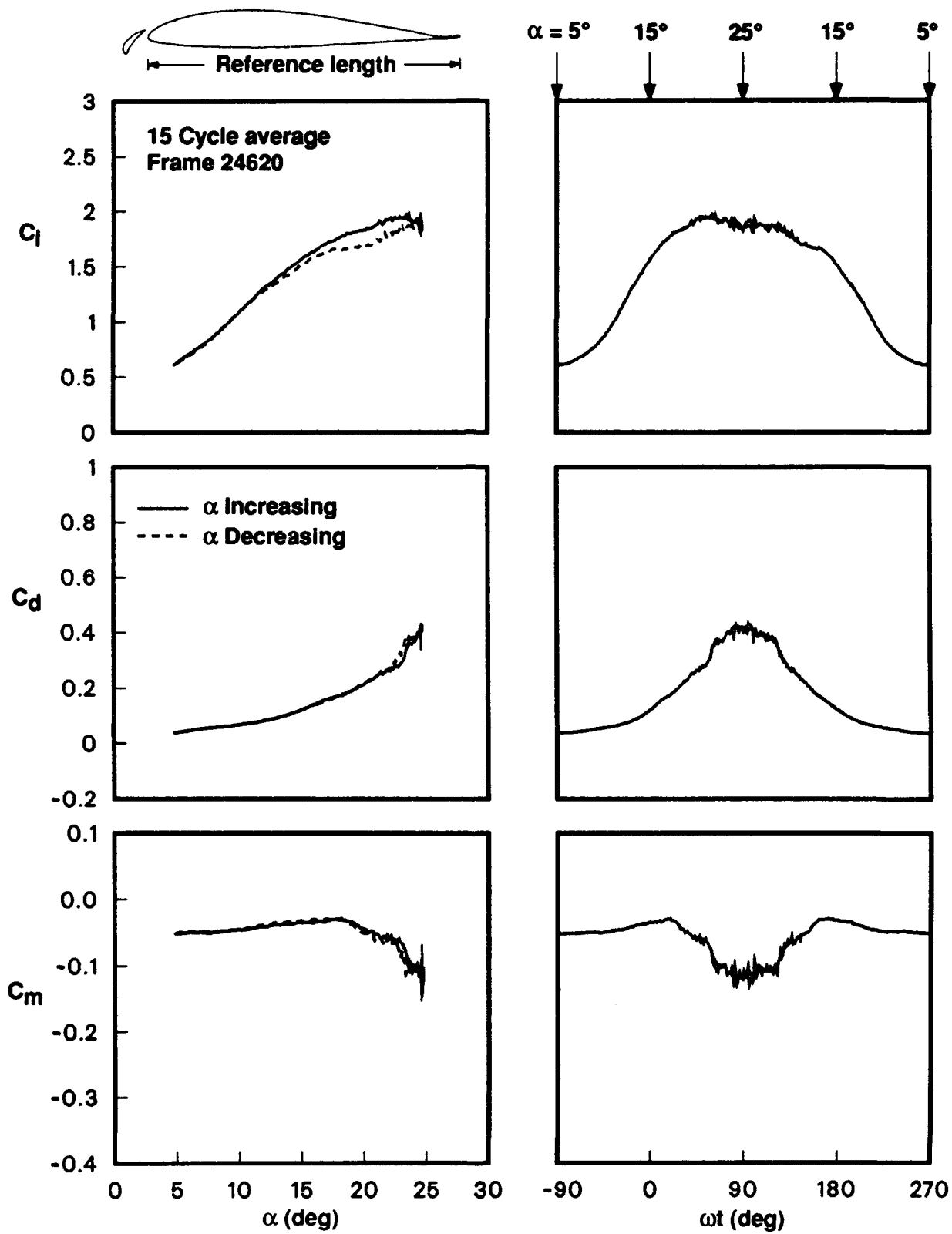


Figure 23. Superposition of results for  $Re = 100K \rightarrow 250K$  for the VR-7 airfoil with slat at  $k = 0.10$  with  $\alpha = 15^\circ + 10^\circ \sin(\omega t)$ .



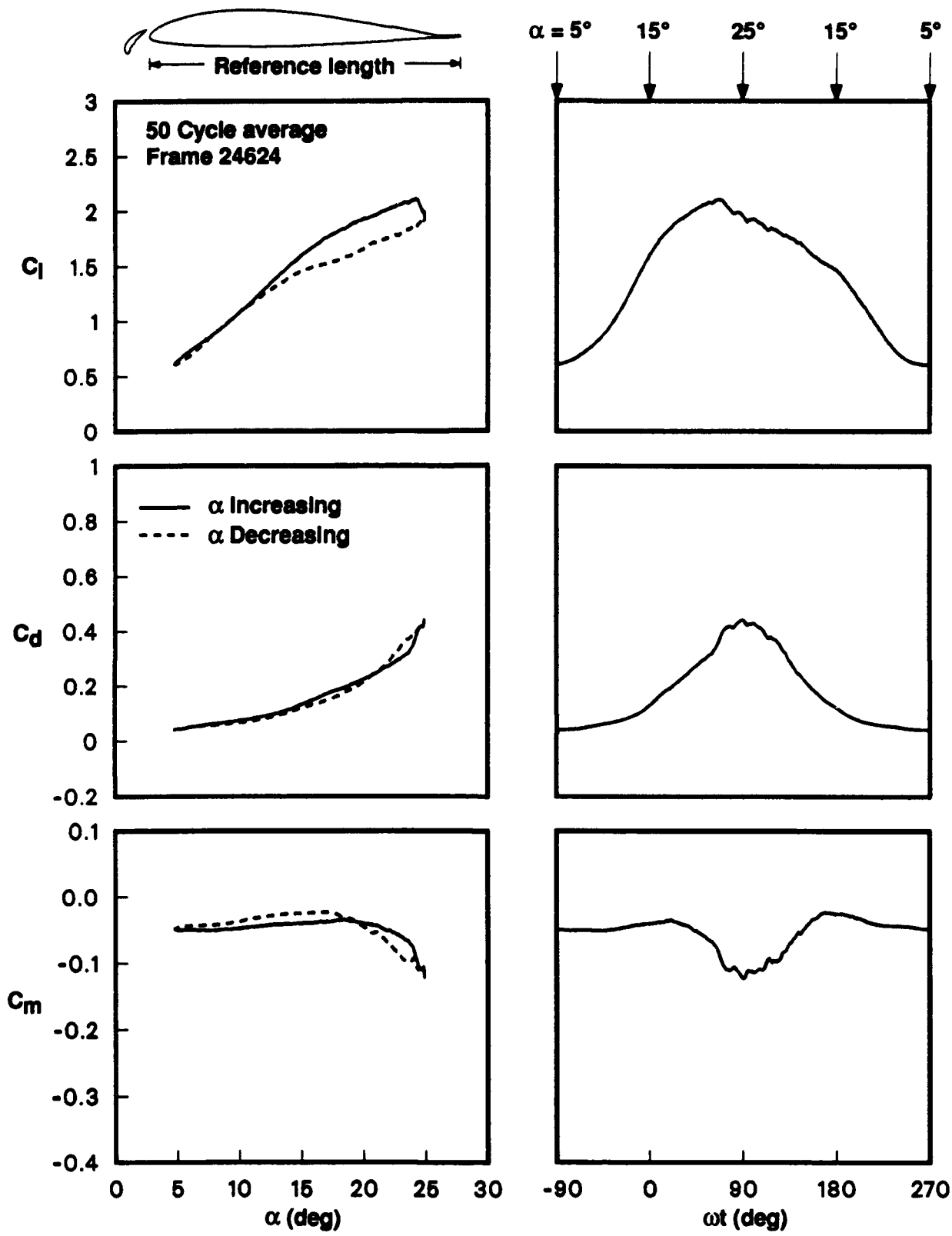
(a)  $k = 0.001$ .

Figure 24. Reduced frequency effects on the VR-7 airfoil with slat at  $Re = 200K$  with  $\alpha = 15^\circ + 10^\circ \sin(\omega t)$ .



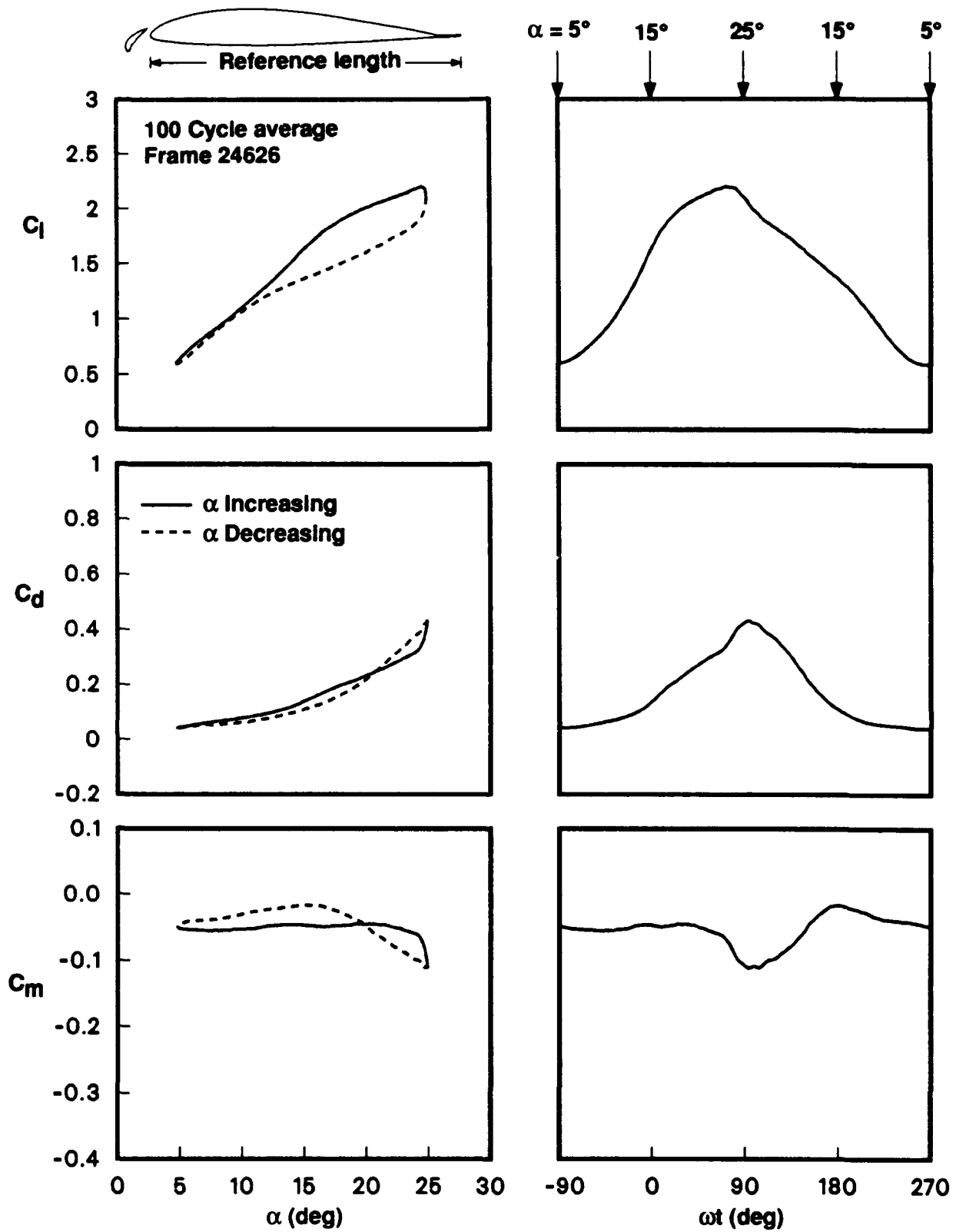
(b)  $k = 0.005$ .

Figure 24. Continued.



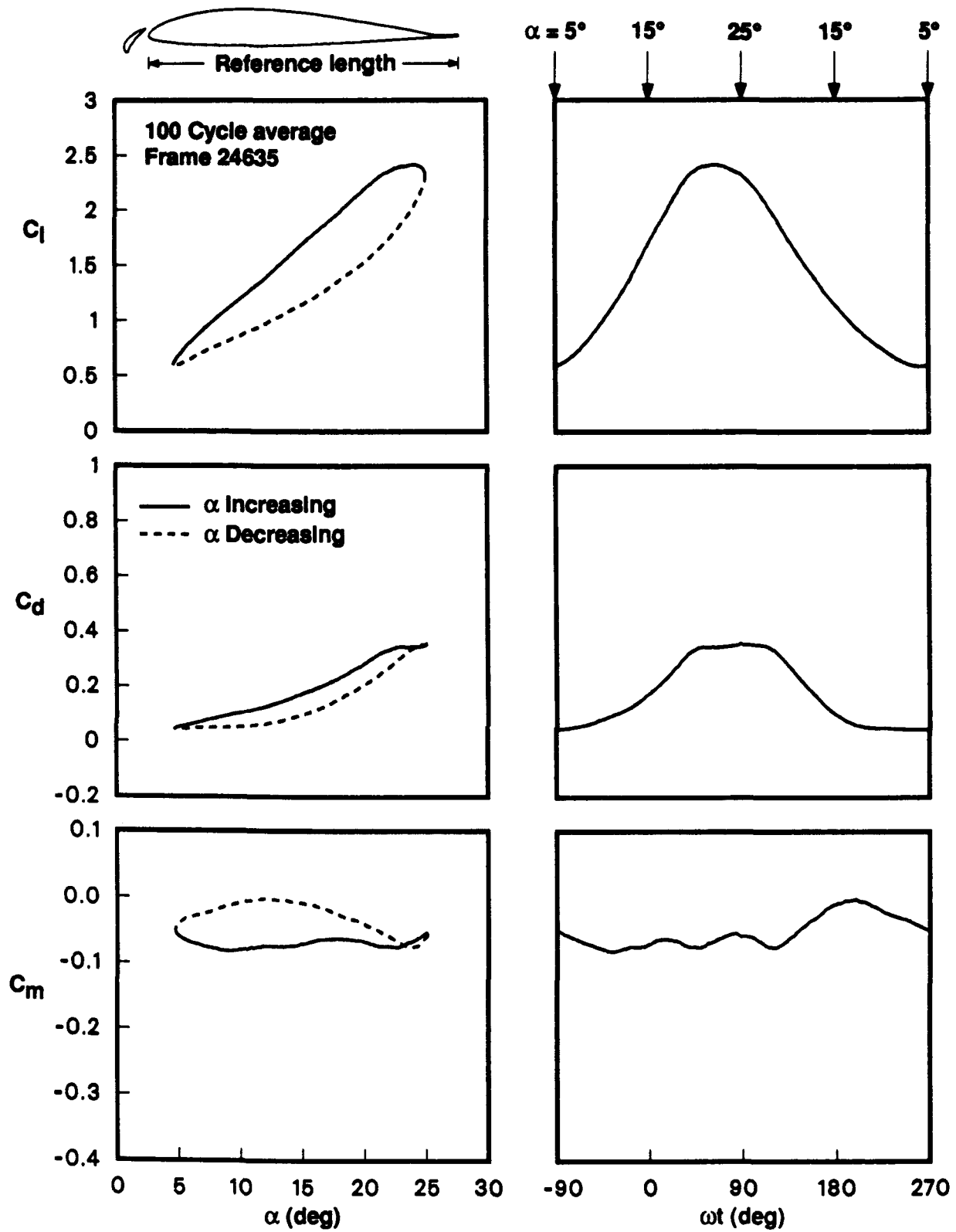
(c)  $k = 0.025$ .

Figure 24. Continued.



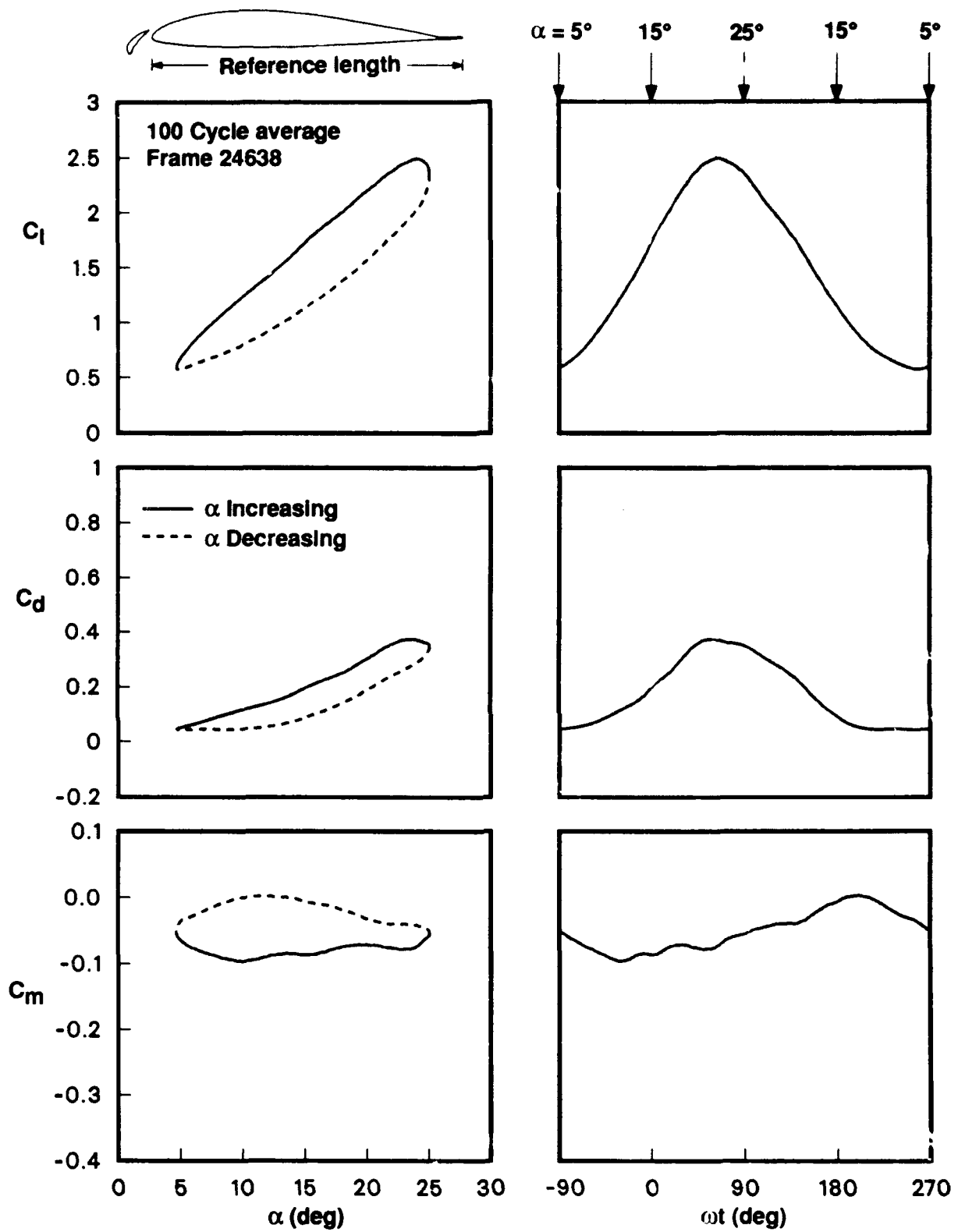
(d)  $k = 0.05$ .

Figure 24. Continued.



(e)  $k = 0.15$ .

Figure 24. Continued.



(f)  $k = 0.20$ .

Figure 24. Concluded.

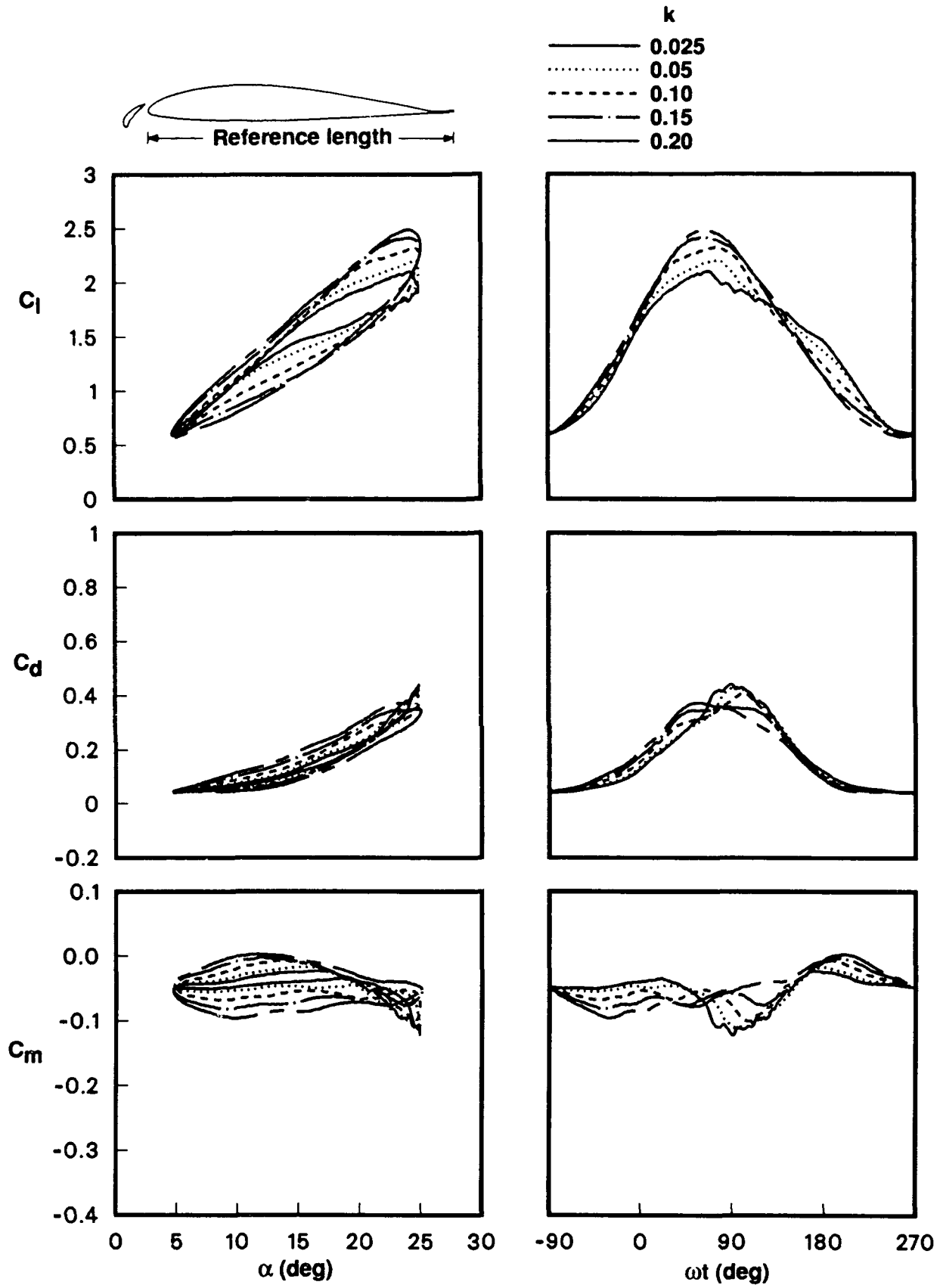
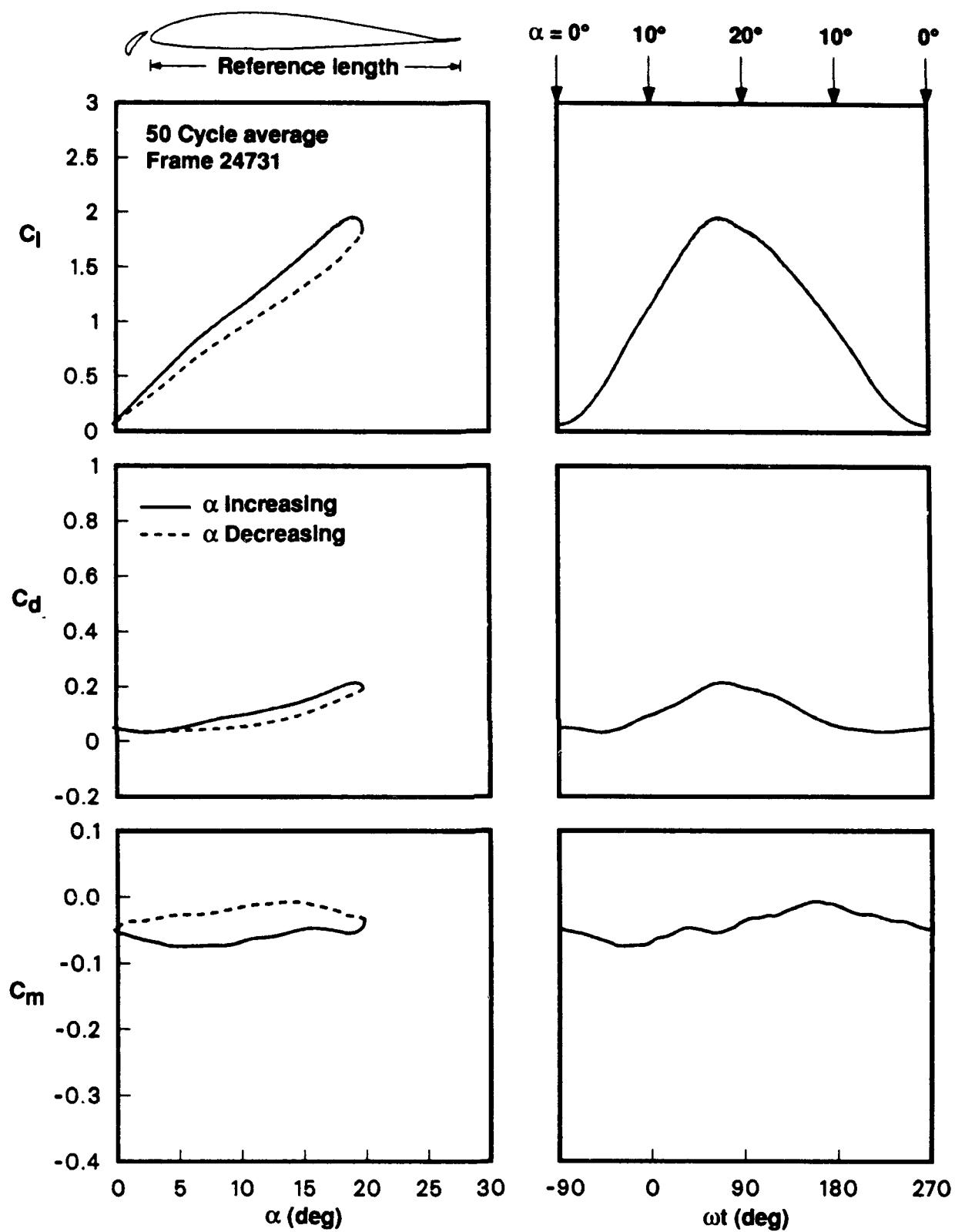
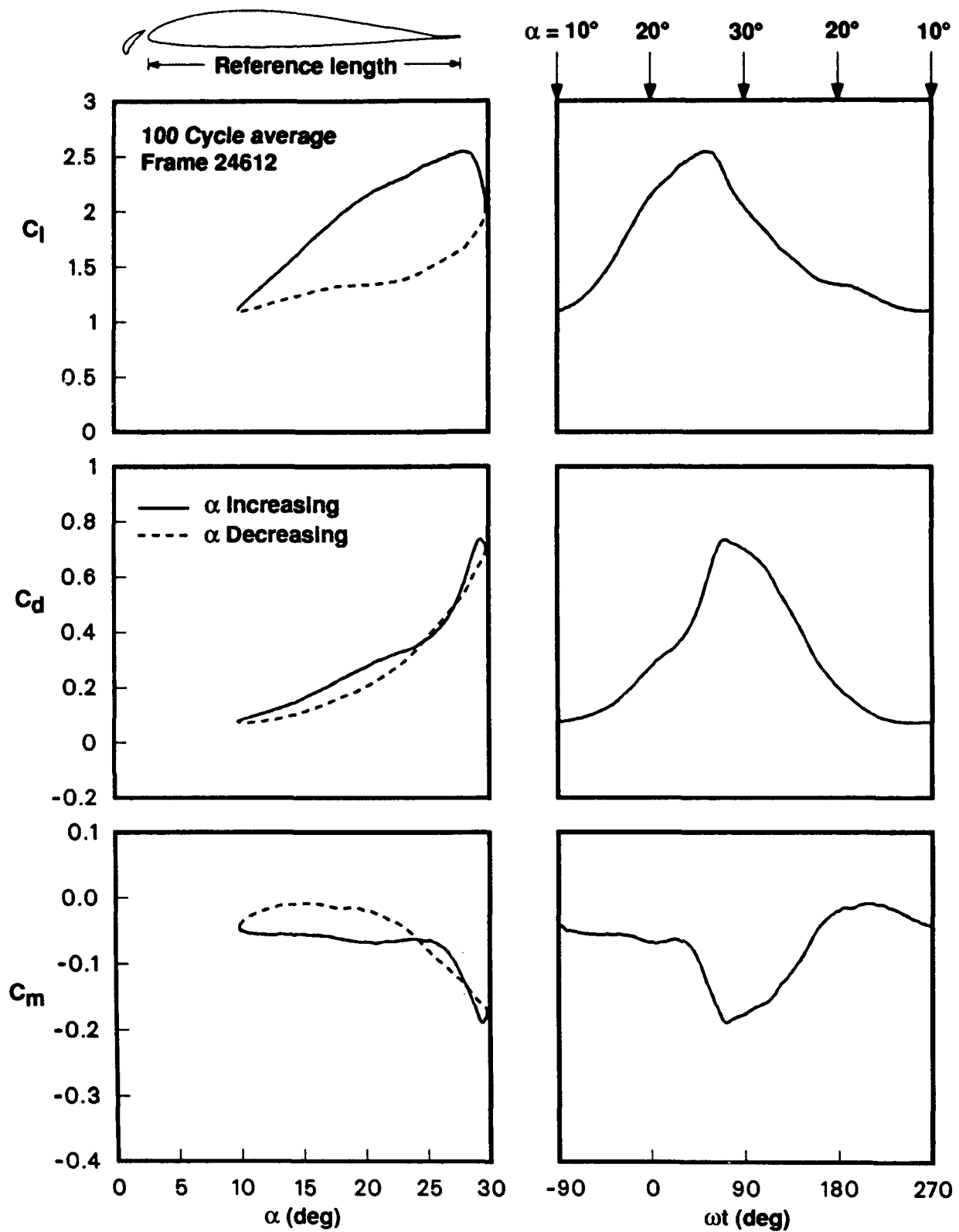


Figure 25. Superposition of results for  $k = 0.025 \rightarrow 0.20$  for the VR-7 airfoil with slat at  $Re = 200K$  with  $\alpha = 15^\circ + 10^\circ \sin(\omega t)$ .



(a)  $\alpha = 10^\circ + 10^\circ \sin(\omega t)$ .

Figure 26. Effects of mean angle of oscillation on the VR-7 airfoil with slat at  $Re = 200K$  and  $k = 0.1$ .



(b)  $\alpha = 20^\circ + 10^\circ \sin(\omega t)$ .

Figure 26. Concluded.

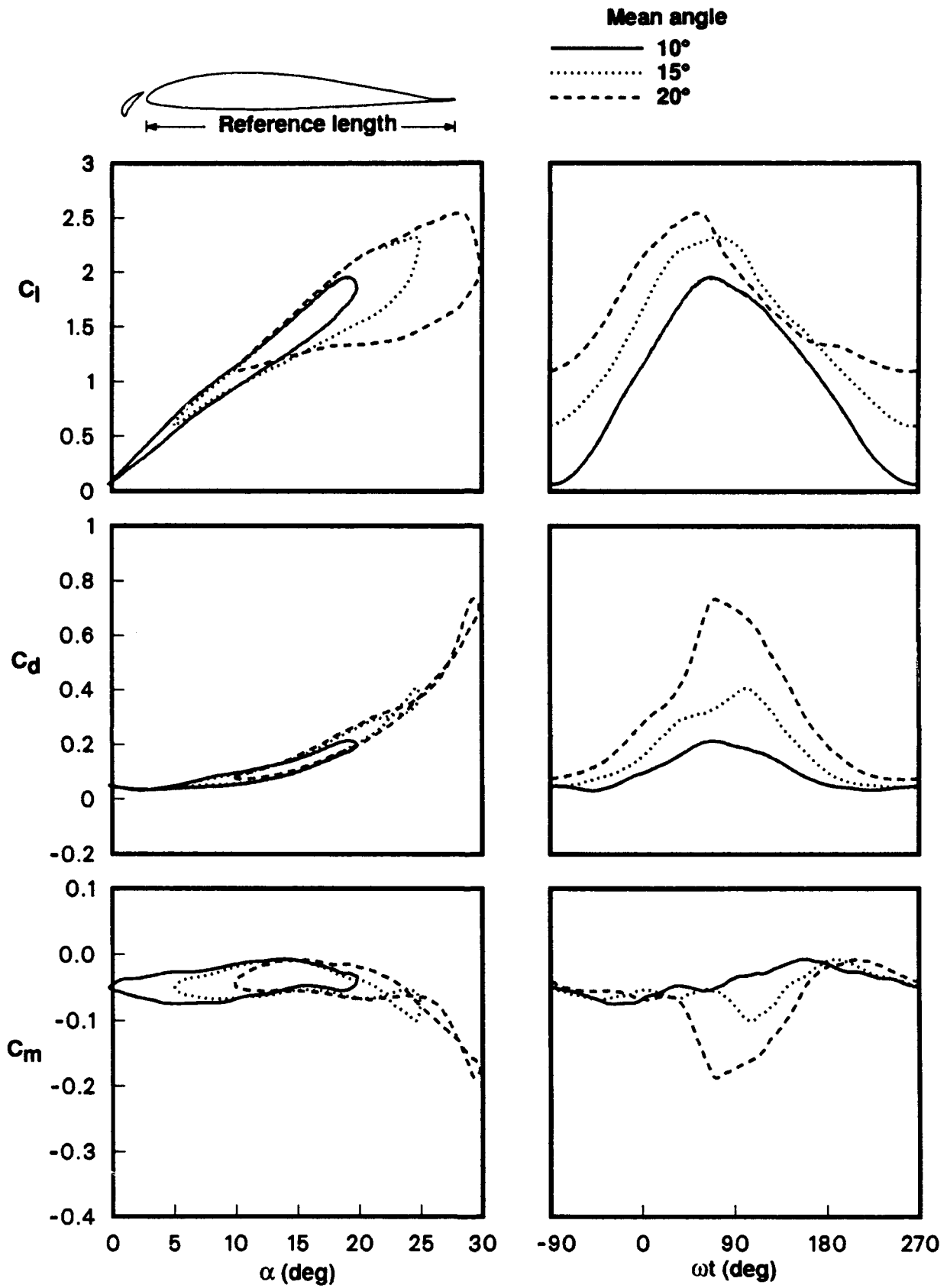
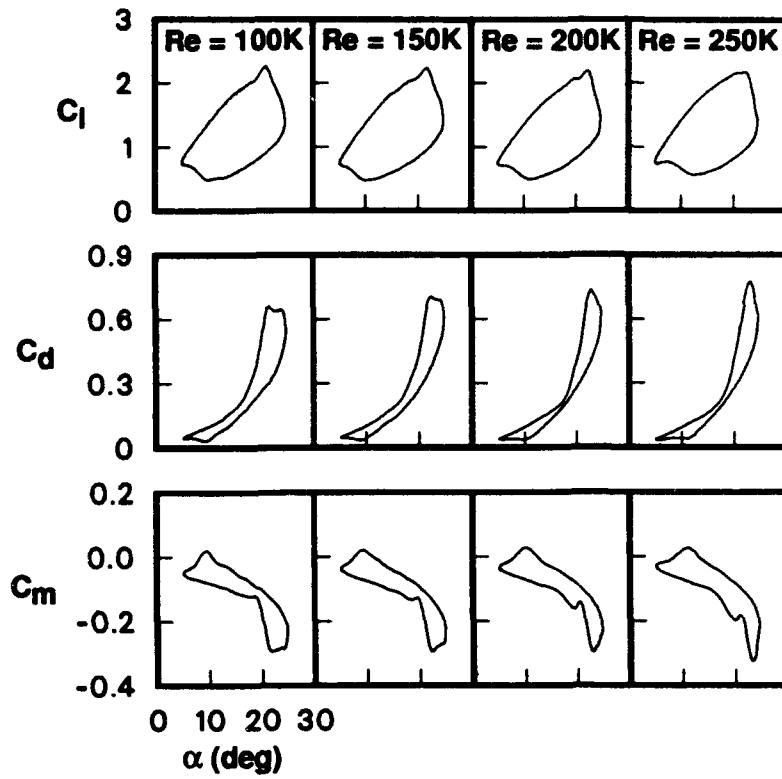
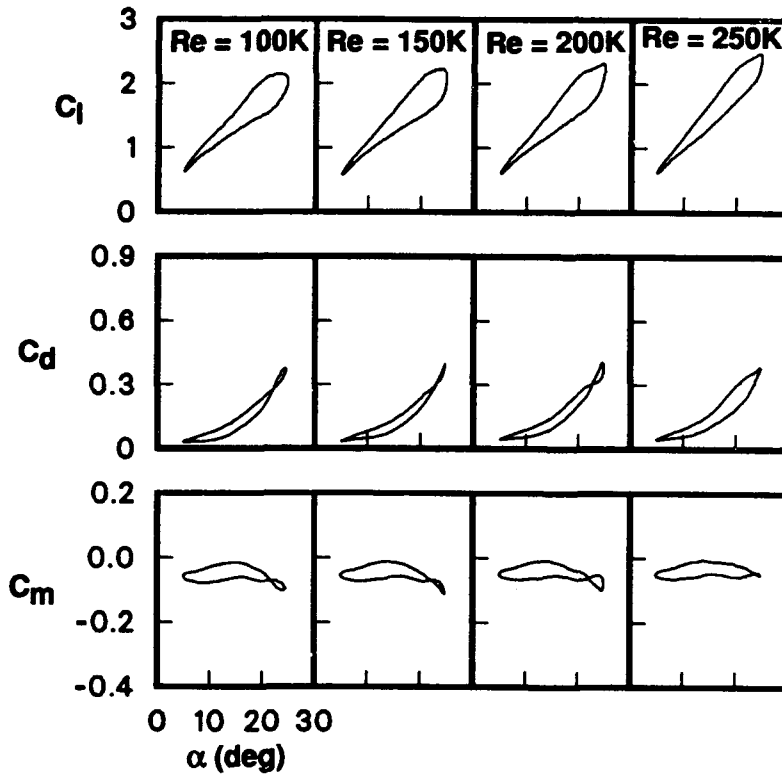


Figure 27. Superposition of results for mean angles of oscillation of  $10^\circ \rightarrow 20^\circ$  for the VR-7 airfoil with slat at  $Re = 200K$  and  $k = 0.1$ .

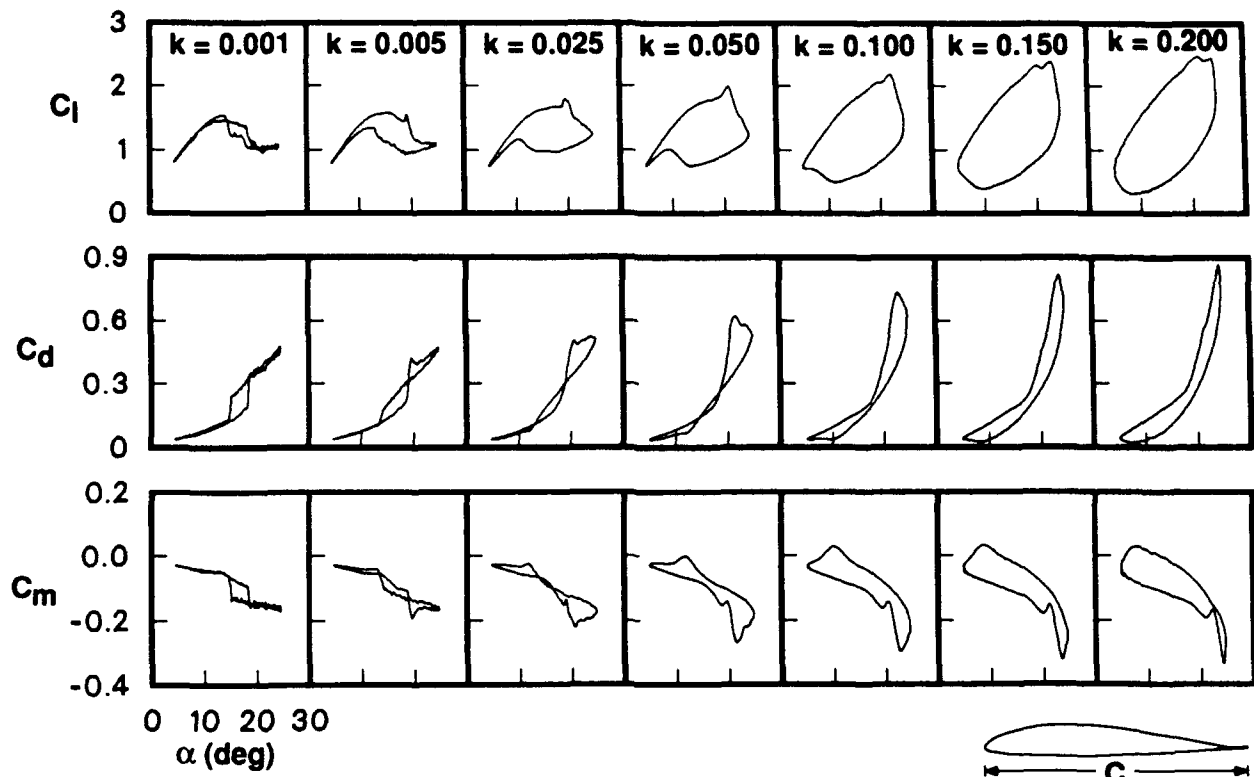


(a) Basic VR-7 airfoil.

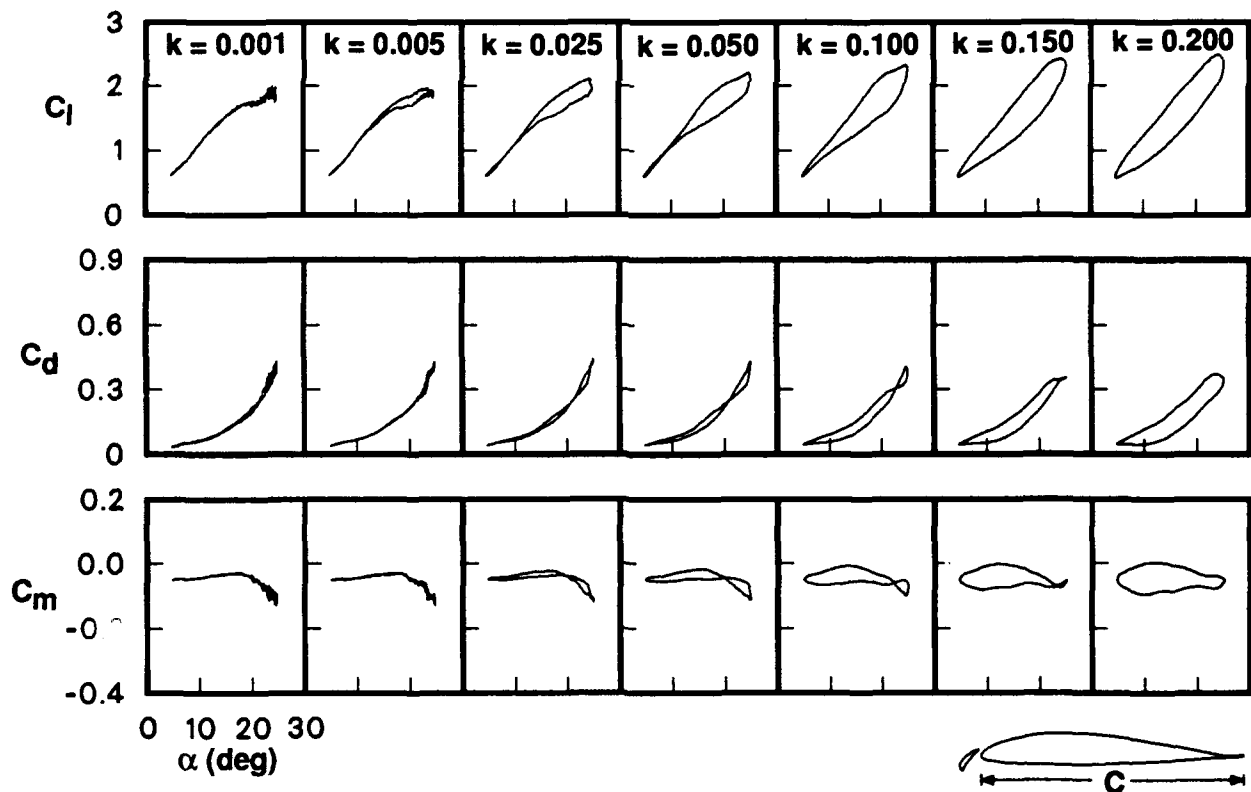


(b) VR-7 airfoil with slat.

Figure 28. Summary of results for  $Re = 100K \rightarrow 250K$  at  $k = 0.1$  with  $\alpha = 15^\circ + 10^\circ \sin(\omega t)$ .

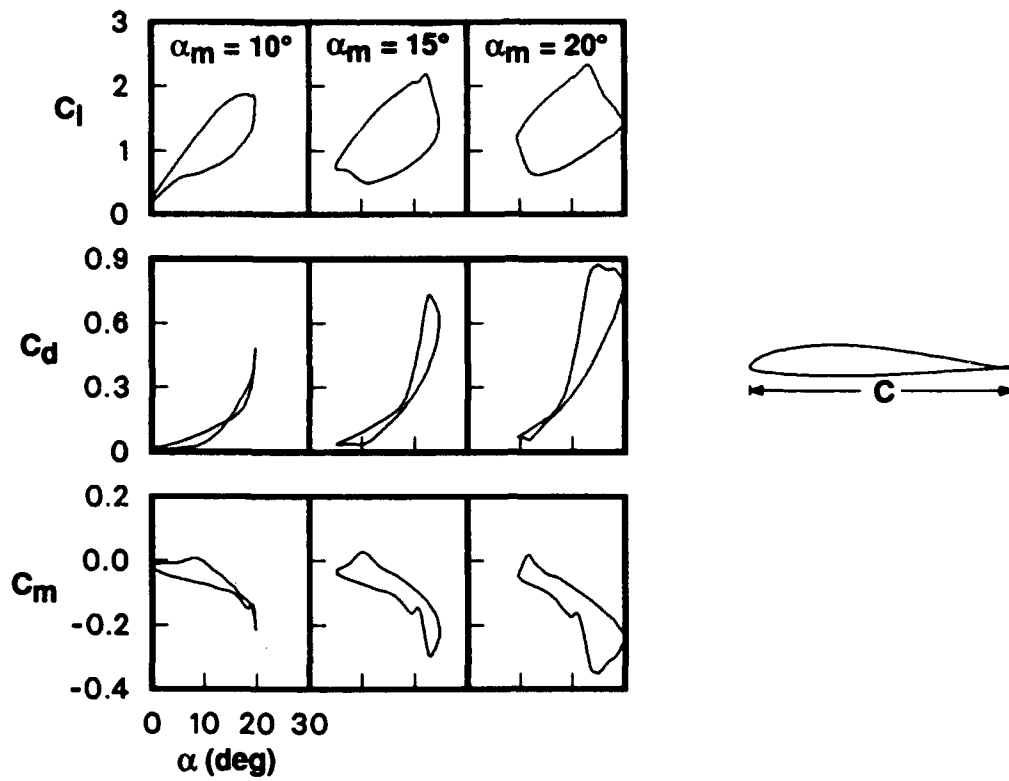


(a) Basic VR-7 airfoil.

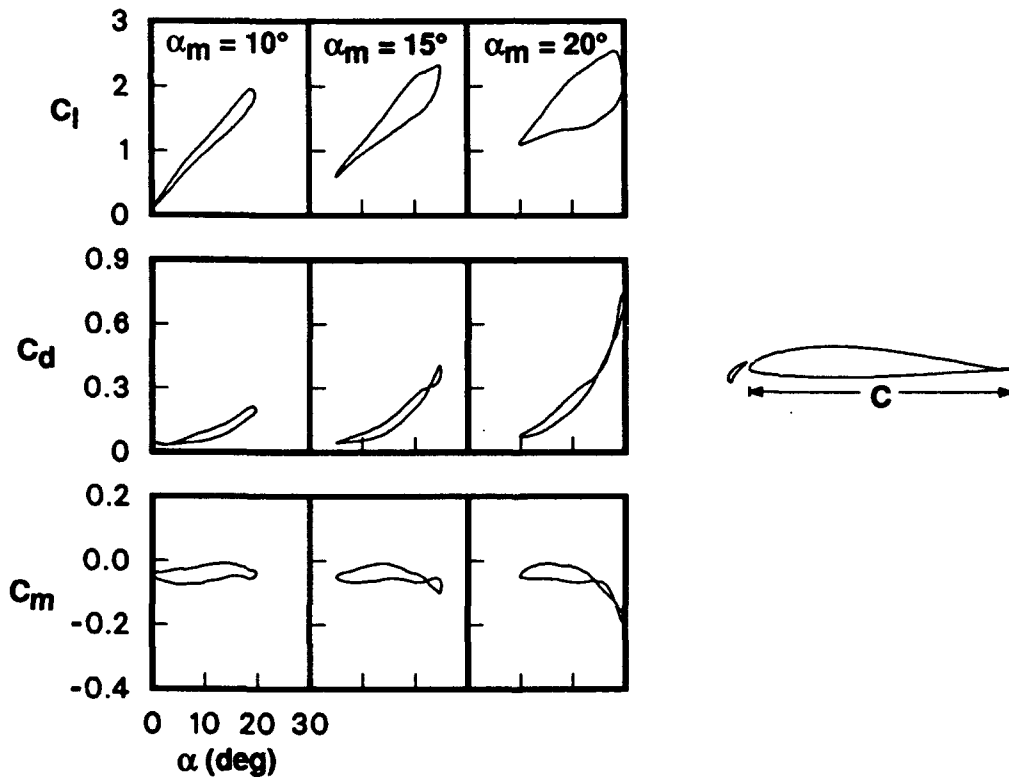


(b) VR-7 airfoil with slat.

Figure 29. Summary of results for  $k = 0.001 \rightarrow 0.20$  at  $Re = 200K$  with  $\alpha = 15^\circ + 10^\circ \sin(\omega t)$ .

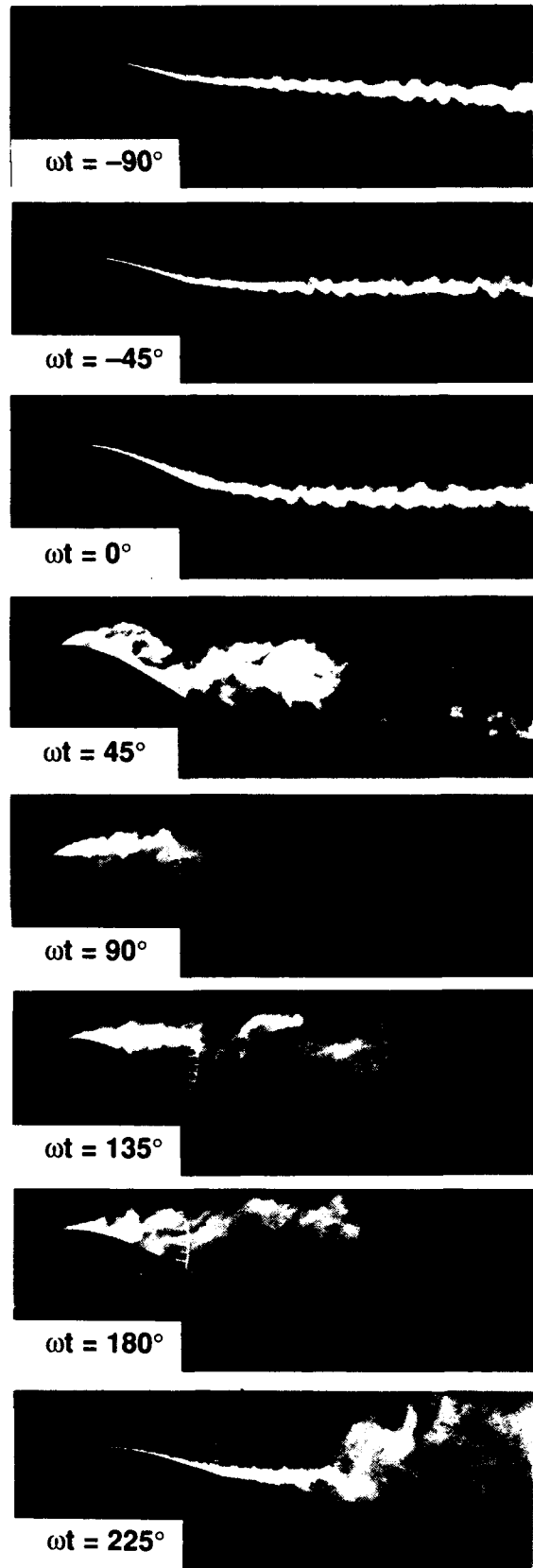
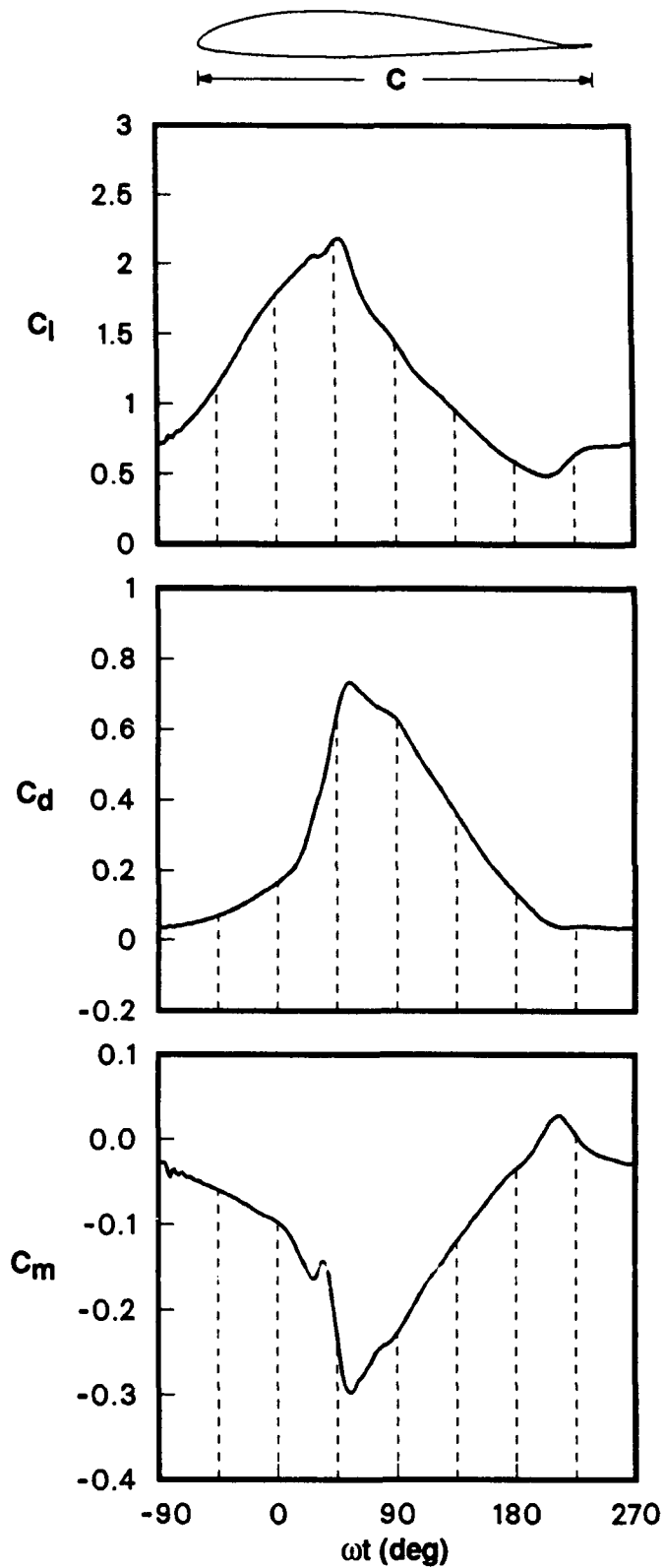


(a) Basic VR-7 airfoil.



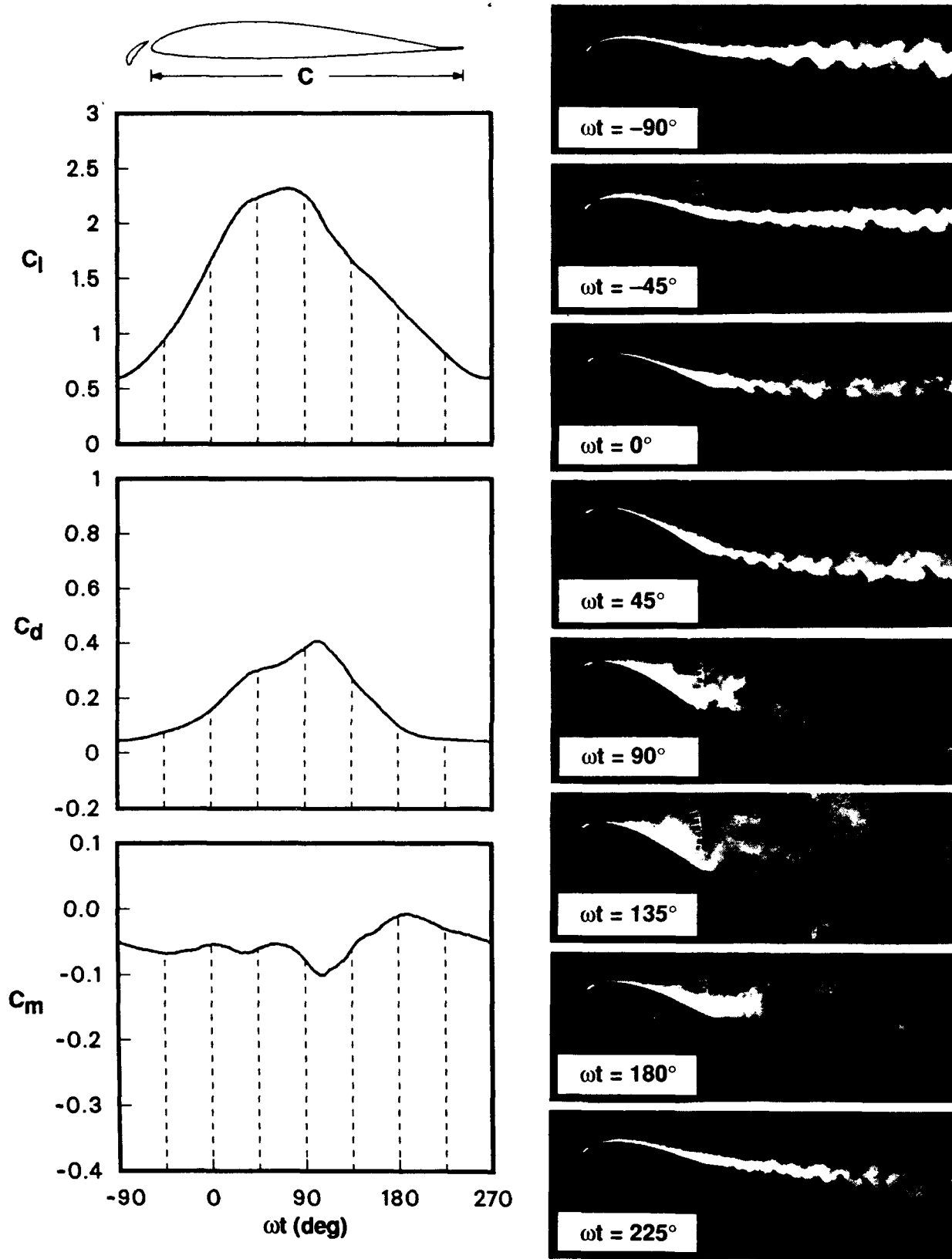
(b) VR-7 airfoil with slat.

Figure 30. Summary of results for mean angles of oscillation of  $10^\circ \rightarrow 20^\circ$  with  $\alpha = \alpha_m + 10^\circ \sin(\omega t)$  at  $Re = 200K$  and  $k = 0.1$ .



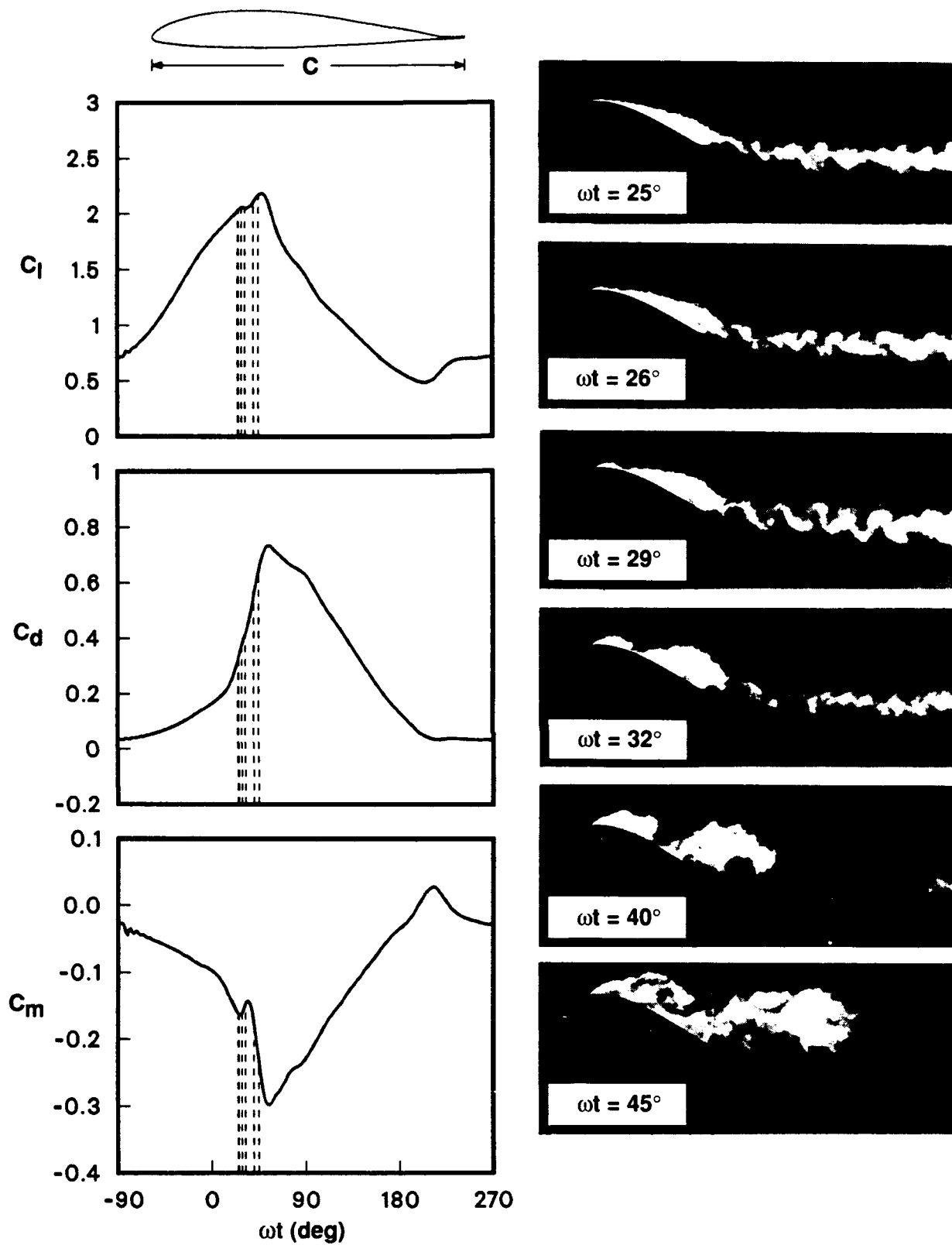
(a) Basic VR-7 airfoil

Figure 31. Visualization of flow over cycle of oscillation at  $Re = 200K$  and  $k = 0.1$  with  $\alpha = 15^\circ + 10^\circ \sin(\omega t)$ .



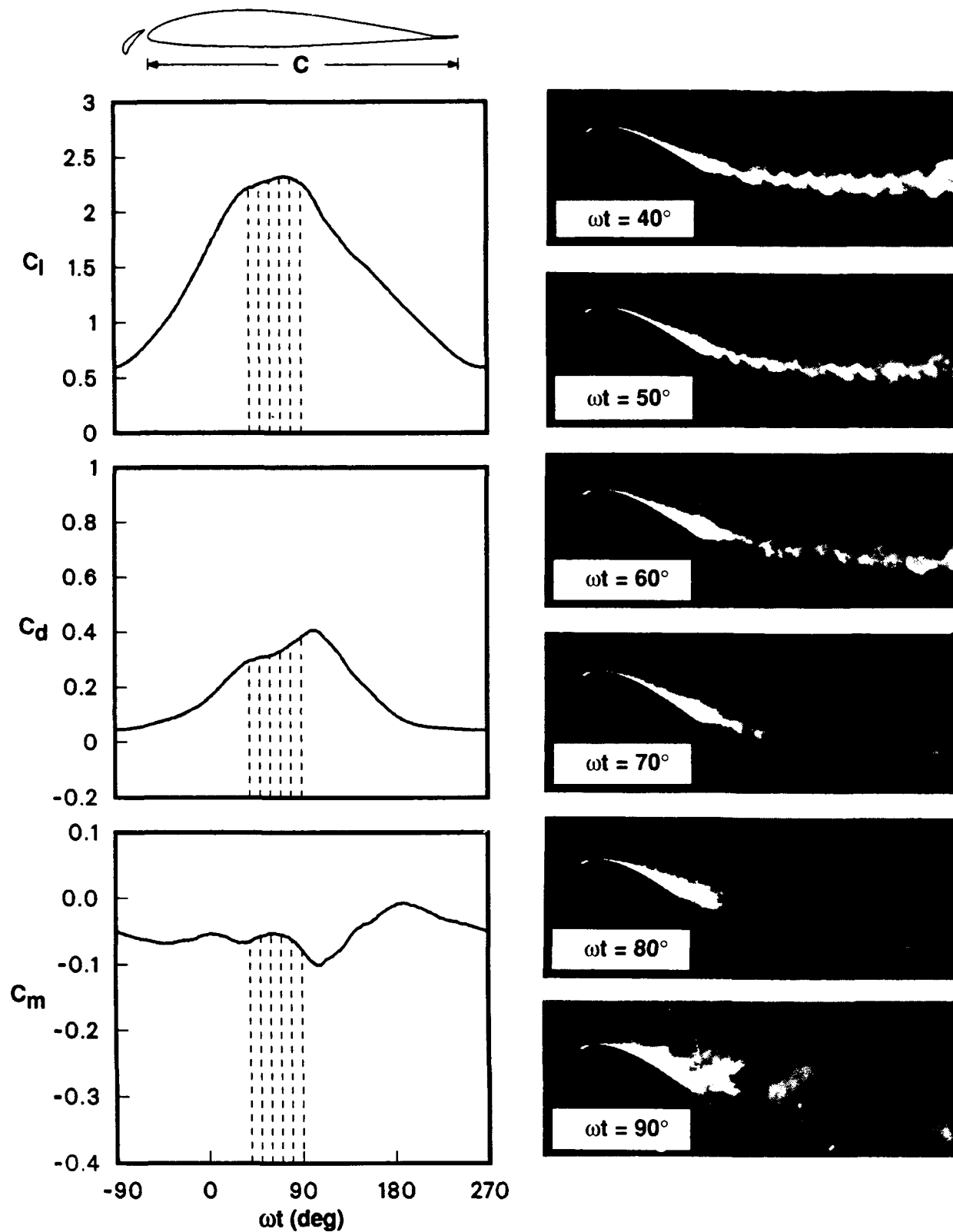
(b) VR-7 airfoil with slat.

Figure 31. Concluded.



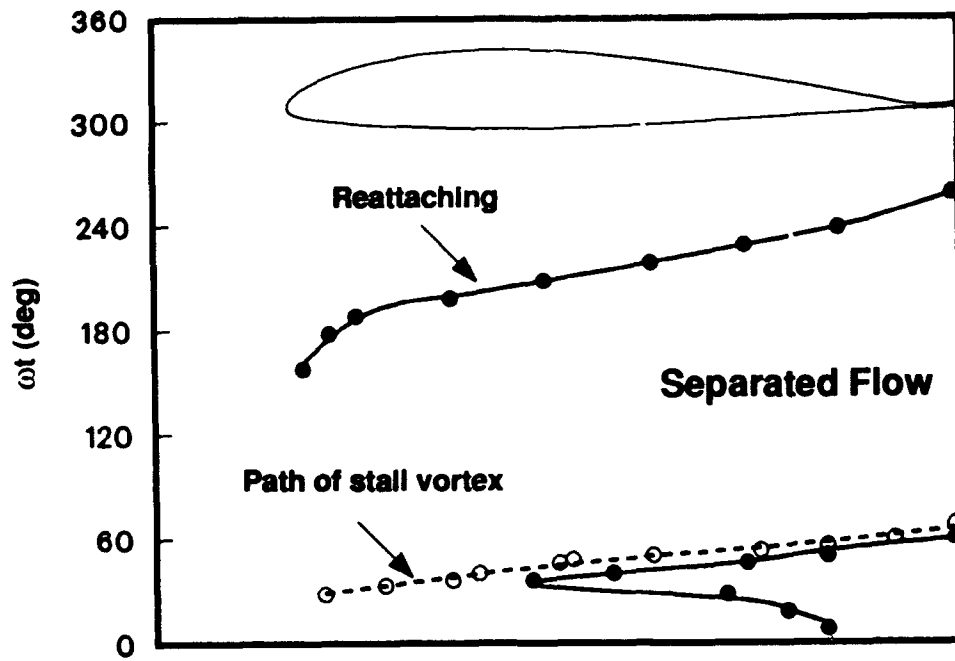
(a) Basic VR-7 airfoil.

Figure 32. Visualization of flow during initial stages of flow separation at  $Re = 200K$  and  $k = 0.1$  with  $\alpha = 15^\circ + 10^\circ \sin(\omega t)$ .

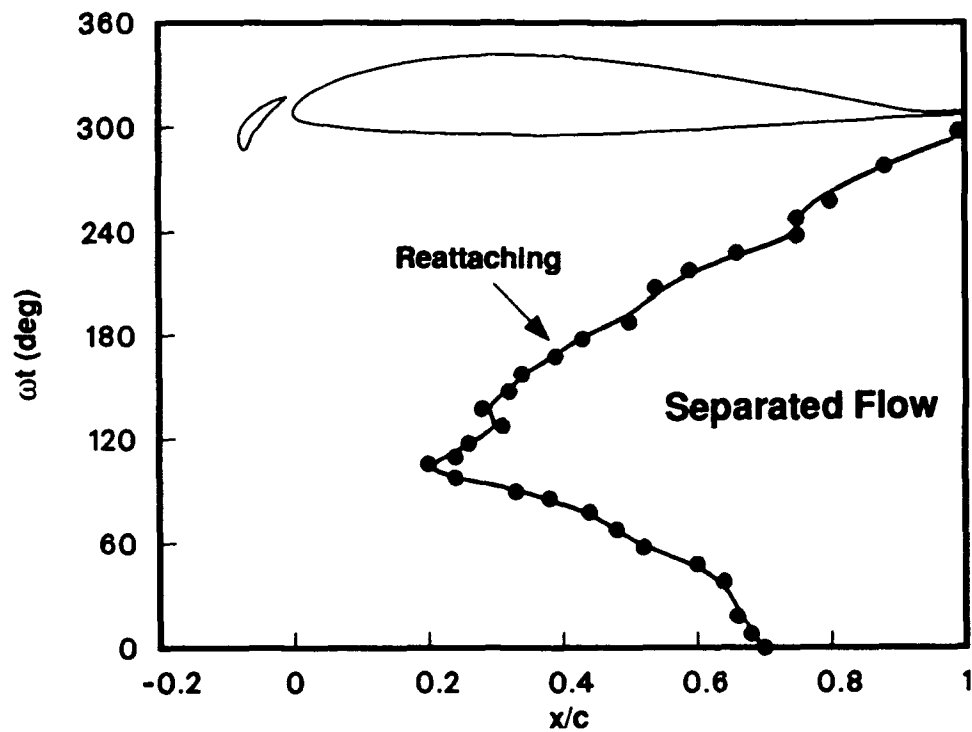


(b) VR-7 airfoil with slat.

Figure 32. Concluded.

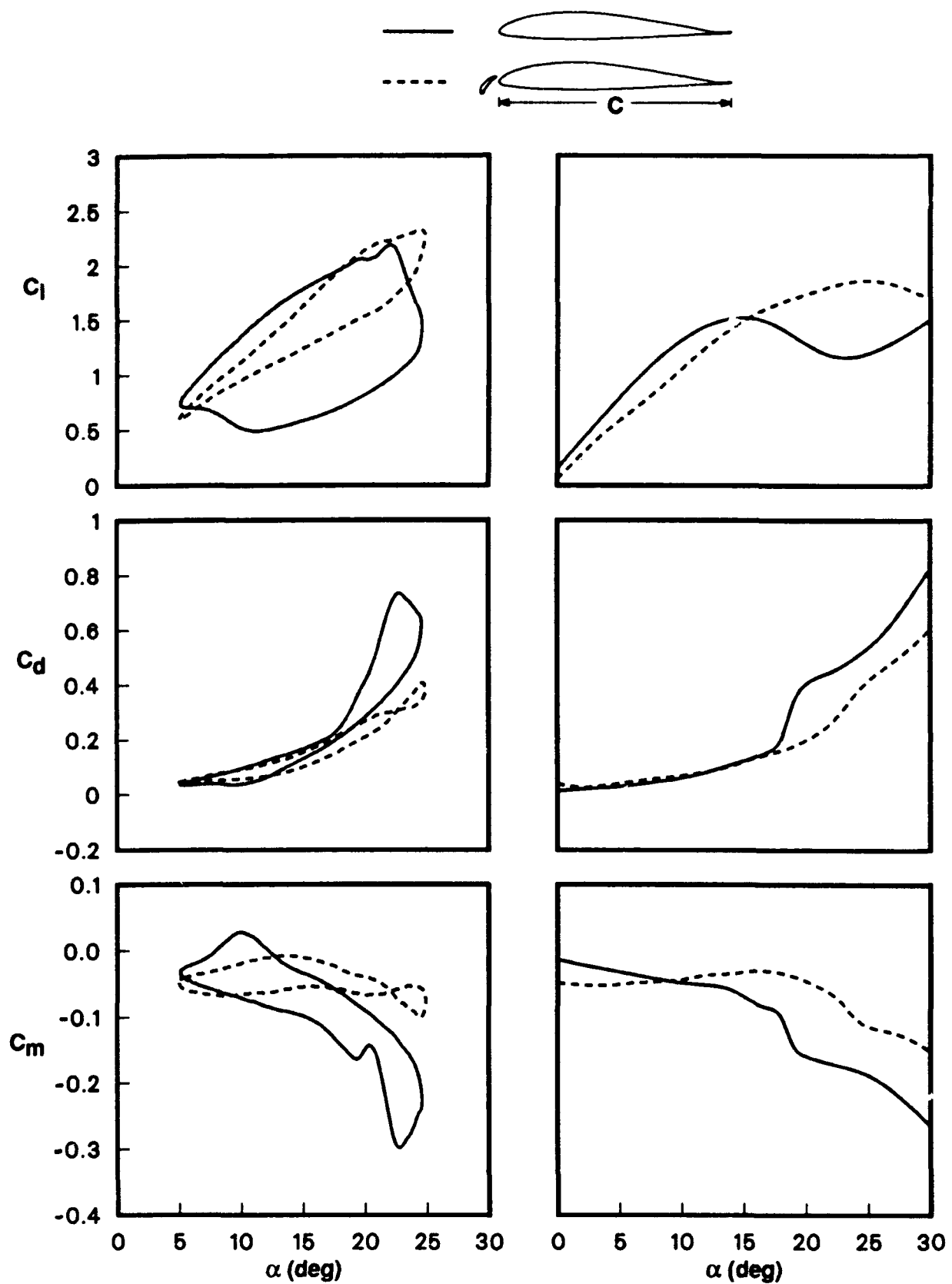


(a) Basic VR-7 airfoil.



(b) VR-7 airfoil with slat.

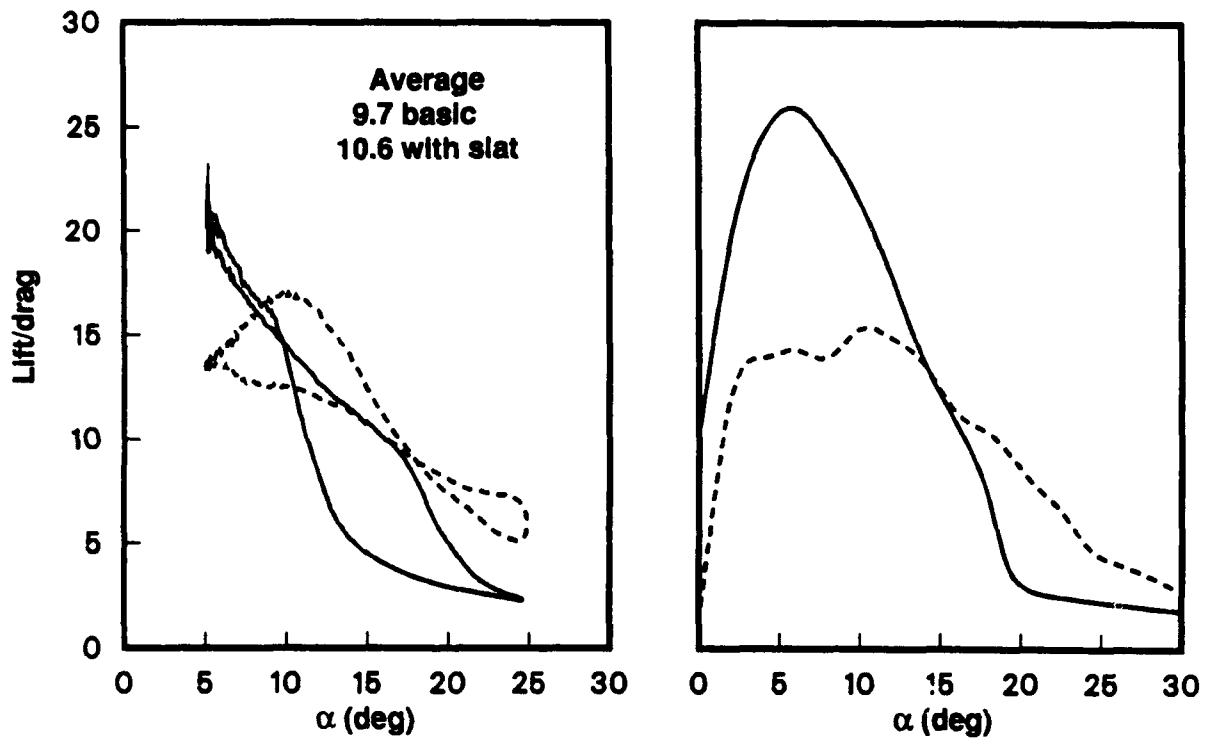
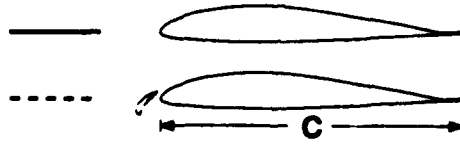
Figure 33. Separation boundaries determined from flow visualizations at  $Re = 200K$  and  $k = 0.1$  with  $\alpha = 15^\circ + 10^\circ \sin(\omega t)$ .



(a) Unsteady:  $\alpha = 15^\circ + 10^\circ \sin(\omega t)$  at  $k = 0.1$ .

(b) Steady:  $\alpha = 0^\circ \rightarrow 30^\circ$ .

Figure 34. Force and moment comparison between basic and slatted VR-7 airfoils at  $Re = 200K$ .



(a) Unsteady:  $\alpha = 15^\circ + 10^\circ \sin(\omega t)$  at  $k = 0.1$ .

(b) Steady:  $\alpha = 0^\circ \rightarrow 30^\circ$ .

Figure 35. Lift/drag comparison between basic and slatted VR-7 airfoils at  $Re = 200K$  for steady and unsteady conditions.

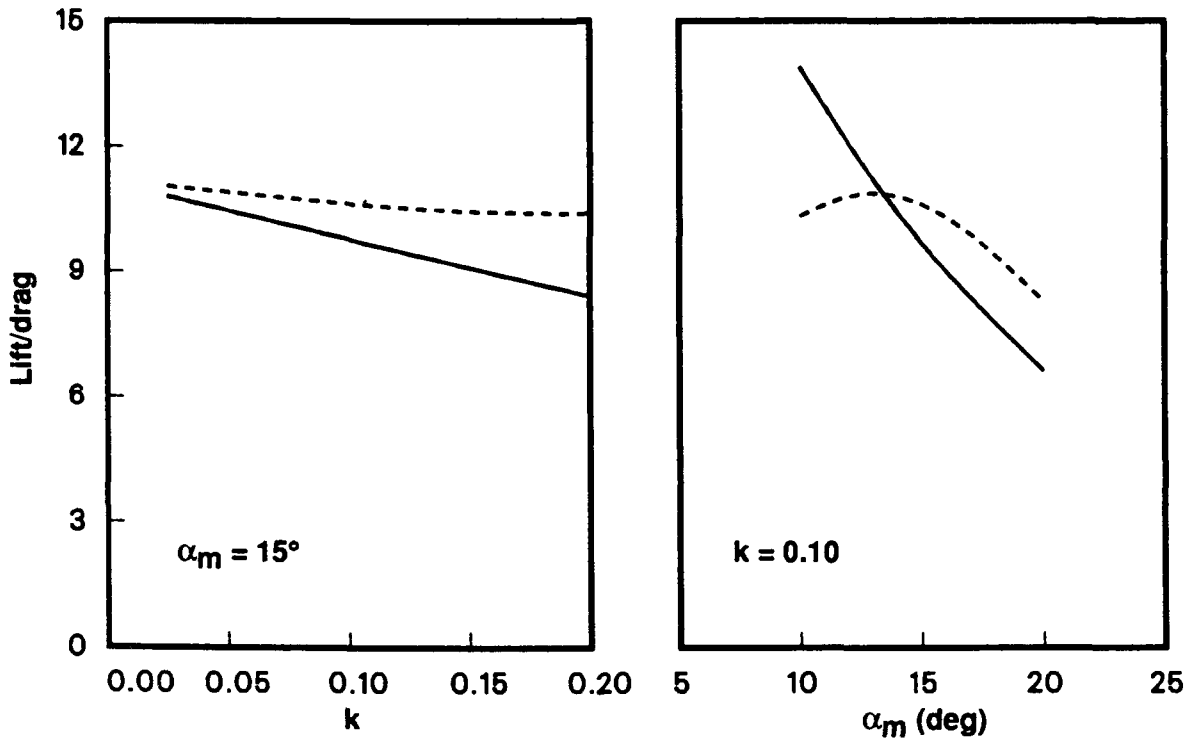
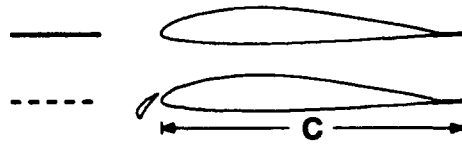
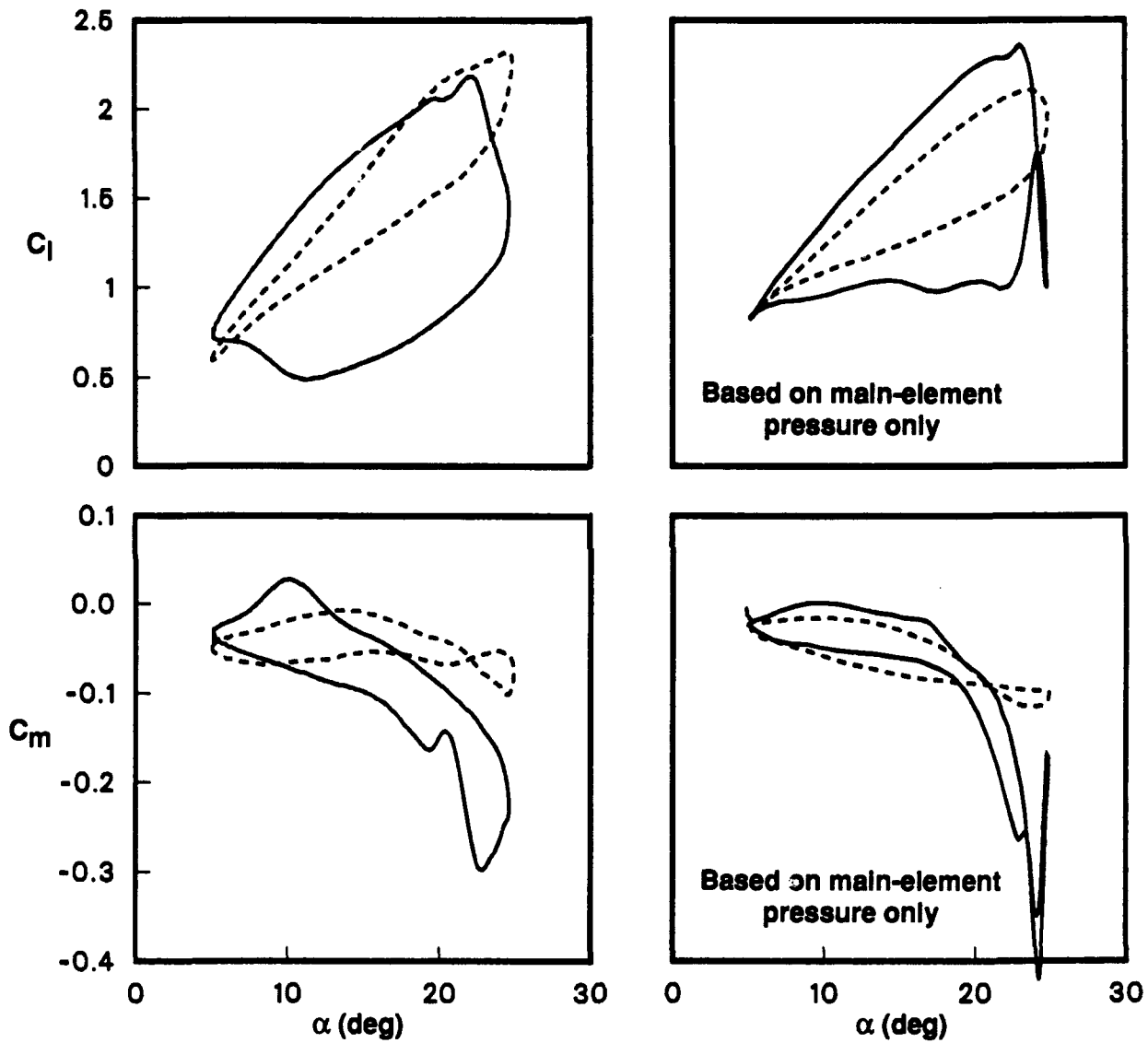
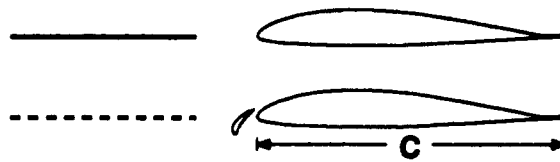


Figure 36. Lift/drag comparison between basic and slatted VR-7 airfoils at  $Re = 200K$  for  $k = 0.025 \rightarrow 0.2$  and  $\alpha_m = 10^\circ \rightarrow 20^\circ$  with  $\alpha = \alpha_m + 10^\circ \sin(\omega t)$ .



(a) Water tunnel,  $Re = 2.0 \times 10^5$ .

(b) Wind tunnel,  $Re = 2.5 \times 10^6$  (ref. 7).

Figure 37. Comparison of water tunnel and wind tunnel results for the basic and slatted VR-7 airfoils at  $k = 0.1$  with  $\alpha = 15^\circ + 10^\circ \sin(\omega t)$ .

# REPORT DOCUMENTATION PAGE

Form Approved  
OMB No. 0704-0188

Public reporting burden for this collection of information is estimated to average 1 hour per response, including the time for reviewing instructions, searching existing data sources, gathering and maintaining the data needed, and completing and reviewing the collection of information. Send comments regarding this burden estimate or any other aspect of this collection of information, including suggestions for reducing this burden, to Washington Headquarters Services, Directorate for Information Operations and Reports, 1215 Jefferson Davis Highway, Suite 1204, Arlington, VA 22202-4302, and to the Office of Management and Budget, Paperwork Reduction Project (0704-0188), Washington, DC 20503.

1. AGENCY USE ONLY (Leave blank)		2. REPORT DATE March 1993	3. REPORT TYPE AND DATES COVERED Technical Paper	
4. TITLE AND SUBTITLE Suppression of Dynamic Stall with a Leading-Edge Slat on a VR-7 Airfoil			5. FUNDING NUMBERS  505-61-51	
6. AUTHOR(S) K. W. McAlister and C. Tung				
7. PERFORMING ORGANIZATION NAME(S) AND ADDRESS(ES) Ames Research Center Moffett Field, CA 94035-1000			8. PERFORMING ORGANIZATION REPORT NUMBER  A-93006	
9. SPONSORING/MONITORING AGENCY NAME(S) AND ADDRESS(ES) National Aeronautics and Space Administration Washington, DC 20546-0001			10. SPONSORING/MONITORING AGENCY REPORT NUMBER NASA TP-3357 ATCOM TR-92-A-013	
11. SUPPLEMENTARY NOTES Point of Contact: K. W. McAlister, Ames Research Center, MS 215-1, Moffett Field, CA 94035-1000 (415) 604-5892				
12a. DISTRIBUTION/AVAILABILITY STATEMENT  Unclassified — Unlimited Subject Category 02			12b. DISTRIBUTION CODE	
13. ABSTRACT (Maximum 200 words) <p>The VR-7 airfoil was experimentally studied with and without a leading-edge slat at fixed angles of attack from <math>0^\circ</math> to <math>30^\circ</math> at <math>Re = 200,000</math> and for unsteady pitching motions described by <math>\alpha = \alpha_m + 10^\circ \sin(\omega t)</math>. The models were two dimensional, and the test was performed in a water tunnel at Ames Research Center. The unsteady conditions ranged over <math>Re = 100,000 \rightarrow 250,000</math>, <math>k = 0.001 \rightarrow 0.2</math>, and <math>\alpha_m = 10^\circ \rightarrow 20^\circ</math>. Unsteady lift, drag, and pitching-moment measurements were obtained along with fluorescent-dye flow visualizations. The addition of the slat was found to delay the static-drag and static-moment stall by about <math>5^\circ</math> and to eliminate completely the development of a dynamic-stall vortex during unsteady motions that reached angles as high as <math>25^\circ</math>. In all of the unsteady cases studied, the slat caused a significant reduction in the force and moment hysteresis amplitudes. The reduced frequency was found to have the greatest effect on the results, whereas the Reynolds number had little effect on the behavior of either the basic or the slatted airfoil. The slat caused a slight drag penalty at low angles of attack, but generally increased the lift/drag ratio when averaged over the full cycle of oscillation.</p>				
14. SUBJECT TERMS Dynamic stall, Leading-edge slat, Airfoil stall			15. NUMBER OF PAGES 70	
			18. PRICE CODE A04	
17. SECURITY CLASSIFICATION OF REPORT Unclassified	18. SECURITY CLASSIFICATION OF THIS PAGE Unclassified	19. SECURITY CLASSIFICATION OF ABSTRACT	20. LIMITATION OF ABSTRACT	